

NUCLEAR BATTERIES WITH TRITIUM  
AND PROMETHIUM-147 RADIOACTIVE SOURCES

BY

GALINA NIKOLAYEVNA YAKUBOVA

DISSERTATION

Submitted in partial fulfillment of the requirements  
for the degree of Doctor of Philosophy in Nuclear Engineering  
in the Graduate College of the  
University of Illinois at Urbana-Champaign, 2010

Urbana, Illinois

Doctoral Committee:

Professor James F. Stubbins, Chair  
Professor George H. Miley  
Professor William D. O'Brien  
Assistant Professor Ling-Jian Meng

# NUCLEAR BATTERIES

## WITH TRITIUM AND PROMETHIUM-147 RADIOACTIVE SOURCES

Galina N. Yakubova, Ph.D.  
Department of Nuclear, Plasma and Radiological Engineering  
University of Illinois at Urbana-Champaign, 2010  
J. F. Stubbins, Advisor

Long-lived power supplies for remote and even hostile environmental conditions are needed for space and sea missions. Nuclear batteries can uniquely serve this role. In spite of relatively low power, the nuclear battery with packaging can have an energy density near a thousand watt-hours per kilogram, which is much greater than the best chemical battery. Moreover, radioactive isotopes are available on the market for reasonable prices and low power electronics are becoming increasingly more versatile. Therefore, nuclear batteries are commercially relevant today.

Literature review and theoretical considerations demonstrate that direct charge nuclear batteries have the highest efficiency converting radioactive decay energy to electricity when compared with other types of nuclear batteries. Direct charge nuclear batteries were chosen for this dissertation research. From calculations of the beta particle flux densities from sources of various isotopes, tritium and promethium-147 were chosen as the most suitable for building a direct charge nuclear battery.

The theoretical analysis of factors influencing the overall efficiency of a direct charge battery with vacuum dielectric are outlined below. The estimated maximum efficiencies of tritium and promethium batteries are 12% and 21%, respectively. The main factors which effect the efficiency are the source construction, secondary electron emission and backscattering from collectors.

Experimentally, it was demonstrated that the efficiency of the tritium direct charge battery model with vacuum dielectrics and collectors with secondary electron emission suppression and backscattering coating reaches 5.5%. This tritium direct charge battery model has an activity of 108 curies and demonstrated open circuit voltage of 5300 volts with short circuit current of 148 nanoamperes. The efficiency can be doubled with double-sided ( $4\pi$ ) sources.

A promethium-147 direct charge battery model of cylindrical design and double-sided ( $4\pi$ ) source and collector having polyimide coating was built and tested. This model had an activity of 2.6 curies and demonstrated open circuit voltage at around 60 kV, short circuit current of 6 nanoamperes and efficiency of up to 15%. The experimentally demonstrated battery efficiency approached theoretical calculations.

Also, the well known effect of charge accumulation in dielectrics under mono-energetic electron beam irradiation was utilized for making nuclear batteries. In this battery, charge accumulated in the surface region of a thick layer of dielectric from beta irradiation and was found to effectively conduct current through an uncharged dielectric.

A simple nuclear battery model was fabricated and tested with a tritium source, a dielectric layer much thicker than the range of tritium beta particles, and a metal collector without vacuum space. This model, with 1 curie of tritium, produced 0.4 microwatts of electrical power on an optimal load resistor of 1 tera-ohm with efficiency approximating 1%. A phenomenological model describing the charging process is suggested in this dissertation and compared favorably with experimental data. Based on the described model, this type of battery having 1000 curies tritium would produce more than 1 milliwatt useful power with efficiency near 4% on a giga-ohm load. While the practically achieved efficiency of the

solid-state nuclear battery is less than that built using vacuum dielectric, it is smaller and mechanically more robust.

While studying the mechanism of nuclear battery charge accumulation in a dielectric, the space charge distribution in a dielectric under tritium irradiation was investigated both theoretically with calculations by Monte Carlo simulation code and experimentally with measurements by the Pulse Electroacoustic method. It was determined that charge accumulated under tritium irradiation in polyimide from the source-facing surface to a depth of approximately 5 microns.

Possible applications of direct charge nuclear batteries and nuclear batteries with charged dielectrics are discussed in this dissertation. Experiments demonstrated the success of using beta batteries to power electrostatic screens for higher voltage alpha direct charge cells, and as spark sources for flash lamps. In the future, their use is promising for integrated electrostatic type motors and photomultipliers. Even ionizing radiation in deep space travel might be harvested utilizing this phenomenon.

This dissertation discusses very promising research regarding the feasibility of a tritium nuclear battery with charged solid dielectric.

## ACKNOWLEDGEMENTS

I would like to acknowledge all those who gave me the opportunity to complete this dissertation. First of all, I would like to express my sincere gratitude to the team of TRACE Photonics, Inc. who supported me at all aspects of my research. Secondly, I would like to thank President TRACE Photonics Dr. Ken Bower, who invited me to be a researcher on this project and has given me invaluable support for five years. I feel very lucky to have been directed by such a brilliant supervisor, Dr. Alexander Kavetskiy, whose knowledge, talents, acceptance and encouragement have constantly inspired my confidence and enthusiasm for research work. I would like to thank Dr. Shahid Yousaf for preparing the dielectric samples; without them the research would have been impossible. Thank you also to Doris Chen who wrote the computer codes for data acquisition during the experiments.

I would like to thank my advisor, Professor James Stubbins, for valuable advice and expert help during my study at this great university, especially during preparation for my dissertation and presentation.

I gratefully acknowledge D. Robertson, A. Garnov, D. Meier (University of Missouri, Columbia), B. Liu and K. Chen (University of Pittsburg) who made and qualified the promethium-147 and tritium sources for this work.

I also would like to thank all the faculty and staff in the Department of Nuclear, Plasma and Radiological Engineering for providing me with support and help in various aspects of graduate school.

Finally, I would like to express my appreciation for the project support provided by the Defense Advanced Research Projects Agency and the U.S. Army, Picatinny Arsenal, under contract W15QKN-04C-1123.

The views, opinions, and/or findings contained in this Dissertation are those of the author and should not be interpreted as representing the official views or policies, either expressed or implied, of the Defense Advanced Research Projects Agency or the Department of Defense.

Approved for Public Release, Distribution Unlimited

## TABLE OF CONTENTS

SYMBOL DESIGNATIONS.....	x
CHAPTER 1: INTRODUCTION.....	1
1.1 Methods of converting radioactive decay energy into electricity .....	1
1.2 Ragone Plot comparison of different types of batteries.....	2
1.3 Actuality of nuclear converters research and developments.....	5
References.....	6
CHAPTER 2: TYPES OF RADIOISOTOPE GENERATORS.....	7
(LITERATURE REVIEW)	
2.1 Classification of radioisotope generators.....	7
2.2 Direct conversion nuclear batteries.....	7
2.3 Indirect conversion nuclear batteries.....	15
2.4 Direct charge nuclear batteries.....	18
2.5 Comparison of different types of nuclear batteries.....	24
References.....	25
CHAPTER 3: THEORETICAL ESTIMATION OF THE DIRECT CHARGE.....	29
NUCLEAR BATTERY EFFICIENCY	
3.1 Equation for calculation of the efficiency of the direct charge nuclear battery...	29
3.2 Factors affecting efficiency of direct charge nuclear battery.....	30
3.3 Estimation of the theoretical efficiency of direct charge nuclear battery .....	56
3.4 Directions of research.....	57
References.....	57
CHAPTER 4: TRITIUM DIRECT CHARGE NUCLEAR BATTERY.....	60
4.1 Tritium beta source (manufacturing and characteristics).....	60
4.2 Experimental setup for testing tritium direct charge nuclear battery.....	66
4.3 Design of tritium direct charge nuclear battery.....	69

4.4 Testing results of multilayer tritium direct charge nuclear battery,.....	77
efficiency of tritium direct charge nuclear battery	
References.....	82
CHAPTER 5: PROMETHIUM-147 DIRECT CHARGE NUCLEAR BATTERY.....	83
5.1 Promethium-147 beta source (fabrication and characteristics).....	83
5.2 Experimental setup for testing Pm-147 direct charge nuclear battery.....	89
5.3 Testing results of Pm-147 direct charge nuclear battery,.....	92
efficiency of Pm-147 direct charge nuclear battery	
References.....	102
CHAPTER 6: TRITIUM NUCLEAR BATTERY WITH SOLID DIELECTRIC.....	103
6.1 Operational principle of nuclear battery with solid dielectric.....	103
6.2 Charge accumulation and storage in the dielectric under irradiation.....	108
6.3 Dielectrics.....	113
6.4 Nuclear battery with charged dielectric model and experimental setup.....	119
6.5 Testing the battery model and modeling the charging process.....	120
6.6 Predicted calculations.....	127
6.7 Conclusion.....	129
References.....	130
CHAPTER 7: APPLICATIONS OF DIRECT CHARGE NUCLEAR BATTERIES.....	132
7.1 Load characteristics and possible direct charge nuclear battery applications.....	132
7.2 Autonomous alpha direct charge nuclear battery (alpha-beta cell).....	133
7.3 Experiments with flash lamp.....	138
7.4 Direct charge nuclear battery as a power supplier for electrostatic motor and... photomultiplier	140
References.....	141
CONCLUSION.....	142
FUTURE WORK.....	145



Appendix A. Measurement of the activity Pm-147 source by gamma-spectrometric..... 146  
method  
References.....149

Appendix B. Measurements of space charge distribution in dielectrics..... 150  
References.....158

LIST OF PUBLICATIONS..... 159

CURRICULUM VITAE..... 160

## SYMBOL DESIGNATIONS

$a$	acceleration
$A$	total activity
$A_s$	surface activity
$A_{sp}$	specific activity
$b$	coefficient of backscattering
$C$	capacitance
$C_{cell}$	cell capacitance
$d$	distance
$d_m$	dielectric density
$D$	mass thickness
$D_{sub}$	mass thickness of substrate
$D_{prot}$	mass thickness of protection sheet
$e_p$	electric field pulse
$E_D$	energy density over time
$E_{e-h}$	energy of electron-hole pair generation
$E_g$	bandgap
$F$	gamma flux
$I_{Ch}$	charging current
$I_{ChP}$	charging particles current
$I_{ion}$	ionization current
$I_{load}$	current through the load resistor
$I_{sc}$	short circuit current
$I_\beta$	beta particles current
$I_{0r}$	reverse saturation current
$k$	Boltzmann's constant
$k_g$	geometrical factor
$k_n$	normalizing factor
$L$	length
$m_e$	mass of an electron
$Mw$	molecular weight
$n$	number of atoms of the radioactive isotope in molecule
$N$	the number of counts
$N_A$	Avogadro's number
$P$	power
$P(t)$	power density with time
$P_d$	absorbed dose rate
$P_{el}$	electrical power on load
$P_{el, \max}$	maximal electrical power on load
$P_{RD}$	power of a radioactive decay
$P_0$	specific power of isotope
$q_e$	elementary charge
$Q_C$	charge on capacitor

$Q_{in}$	emitted charge
$Q_R$	charge through the load resistor
$r$	radius in the units of mass thickness
$r_\beta$	beta particle range
$R$	radius
$R_a$	roughness
$R_{cell}$	internal resistor of the battery (cell)
$R_{div}$	divider resistivity
$R_{leak}$	leakage resistance
$R_{load}$	load resistance
$R_{sq}$	resistivity of 1 cm <sup>2</sup>
$s$	coefficient of secondary electrons emission
$t$	time
$t_m$	dielectric thickness
$T$	absolute temperature
$T_c$	counting time
$T_{1/2}$	half-life of isotope
$U$	voltage
$U_{oc}$	open circuit voltage
$U_{sat}$	saturation voltage
$V$	speed
$w$	width
$W(r)$	point beta source function
$W_0$	stopping power
$Z_{eff}$	effective atomic number
$\varepsilon_{avg}$	average energy of radioactive particle
$\varepsilon_{max}$	maximal energy of radioactive particle
$\varepsilon_\beta$	energy of the beta particle
$\varepsilon_{ion\_pair}$	energy of producing of ion pair
$\eta$	fraction of beta particles flux
$\eta_S$	efficiency of source
$\eta_R(U)$	repulsing factor
$\lambda$	decay constant
$\nu$	mass absorption coefficient
$\xi$	efficiency of battery
$\rho$	space charge density
$\rho_v$	volume resistivity
$\Phi(\theta, \beta)$	beta particle flux at the angles $\theta$ and $\beta$
$\Phi$	beta particle flux
$\Omega$	solid angle
$w(\varepsilon_\beta)$	energy spectrum

# CHAPTER 1

## INTRODUCTION

### 1.1 METHODS OF CONVERTING RADIOACTIVE DECAY ENERGY INTO ELECTRICITY

Devices which transform radioactive decay energy into electricity are called radioisotope generators. Research and development of these devices has progressed since 1913<sup>1</sup>. The main feature of radioisotope generators, which stimulated development for approximately one century, is their ability to produce electricity during years or even dozens of years depending on the half life of the radioisotope. The second advantage of radioisotope generators is high energy density, which can be around ten times higher than hydrogen fuel cells,<sup>2</sup> and a thousand times more than a chemical battery.<sup>3,4</sup> Also, radioisotope generators do not depend on environmental condition. They function over a large range of temperature, pressure, and can work in space or under water. Radioisotope generators are autonomous, so do not need remounting, refilling or recharging.

Conversion techniques for producing electricity from radioisotopes can be grouped into two types: thermal (output power depends on the thermal power of the sources of ionizing radiation) and non-thermal (whose output power is not a function of a temperature difference between the source and outside world).

Thermal converters (radioisotope thermoelectric generator - RTG) are effective starting at several hundred milliwatt electrical power. A large amount of radioactive material is necessary for creating a sufficient thermal gradient for an effective RTG. Usually, at least a gram or more of the alpha or beta radioactive isotopes, with emitted particle energy of several hundreds or thousands kiloelectronvolts (usually Pu-238 and Sr-90)<sup>5</sup>, are used in RTGs. The efficiency of energy conversion for RTGs can reach 8-10%.<sup>6</sup> Modern types of RTG, thermophotovoltaic cells, can reach conversion efficiency up to 20%<sup>7</sup> and theoretical calculation suggest that this value can be increased to 30%.<sup>8</sup> Prototypes of the new

generation of RTG, Stirling Radioisotope Generator, demonstrated an average efficiency of 23%.<sup>8</sup> The large amount of radioactive isotopes in RTGs restrict their applications because of high radiation and radiotoxic dangers. Many modern electronic devices use electrical power in a milliwatt or even microwatt range. Non-thermal converters (so called nuclear batteries – NB) can effectively produce electrical power in this range. NBs can efficiently produce milliwatts of electrical power using not grams but milligrams of radioactive isotopes. Therefore, the NB can find broad application as a power supply for micro and milliwatt electronic devices.

## 1.2 RAGONE PLOT COMPARISON OF DIFFERENT TYPES OF BATTERIES

Comparison of various types of energy supplies can be illustrated with a Ragone Plot. The Ragone Plot graphs the dependence of energy density against power density available on a load.<sup>9</sup> Generally, the vertical axis shows how much energy is available from the supply while the horizontal axis shows how quickly we can take this energy. The sloping lines gives the time to get the charge in or out. All different types of energy storage devices are located in the characteristic regions on this plot. The theory of Ragone Plots, for general classes of energy storage devices with calculation of specific curves, is described by Christen.<sup>10</sup>

A comparison of NB with different isotopes and fuel cell with chemical batteries on a Ragone Plot was done by G.H.Miley et al.<sup>11</sup> The characteristics of NB in this work assumed a specific activity of 12.5 Ci/g for each isotope. Real NBs can use isotopes from different chemical compounds. Common chemical compounds used as carriers of tritium, Pm-147, Ni-63, Sr-90, or Pu-238 are shown in Table 1.1. These isotopes are preferred in NB and RTG.<sup>5</sup> The specific activity  $A_{sp}$  of the listed isotopes, in compounds at 100% content of the particular isotope, were calculated by Equation (1.1) and represented in Table 1.1.

$$A_{sp} = \frac{n \cdot N_A \cdot \lambda}{Mw \cdot 10^{12}}, \text{ GBq/mg} \quad (A_{sp} = \frac{n \cdot N_A \cdot \lambda}{Mw \cdot 3.7 \cdot 10^{13}}, \text{ Ci/mg}) \quad (1.1)$$

where  $n$  is number of atoms of the radioactive isotope in the molecule,  $\lambda$  is decay the constant,  $s^{-1}$ ,  $N_A=6.022 \cdot 10^{23} \text{ mol}^{-1}$  is Avogadro's number,  $Mw$  is the molecular weight,  $\text{g} \cdot \text{mol}^{-1}$ .

The power density with time  $P(t)$  (W/kg) and energy density over time  $E_D$  (W·hr/kg) for specific activity isotopes represented in Table 1.1 were calculated from Equations (1.2) and (1.3):

$$P(t) = 0.001 \cdot P_0 \cdot A_{sp} \cdot \xi \cdot e^{\frac{\ln 2 \cdot t}{T_{1/2}}} \quad (1.2)$$

$$E_D = 24 \cdot 365 \cdot 0.001 \cdot P_0 \cdot \xi \cdot A_{sp} \cdot \int_0^{T_{1/2}} e^{\frac{\ln 2 \cdot t}{T_{1/2}}} dt = 6.32 \cdot P_0 \cdot \xi \cdot A_{sp} \cdot T_{1/2} \quad (1.3)$$

where  $P_0$  is the specific power of isotope ( $\mu\text{W/Ci}$ ),  $\xi$  is the efficiency of conversion of radioactive decay energy to electricity (arbitrary unit) and  $T_{1/2}$  is the isotope half-life (years).

**Table 1.1. Half-life, chemical compound–carrier, specific activity of the chemical compound for tritium, Pm-147, Ni-63, Sr-90, Pu-238, and power density and energy density nuclear batteries used these isotopes**

Parameter	Isotope				
	Tritium	Pm-147	Ni-63	Sr-90	Pu-238
Half-life of isotope, $T_{1/2}$ , yr <sup>13</sup>	12.32	2.62	100.1	28.9	87.7
Chemical compound of isotope	Ti <sup>3</sup> H <sub>2</sub> Sc <sup>3</sup> H <sub>2</sub>	<sup>147</sup> Pm <sub>2</sub> O <sub>3</sub>	<sup>63</sup> Ni	<sup>90</sup> Sr(NO <sub>3</sub> ) <sub>2</sub>	<sup>238</sup> PuO <sub>2</sub>
Specific activity of the chemical compound, $A_{sp}$ , Ci/g	1100	800	57	116	15
Specific power of isotope, $P_0$ , $\mu\text{W/Ci}$ <sup>5</sup>	34	367	103	6700	32000
Power density of battery, $P(0)$ , W/kg	3.4	30	0.6	78	50
Energy density of battery, $E_D$ , W·hr/kg	$2.9 \cdot 10^5$	$4.9 \cdot 10^5$	$3.7 \cdot 10^5$	$1.4 \cdot 10^7$	$2.8 \cdot 10^7$

The efficiency of conversion of radioactive decay energy to electricity  $\xi$  was assumed to be 0.1.<sup>11</sup> The energy density for each isotope was calculated over the period of one half life of the particular isotope. Because the mass penalty does not apply to chemical and fuel batteries<sup>12</sup>, it was not taken into account for NB and RTG in calculation of Ragone Plots.

The specific Ragone curves for NB and RTG are shown in Figure 1.1. These curves represent the regions of specific power and specific energy in which the NB and RTG can operate.

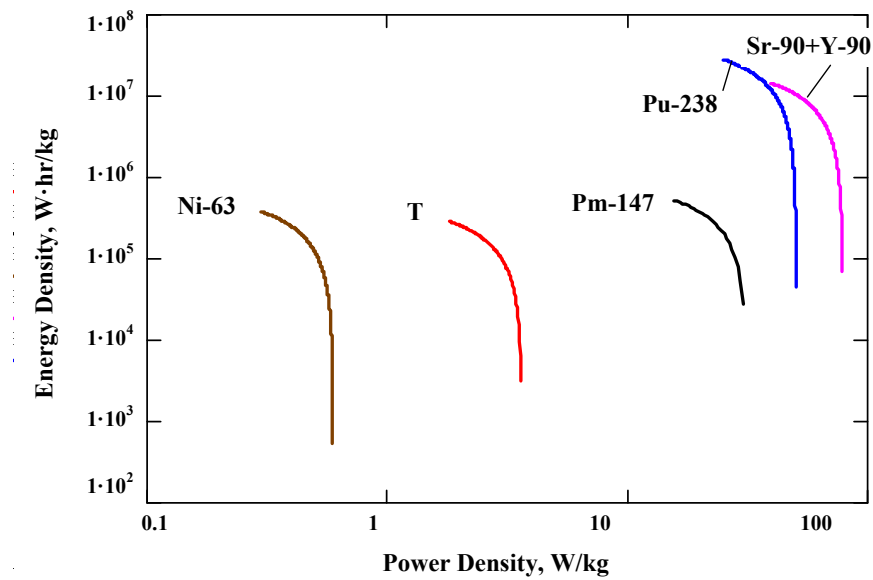


Figure 1.1. Ragone curves for NB (tritium, Pm-147, Ni-63, Sr-90+Y-90) and RTG (Pu-238)

The Ragone plot for nuclear batteries and various electrochemical devices<sup>14</sup> is shown in Figure 1.2. Examining the plot we see that nuclear batteries of Pm-147 and Sr-90 are approximately the same power densities as chemical batteries and fuel cells; nuclear batteries using tritium and Ni-63 have power densities an order or two lower but energy density 3-5 orders higher compared with chemical batteries and fuel cells. Therefore, they can supply electricity much longer than chemical power supplies.

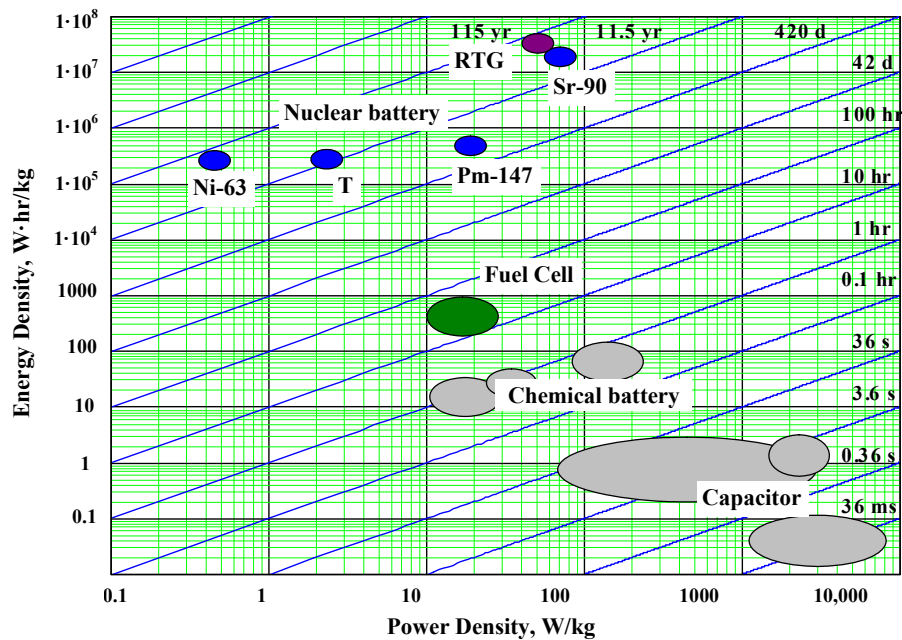


Figure 1.2. Ragone Plot for nuclear batteries and various electrochemical devices

Thus, investigation in the field of nuclear batteries allows development of autonomous, long-lived batteries for low energy electronic devices in hard-to-reach and extreme environmental conditions.

### 1.3 ACTUALITY OF NUCLEAR CONVERTERS RESEARCH AND DEVELOPMENTS

Electronic devices used in space, sea, and other remote environments require minimum maintenance, are long-lived (at least several years), and only require power in the milliwatt or even microwatt range. Microelectromechanical systems (MEMS) require very small power sources to be integrated in one package. Small scale chemical batteries cannot provide enough power for such devices. As the size of the chemical battery is reduced, the amount of stored energy goes down exponentially.<sup>15</sup> Radioisotope fuels can be fabricated as ultra thin film allowing integration into MEMS with little additional volume. The nuclear batteries could be suitable for numerous applications such as ground sensors, light sensors, crystal oscillators, and transceivers.<sup>16</sup>



The additional stimulus for investigation in the field of nuclear batteries is that radioactive isotopes are available on the market for reasonable prices in multicurie quantities today.

The investigation in the field of nuclear batteries is practical and feasible and was therefore chosen as the present dissertation research.

## REFERENCES

- <sup>1</sup> H. G. J. Moseley, and J. Harling, "The Attainment of High Potentials by the Use of Radium," *Proc. R. Soc. (London) A*, **88**, 471 (1913).
- <sup>2</sup> <http://www.fuelcellsforpower.com/Energy-Density.html>
- <sup>3</sup> <http://www.batteryuniversity.com/partone-3.htm>
- <sup>4</sup> <http://homepages.cae.wisc.edu/~blanchar/res/BlanchardKorea.pdf>
- <sup>5</sup> W. R. Corliss, and D. J. Harvey, "Radioisotopic power generation," *Englewood Cliffs: Prentice-Hall* (1964).
- <sup>6</sup> Y. V. Lazarenko, V. V. Gusev, and A. A. Pystovalov, "Basic parameters of a radionuclide thermoelectric generator," *Atomic Energy* **64** (2), 131 (1988).
- <sup>7</sup> D. J. Anderson, W. A. Wong, et al., "An Overview and Status of NASA's Radioisotope Power Conversion Technology NRA," *NASA/TM-2005-213980* (2005).
- <sup>8</sup> [http://en.wikipedia.org/wiki/Radioisotope\\_thermoelectric\\_generator](http://en.wikipedia.org/wiki/Radioisotope_thermoelectric_generator)
- <sup>9</sup> [http://en.wikipedia.org/wiki/Ragone\\_chart](http://en.wikipedia.org/wiki/Ragone_chart)
- <sup>10</sup> T. Christen, and M. W. Carlen, "Theory of Ragone plots," *Journal of Power Sources* **91**, 210 (2000).
- <sup>11</sup> M. Romer, G. H. Miley, and R. J. Gimlin, "Ragone Plot Comparison of Radioisotope Cells and the Direct Sodium Borohydride/Hydrogen Peroxide Fuel Cell With Chemical Batteries," *IEEE Transactions on Energy Conversion* **23** (1), 171 (2008).
- <sup>12</sup> D. Linder, and T. B. Reddy, "Handbook of Batteries," *3<sup>rd</sup> ed.*, *McGraw-Hill* (2002).
- <sup>13</sup> <http://www.nndc.bnl.gov/chart/>
- <sup>14</sup> <http://www.mpoweruk.com/performance.htm>
- <sup>15</sup> A. Lal, and J. Blanchard, *IEEE Spectrum*, 36 (2004).
- <sup>16</sup> K. E. Bower, Y. A. Barbanel et al., "Radioisotope Microbattery Commercialization." In: K. Bower, Y. A. Barbanel, Y. Shreter, G. Bohnert, (Eds.), *Polymers, Phosphors, and Voltaics for Radioisotope Microbatteries*. CRC Press, 39 (2002).

## CHAPTER 2

### TYPES OF RADIOISOTOPE GENERATORS (LITERATURE REVIEW)

#### 2.1 CLASSIFICATION OF RADIOISOTOPE GENERATORS

The classification of nuclear devices by their principle of conversion of radioactive decay energy into electricity is shown in Figure 2.1.<sup>1</sup> Radioisotopes generators are either thermal converters, such as RTGs, or non-thermal converters, such as nuclear batteries. The nuclear batteries in turn, can be divided into three groups based on conversion principles – direct conversion, indirect conversion and direct charge nuclear batteries. To the original scheme<sup>1</sup> we introduced a new type of nuclear battery – nuclear battery with a charged solid dielectric based on charge accumulation in the dielectric. The investigation of this type of battery will be described later.

#### 2.2 DIRECT CONVERSION NUCLEAR BATTERIES

Direct Conversion Nuclear Batteries can be based on the betavoltaic effect, contact potential difference, and secondary emission from an irradiated surface.

##### 2.2.1 Direct Conversion Nuclear Batteries with betavoltaics

The betavoltaics effect is the creation of excess electron-hole pairs by impinging beta particles. The first report of the betavoltaic effect was by Ehrenberg in 1951.<sup>2</sup> Rappoport in 1953 described a betavoltaic cell using Sr-90 and Y-90 coupled with a semiconductor junction.<sup>3</sup> In 1960, the Radiation Research Corporation built betavoltaic batteries with Pm-147 on silicon with overall efficiencies of 0.4% and 0.77%.<sup>4</sup> Table 2.1 compares characteristics of betavoltaics batteries that were fabricated and tested in previous years.

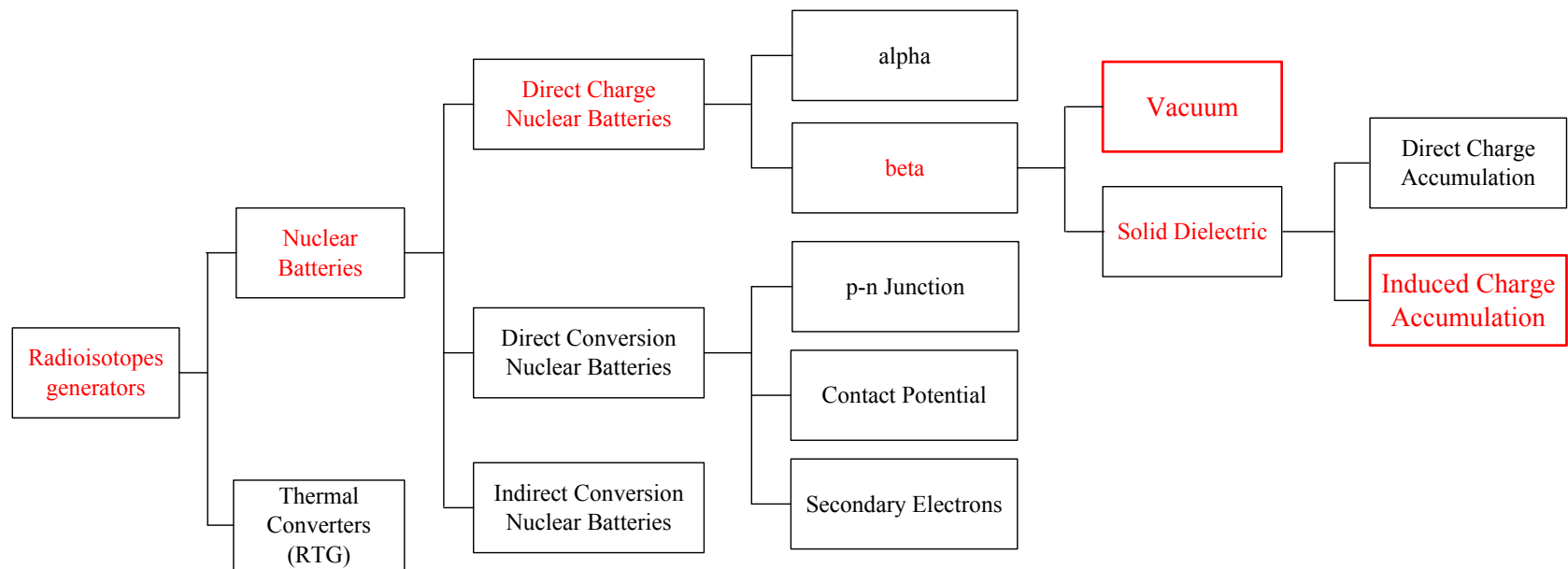


Figure 2.1. Types of nuclear radioisotope generators.<sup>1</sup>

**Table 2.1. Design and characteristics of betovoltaiics batteries.**

Battery design			Battery parameters				Ref.
Isotope	Activity, Ci	Beta-voltaic	$I_{sc}$ , nA	$U_{oc}$ , V	$P$ , $\mu$ W	Efficiency %	
Sr-90+ Y-90	0.05	Si, Ge	4300	0.2	0.8	0.2	6
Pm-147	6.3	Si	-	-	<9	0.4	7
Pm-147	6.8	Si	62000	0.26	9.1	0.77	
Pm-147	66	Si	112000	4.9	400	1.7	4
Tritium	0.048 per cm <sup>2</sup>	a-Si:H	0.98	0.021	0.29 per cm <sup>2</sup>	-	8
Ni-63	0.001	Si	2.86	0.128	0.032	-	9
Tritium	gas	3D porous Si	18000 per Ci	0.016	-	0.22	10
Ni-63	0.2 per cm <sup>2**</sup>	GaN	1100	2.30	-	25.4*	11
Ni-63	0.2 per cm <sup>2**</sup>	Al <sub>0.7</sub> Ga <sub>0.3</sub> N	600	4.90	-	27.4*	
P-33	0.23	SiC	565	2.04	0.58	0.56	12
Ni-63	0.001	4H SiC	0.042	0.72	-	6*	13
Kr-85	1.2	SiC	-	1.8	-	0.75- 1.15	14
Tritium	0.1 per cm <sup>2</sup>	Al <sub>0.35</sub> Ga <sub>0.65</sub> As	40 per cm <sup>2</sup>	0.75	0.024 per cm <sup>2</sup>	0.6	15
Tritium	gas	Al <sub>0.35</sub> Ga <sub>0.65</sub> As	760 per cm <sup>2</sup>	0.91	0.55 per cm <sup>2</sup>	1.2	
Pm-147	0.03	SiC	-	-	0.0003	0.6	16
Ni-63	0.01	Si	54	0.082	-	-	17
Tritium	Gas Pressure 678 torr	a-Si:H	610 per cm <sup>2</sup>	0.43	0.129	1.2	18

\* Betavoltaic efficiency only

\*\* Calculated value for 4 $\mu$ m Ni-63 thickness

As seen in Table 2.1, Direct Conversion Nuclear Batteries with betavoltaics have an open circuit voltage not exceeding several volts, as determined by the semiconductor pairs used in the design.

The operating principle of the p-n junction type is shown in Figure 2.2.<sup>1</sup> The kinetic energy of beta particles creates the electron-hole pairs. Due to the potential difference on the p-n junction they are separated and induce current on the load resistor. The open circuit voltage is

$$U_{oc} = \frac{kT}{q_e} \cdot \ln\left(\frac{I_{sc}}{I_{0r}} + 1\right),^3 \quad (2.1)$$

where  $I_{0r}$  is the reverse saturation current,  $T$  is the absolute temperature,  $k$  is Boltzmann's constant, and  $q_e$  is an elementary charge.  $I_{sc}$  is the short circuit current produced by irradiation equal to the beta particle current times a multiplication factor. This factor is the ratio of the average energy of the beta particles reaching the junction to the energy of electron-hole pair generation in the semiconductor. The energy of electron-hole pair generation can be estimated as

$$E_{e-h} = 2.67 \cdot E_g + 0.87, \quad (2.2)$$

where  $E_g$  is the bandgap of the semiconductor. The multiplication factor for radioisotope Sr-90, for example, is 200,000 electrons per beta particle.<sup>5</sup> Estimation using these equations give the open circuit voltage from several hundred millivolts to volts depending on the strength of irradiation and the semiconductor bandgap.<sup>10</sup>

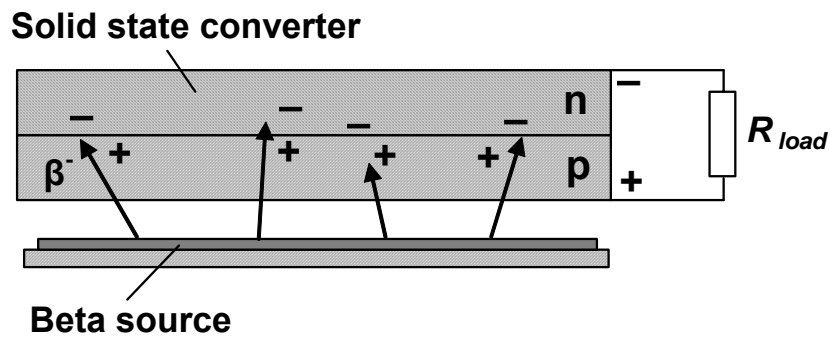


Figure 2.2. Operating principle of the p-n junction type cell<sup>1</sup>

Another feature of Direct Conversion Batteries with betavoltaics is that overall efficiency is not more than 2%, as shown in Table 2.1. The overall efficiency depends on both the source efficiency in providing flux into the betavoltaic, and the efficiency of conversion of beta flux absorbed by betavoltaics into electricity (betavoltaic efficiency). The theoretical calculated betavoltaic efficiency vs. semiconductor bandgap is shown in Figure 2.3. The betavoltaic efficiency increased with bandgap and can reach 30% for such wide bandgap betavoltaics like GaN and AlN. The source efficiency depends on the isotope particle energies and thickness (mass thickness) of the radioactive layer. For example, Pm-147 widely used in Direct Conversion Battery with betavoltaics and with a mass thickness of  $5 \text{ mg/cm}^2$ , has a source efficiency of 25%.<sup>19</sup> Although, theoretically, the overall efficiency (betavoltaic efficiency  $\times$  source efficiency) can approach 7-10% and the practical demonstrated battery efficiency is not more than 2%.

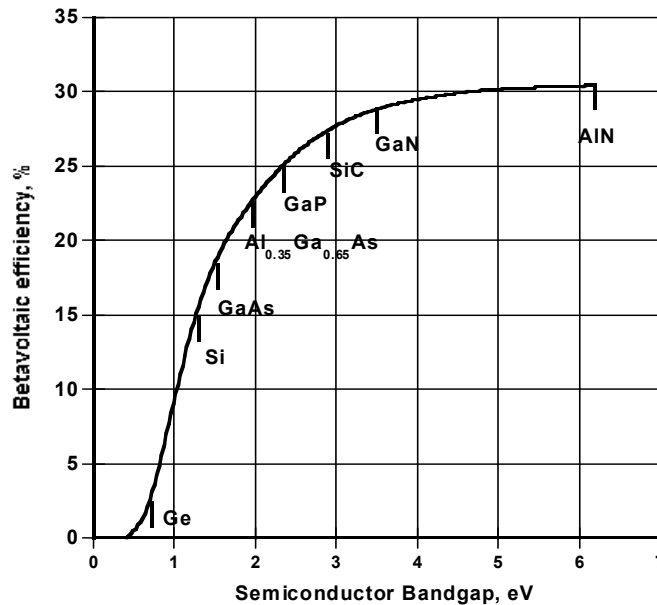
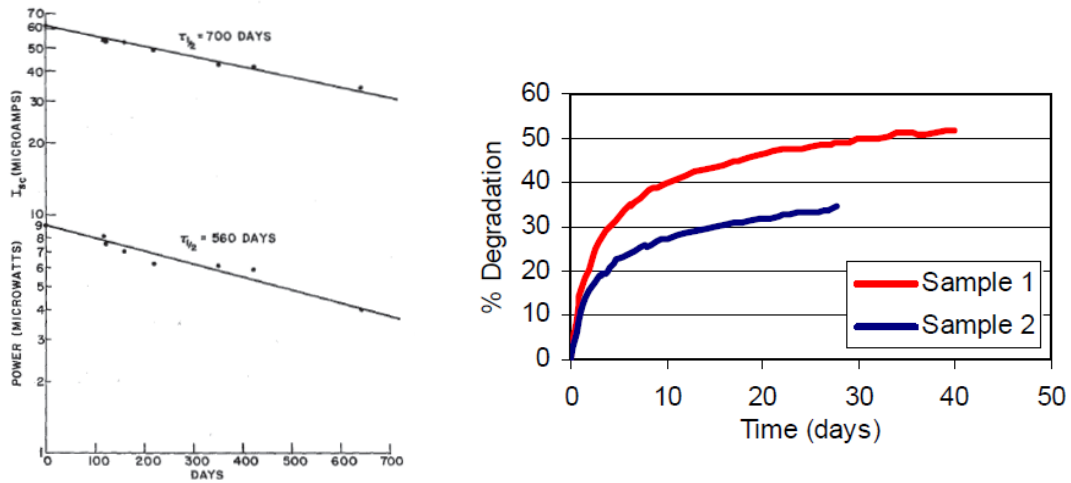


Figure 2.3. Dependence of the betavoltaic efficiency vs. semiconductor bandgap<sup>4</sup>

Demonstrated efficiency in Table 2.1 is given at the beginning of the battery life. Prolonged beta-irradiation produces defects as a result of radiation damage and fracture of the semiconductor crystal by high energy beta particles. This lowers efficiency over time in

the semiconductor. The power and efficiency decrease with time, due to both radioactive decay and radiation degradation of semiconductor. For example, in Figure 2.4a<sup>6</sup> the short circuit current and battery power are from a 6.8 Ci Pm-147 source and silicon betavoltaic with time as shown below. Short circuit current and power decrease with a half-life of 560 days (1.5 yr), which is shorter than the Pm-147 radioactive decay half-life of 960 days (2.62 yr). Figure 2.4b<sup>13</sup> shows the 30-50% degradation during 30-40 days for the betavoltaic battery with 1.2 Ci of Kr-85 and SiC betavoltaic. This was much faster than the rate of radioactive decay Kr-85 alone.



A

b

Figure 2.4. Examples of betavoltaic batteries degradation with time. a) Pm-147+Si<sup>6</sup>, b) Kr-85+SiC<sup>13</sup>

The rate of radiation degradation of betavoltaic is caused by two main factors - intensity of irradiation and bond strength of the semiconductor material. Wide bandgap materials like III-Nitrides demonstrate radiation stability when exposed to very high absorbed doses and energy of irradiated particles.<sup>20</sup> Betavoltaics such as GaN and AlGaN in Direct Conversion Batteries with betavoltaics can improve stability of these devices and investigations are ongoing.<sup>10</sup>

In summary, Direct Conversion Nuclear Batteries with betavoltaics have the following features:

- the open circuit voltage can reach several volts,
- overall efficiency has been demonstrated to be approximately 2%, while theoretical values are approximately 7-10%,
- loss in output power is determined by both the radioactive decay of the isotope and the radiation degradation of the betavoltaic.

### 2.2.2. Contact Potential Difference Batteries

The first demonstrated Contact Potential-Difference type battery (CPD) was by Kramer in 1924<sup>21</sup> and is shown in Figure 2.5. The particle from the radioactive gas (or solid) collides with molecules of gas (solid) to create negative and positive ions, which move to opposite electrodes. The theoretical voltage on the cell is determined by the difference in work functions of the two electrode metals.

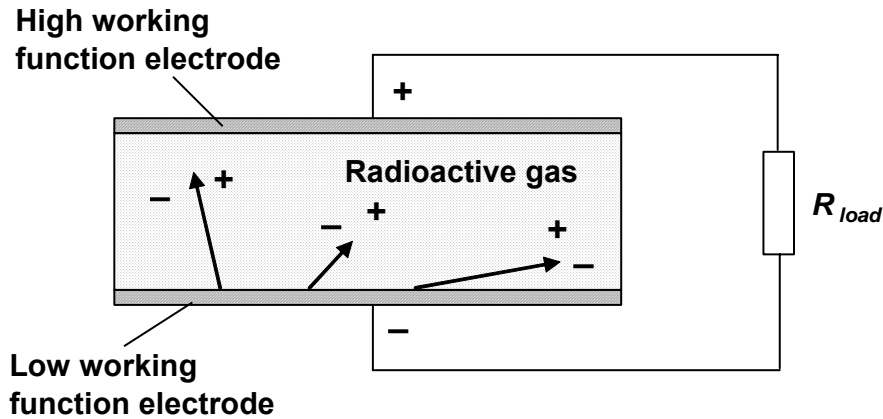


Figure 2.5. Operating principle of Contact-Potential Difference (CPD) type cell<sup>21</sup>

The CPD cell on a scandium tritide source was described by Liu, et al. in 2008.<sup>22</sup> In this case, the electrical field was created by the work function difference between ScT<sub>2</sub> film



and platinum or copper collectors. The charge created in the dielectric between collectors generates current through the load resistance. Open circuit voltage of 0.5 V and short circuit current density of 2.67 nA/cm<sup>2</sup> was demonstrated. The energy conversion of such type of battery is low (0.5%)<sup>23</sup> due to high average energy of ion pair formation in gas (about 30 eV).<sup>24</sup>

### 2.2.3. Secondary Electron Emission Batteries

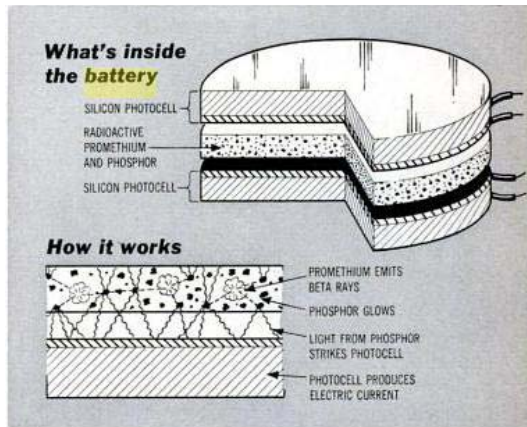
The theory behind the Secondary Emission Battery is based on the collection of secondary electrons caused by collision of high energy primary beta particles (or photons) with a thin layer of dielectric material placed between electrodes. The number of secondary electrons is much greater than primaries; yet, their energy is less. Therefore, the output current of this battery is larger compared to the current of the primary particles. Also, the output voltage of the battery is less than the direct collection of primary particles. This type of battery was first proposed by Schwartz in 1955,<sup>25</sup> and theoretical investigation in this field has continued, for example, in Young et al.,<sup>26</sup> and V.M. Balebanov et al.<sup>27</sup> Practical devices have not been built, possibly due to efficiency not greater than 1%.<sup>28</sup>

### 2.2.4. The Gamma-Electric Cell

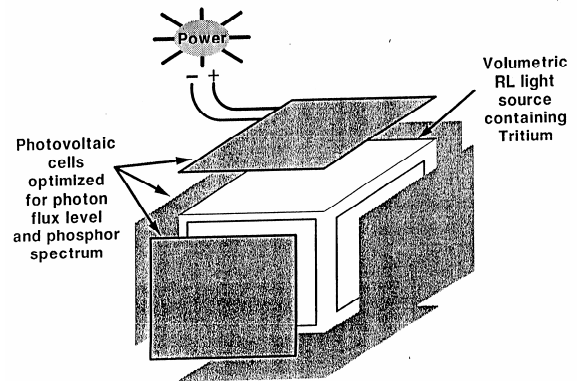
The Gamma-Electric Cell (GEC) is based on the concept of collecting electrons that are Compton scattered from photon radiation. The GEC can be built using vacuum or solid dielectric between electrodes. In the first case, the collector accumulates electrons created at an emitter. In the second case, the collector accumulates the electrons created in the dielectric.<sup>29,30</sup> An example of this kind of battery with solid dielectric using 1000 Ci Co-60 (1.25 MeV average photon energy) was built and had 50 mW output power at 500,000 V with overall efficiency 0.35%. A GEC using isotopes with less gamma energy will have an even lower efficiency.<sup>31</sup> Because of the high energy and large amount of gamma isotope, this kind of battery needs a large and heavy shield and is not suitable for the present research applications. Because of these drawbacks, we will not consider this kind of battery in future investigations.

## 2.3. INDIRECT CONVERSION NUCLEAR BATTERIES

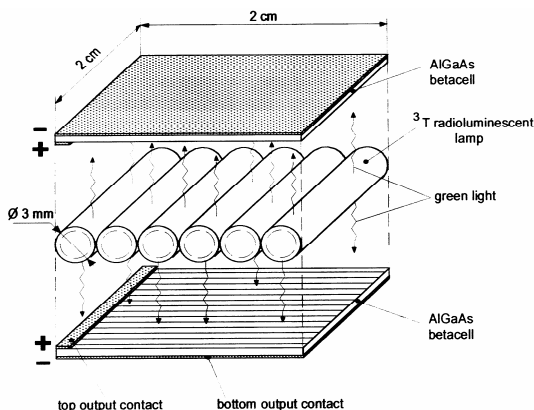
Another possible way to generate electricity from radioactive decay is a double step conversion. In this method, the radioactive decay energy (alpha- or beta-particles) is first converted to ultra-violet or visible light radiation in radioluminescent material (phosphor). Then, the light is converted to electrical energy by a photovoltaic. The designs of some Indirect Conversion Nuclear Batteries are shown in Figures 2.6 a,<sup>32</sup> b,<sup>33</sup> c,<sup>34</sup> d.<sup>35</sup> As can be seen in Figure 2.6, for transformation of radioactive decay energy to light one can use a mixture of Pm-147 with CdS-based phosphor,<sup>32</sup> radioluminescent tritium-filled light source of tubular<sup>34</sup> or microspherical shape,<sup>35</sup> aerogel phosphor composition saturated with tritium,<sup>33</sup> or a tritium containing organic luminophor.<sup>36</sup>



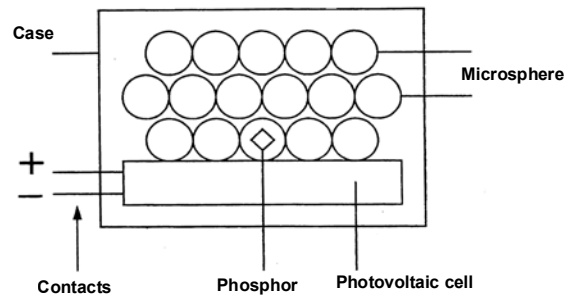
a) Battery with phosphor and Pm-147 mixture<sup>32</sup>



b) Battery with tritium aero gel composition<sup>33</sup>



c) Tritium gas-filled light source based battery<sup>34</sup>



d) Self-luminous microspheres-containing light source-based battery<sup>35</sup>

Figure 2.6. Design of different Indirect Conversion Nuclear Batteries

The intensity of a radioluminescent light source is not high (around  $0.3 \mu\text{W}/\text{cm}^2$  for tritium radioluminescent light source,<sup>37</sup> or around  $20 \mu\text{W}/\text{cm}^2$  for aerogel phosphor saturated with tritium<sup>38</sup>). Special photovoltaics for low intensity light should be used. The spectral distributions of photovoltaic efficiencies suitable for these devices are shown in Figure 2.7. The efficiency of any design of Indirect Conversion Nuclear Battery strongly depends on the match of the emission spectrum of the radioluminescent light and the spectrum of photovoltaic efficiency. The emission spectrums suitable for tubular radioluminescent light sources are shown in Figure 2.8.

Under optimal matching of the luminescent light source and photovoltaic, the overall efficiency can reach 2%.<sup>34</sup> Open circuit voltage of the devices can reach 3.5 V.

Theoretical calculations of devices filled with xenon and a dust of  $10^6$  Ci of radioactive material (Sr-90, Po-210, or Pu-238) and walls covered with AlN photovoltaics, have 25% efficiency. But, this concept has not been practically demonstrated.<sup>41</sup>

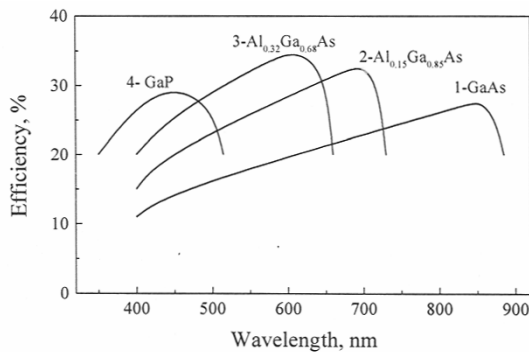


Figure 2.7. The spectral distributions of photovoltaic efficiency for illumination level  $0.1\text{-}10 \mu\text{W}/\text{cm}^2$ <sup>39</sup>

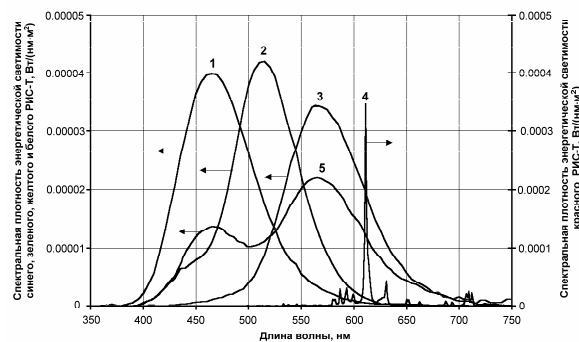


Figure 2.8. The emission spectrum of tubular radioluminescent light sources suitable for indirect conversion nuclear batteries<sup>40</sup>

The efficiencies of these described batteries were referenced at the beginning of device life. Ionizing radiation does not interact with semiconductor material directly in this approach, unlike Direct Conversion Battery. But, the output characteristics do decrease with time faster than radioactive decay alone due to radiation degradation of phosphors. For

example, the change in brightness of different types of gaseous tritium-filled radioluminescence sources with time in comparison with tritium decay is shown in Figure 2.9. The rate of brightness loss is at least two times faster than the tritium decay rate alone. Using alpha isotopes with higher ionizing energies increases the phosphor degradation even faster. A Indirect Conversion Nuclear Battery using a Pu-238 source with activity 300 mCi, a AlGaAs photovoltaic cell, a phosphor screen of (Zn,Cd)S:Ag,Cl (trademark B3g) and a reflective foil for increasing input photovoltaic light signal<sup>42</sup>, was fabricated and tested. It originally showed an open circuit voltage of 2.3 V, short circuit current of 14  $\mu$ A, and an output power of 21  $\mu$ W. This power was enough to supply an 8-digital electronic calculator and wrist watch. But, in only a few days the output dropped several fold. Figure 2.10 shows the radiation degradation mentioned above and other luminophors under alpha irradiation. Alpha radiation stable phosphors were not available in this experiment.

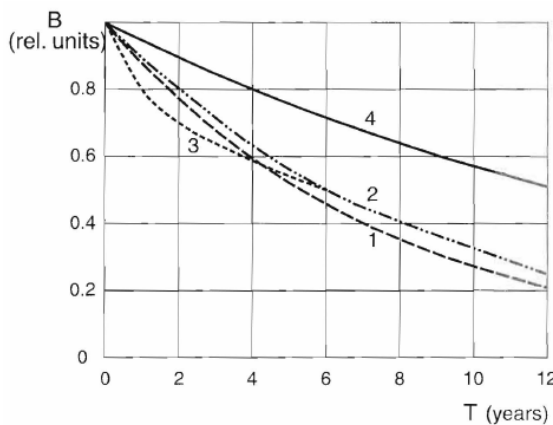


Figure 2.9. Dependencies of relative brightness of different gaseous tritium-filled tubular tritium light sources (curves 1-3) and relative tritium activity in light source (curve 4) with time

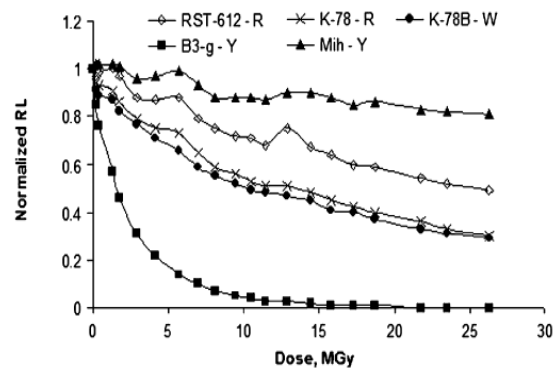


Figure 2.10. Radiation degradation of some luminophors under alpha irradiation ( $P_d=64$  kGy/hr)

In summary, Indirect Conversion Nuclear Batteries have the following features:

- the open circuit voltage of several volts,
- overall efficiency of approximately 2%,
- decreasing output power is determined by both the radioactive decay of the isotope and radiation degradation of the phosphors.

## 2.4. DIRECT CHARGE NUCLEAR BATTERIES

The operating principle of the Direct Charge Nuclear Battery (DCNB) is the direct collection of charged particles emitted from a source electrode on an opposite electrode. DCNB can be built using beta or alpha emitters.

### 2.4.1 Principle of work Direct Charge Nuclear Batteries

In the simplest case, the DCNB is a radioactive source on or in a conductive foil facing a metal foil on which the electrostatic charge is accumulated. The source and metal foil are separated by a dielectric. The scheme of the direct charge cell with load for describing the charging process is shown in Figure 2.11.

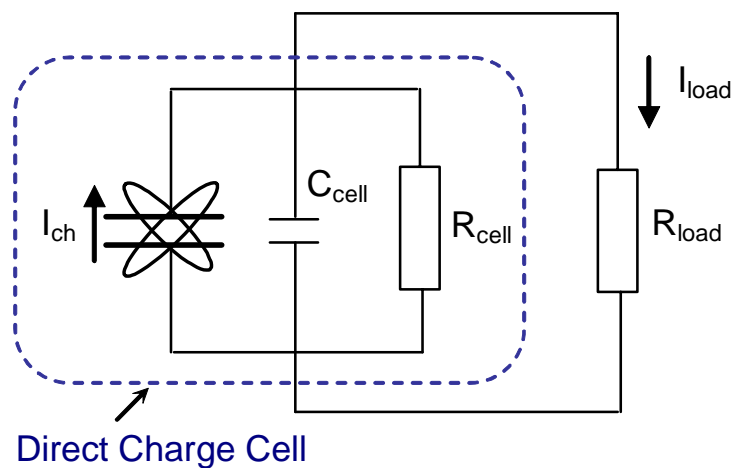


Figure 2.11. Scheme of the direct charge cell with load

Some of the emissions directed toward the collector from the radioactive source will be accumulated. The rest are lost through leakage resistance,  $R_{leak}$ . At each time interval from  $t$  to  $t+dt$ , the charge emitted from the radioactive source toward the collector  $dQ_{in}=I_{Ch} \cdot dt$ .  $I_{Ch}$  is the charging current adding charge to the capacitor plate,  $dQ_C$ , and is also subject to leakage,  $-dQ_R$ . The cell has capacitance  $C$  and the voltage accumulated with time is  $U(t)$ :

$$dQ_{in} = dQ_C + dQ_R \quad (2.3)$$

$$dQ_{in} = I_{Ch} \cdot dt; dQ_C = C \cdot dU(t); dQ_R = \frac{U(t)}{R_{leak}} dt \quad (2.4)$$

$$I_{Ch} \cdot dt = C \cdot dU(t) + \frac{U(t)}{R_{leak}} \cdot dt \quad \text{or} \quad \frac{dU(t)}{dt} + \frac{U(t)}{R_{leak} \cdot C} = \frac{I_{Ch}}{C} \quad (2.5)$$

At the beginning of the charge accumulation cycle, when  $I_{Ch}$  isn't impeded by the increasing collector voltage, a solution of Equation (2.5) is:

$$U(t) = I_{Ch} \cdot R_{leak} \left[ 1 - \exp\left(-\frac{t}{R_{leak} \cdot C}\right) \right] \quad (2.6)$$

When the time  $t \gg R_{leak} \cdot C$ , accumulated voltage approaches saturation  $U_{sat}$

$$U_{sat} = I_{Ch} \cdot R_{leak} \quad (2.7)$$

When  $t \ll R_{leak} \cdot C$ ,  $U(t)$  is directly proportional to  $t$ :

$$U(t) = \frac{I_{Ch} \cdot t}{C} \quad (2.8)$$

The DCNB saturated voltage can be calculated using Equation (2.7). If the DCNB is connected in parallel to an external load with resistance  $R_{load}$ , then the leakage resistance is:

$$R_{leak} = \frac{R_{cell} \cdot R_{load}}{R_{cell} + R_{load}} \quad (2.9)$$

where  $R_{cell}$  is the internal resistance of the DCNB.

If  $R_{load} \gg R_{cell}$  then  $R_{leak} = R_{cell}$  (open circuit), then voltage at saturation can be designated as  $U_{oc}$ .

If  $R_{load} = 0$  (short circuit), short circuit current  $I_{sc}$  will equal  $I_{Ch}$ .

The current,  $I_{load}$ , which will go through external load with resistance,  $R_{load}$ , is:

$$I_{load} = \frac{U_{sat}}{R_{load}} = \frac{I_{Ch}}{R_{load}} \cdot \frac{R_{cell} \cdot R_{load}}{R_{cell} + R_{load}} = \frac{I_{Ch} \cdot R_{cell}}{R_{cell} + R_{load}} \quad (2.10)$$

The electrical power on load  $P_{el}$  is:

$$P_{el} = U_{sat} \cdot I_{load} = I_{Ch} \cdot \frac{R_{cell} \cdot R_{load}}{R_{cell} + R_{load}} \cdot I_{Ch} \cdot \frac{R_{cell}}{R_{cell} + R_{load}} = \left( \frac{I_{Ch} \cdot R_{cell}}{R_{cell} + R_{load}} \right)^2 \cdot R_{load} \quad (2.11)$$

The dependence of  $P_{el}$  on  $R_{load}$  has a maximum when  $R_{load} = R_{cell}$  (maximum power theorem). At  $R_{load} = R_{cell}$  the value of  $\frac{R_{cell} \cdot R_{load}}{(R_{cell} + R_{load})^2} = 0.25$ . So the optimal value of useful power  $P_{el, \max}$  is at  $R_{load} = R_{cell}$  and can be estimated as:

$$P_{el, \max} = 0.25 \cdot I_{Ch}^2 \cdot R_{cell} = 0.25 \cdot U_{oc} \cdot I_{sc} \quad (2.12)$$

The power of radioactive decay,  $P_{RD}$ , available for conversion to electricity is estimated as

$$P_{RD} = A \cdot \varepsilon_{avg} \quad (2.13)$$

where  $A$  is the radioactive material activity in Becquerel and  $\varepsilon_{avg}$  is the average energy of emitted radioactive particles in Joules.

The efficiency of the DCNB,  $\xi$ , when the charging current is not decreasing with voltage on collector as a percent of total thermal energy, is:

$$\xi = \frac{P_{el, \max}}{P_{RD}} \cdot 100\% = \frac{0.25 \cdot U_{oc} \cdot I_{sc}}{A \cdot \varepsilon_{avg}} \cdot 100\% \quad (2.14)$$

With activity in gigabecquerel,  $\varepsilon_{avg}$  in kiloelectron volts,  $I_{sc}$  in nanoamperes and  $U_{oc}$  in kilovolts, Equation (2.14) is:

$$\xi = 156 \cdot \frac{U_{oc}(kV) \cdot I_{sc}(nA)}{A(GBq) \cdot \varepsilon_{avg}(keV)} \quad (\xi = 4.22 \cdot \frac{U_{oc}(kV) \cdot I_{sc}(nA)}{A(Ci) \cdot \varepsilon_{avg}(keV)}) \quad (2.15)$$

#### 2.4.2 Historical demonstrations of Direct Charge Nuclear Batteries

The first DCNB was built by Moseley in 1913 with radium-226.<sup>43</sup> The radium isotope was placed in the center of a sphere (see Figure 2.12). The inner surface of the sphere was covered by silver and served as a high voltage electrode. After evacuating the air from the inner space, an open circuit voltage of 150 kV and short circuit current of 0.01 nA were measured.

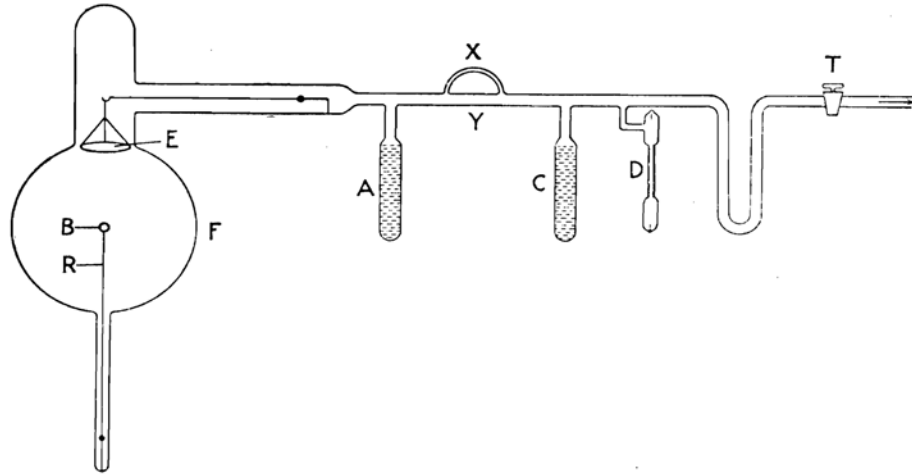


Figure 2.12. B – 20 mCi radium-226; F – glass flask; R – silica rod; A, C – charcoal bulbs; D – discharge tube; T – tap; X, Y – tubes, sealed off after exhaustion; E – electrometer<sup>43</sup>



The theoretical considerations and a practical example of the DCNB using alpha emitter isotopes were developed and constructed at Battelle National Laboratory. This battery delivered 100 kV.<sup>44</sup> DCNB with alpha emitters requires a mesh with negative potential from an external power supply for suppressing the secondary electrons from emitter, so it is not an autonomous device. An autonomous DCNB with alpha emitters was made during the present research. The mesh in this device was powered from a DCNB with a beta emitter, and will be described later.

The first DCNB using Sr-90 with a vacuum dielectric was developed by Linder in 1952.<sup>45</sup> DCNB using Sr-90 with solid polystyrene dielectric was developed by Rappoport in 1953.<sup>46</sup> Radiation Research Corporation designed and produced industrial variants of DCNB using Sr-90<sup>10</sup> and tritium.<sup>47</sup> The Russian Corporation “Majak” built the DCNB using promethium-147.<sup>48</sup>

The efficiency of the nuclear decay energy conversion to electricity calculated by Equation (2.15), and other parameters for DCNB described in the literature, are shown in Table 2.2. As shown from the data represented in this Table, the efficiency of most systems has not been more than 3%. Although, the efficiency of Linder battery<sup>45</sup> is estimated at 10.5%. It is clear that the higher working voltage of collectors in comparison to the energy of charging particles is important to system efficiency. Accumulated voltage is limited by leakage resistance and spontaneous self discharge at higher voltages. Therefore, for making high efficiency DCNB, the isotopes with relatively low average energy such as tritium or Pm-147 are preferable.

**Table 2.2. Parameters of historical direct charge nuclear battery**

Type of Direct Charge Battery	Radioactive source					Electrical parameters of battery				Ref.
	Isotope	Type of particle	$\varepsilon_{avg}$ , keV	$A$		$U_{oc}$ , kV	$I_{sc}$ , nA	$P_{el}$ , $\mu$ W	Eff., %	
				Bq	Ci					
Moseley, 1913	Ra-226	$\alpha$	4870	$7.4 \cdot 10^8$	0.02	150	0.01	0.38	0.06	<sup>3</sup>
Linder, 1952	Sr-Y-90	$\beta$	589	$9.3 \cdot 10^9$	0.25	365	1	91	10.5	<sup>45</sup>
Radiation Research Corporation	Tritium	$\beta$	5.7	$7.4 \cdot 10^9$	0.2	0.4	0.05	0.01	0.07	<sup>49,50,51</sup>
Rappaport, 1953	Sr-Y-90	$\beta$	589	$7.4 \cdot 10^7$	0.002	3.7	0.01	0.01	0.13	<sup>46</sup>
Rappaport, 1953	Sr-Y-90	$\beta$	589	$2.0 \cdot 10^9$	0.054	6.6	0.25	0.41	0.22	<sup>46</sup>
Radiation Research Corporation	Sr-Y-90	$\beta$	589	$3.7 \cdot 10^8$	0.01	7	0.04	0.07	0.20	<sup>52</sup>
Sandia Corporation	Kr-85	$\beta$	251	$3.0 \cdot 10^{10}$	0.8	20	1.2	6.00	0.50	<sup>53</sup>
Gorlovoy, 1950	Sr-Y-90	$\beta$	589	$3.7 \cdot 10^8$	0.01	0.3	0.1	0.01	0.02	<sup>54</sup>
“Majak” BP-1	Pm-147	$\beta$	62	$1.7 \cdot 10^{12}$	46	21	52	273	1.62	<sup>48</sup>
“Majak”, BP-2	Pm-147	$\beta$	62	$2.6 \cdot 10^{12}$	70	23	20	115	0.45	<sup>48</sup>
“Majak”, BP-3	Pm-147	$\beta$	62	$3.7 \cdot 10^{12}$	100	25	90	563	1.53	<sup>48</sup>
“Majak”, BP-4	Pm-147	$\beta$	62	$3.5 \cdot 10^{12}$	94	30	72	540	1.56	<sup>48</sup>
“Majak”, BP-5	Pm-147	$\beta$	62	$4.1 \cdot 10^{12}$	110	23	55	316	0.78	<sup>48</sup>
“Majak”, BP-6	Pm-147	$\beta$	62	$4.3 \cdot 10^{12}$	115	30	51	383	0.91	<sup>48</sup>
“Majak”, BPM-1	Pm-147	$\beta$	62	$3.0 \cdot 10^{11}$	8	21	10	53	1.79	<sup>48</sup>
“Majak”, BPM-2	Pm-147	$\beta$	62	$6.3 \cdot 10^{11}$	17	25	15	94	1.50	<sup>48</sup>
“Majak”, BPM-3	Pm-147	$\beta$	62	$9.3 \cdot 10^{11}$	25	28	18	126	1.37	<sup>48</sup>
“Majak”, BPM-4	Pm-147	$\beta$	62	$7.4 \cdot 10^{11}$	20	19	16	76	1.03	<sup>48</sup>
“Majak”, BPM-5	Pm-147	$\beta$	62	$1.2 \cdot 10^{12}$	31	42	24	252	2.21	<sup>48</sup>
“Majak”, BPM-6	Pm-147	$\beta$	62	$1.3 \cdot 10^{12}$	35	45	27	304	2.36	<sup>48</sup>
“Majak”, BPM-7	Pm-147	$\beta$	62	$2.6 \cdot 10^{12}$	70	30	63	473	1.84	<sup>48</sup>
“Majak”, BPM-8	Pm-147	$\beta$	62	$1.2 \cdot 10^{12}$	31	35	23	201	1.77	<sup>48</sup>
Anno, Battelle	Po-210	$\alpha$	5304	$1.9 \cdot 10^{11}$	5	50	15	188	0.12	<sup>44</sup>
J. Braun, AB Atomenergy	Tritium	$\beta$	5.7	$1.8 \cdot 10^{11}$	4.8	0.69	2.8	0.48	0.29	<sup>55</sup>

## 2.5 COMPARISON OF DIFFERENT TYPES OF NUCLEAR BATTERIES

Comparison of the open circuit voltage, demonstrated efficiency, and rate of power decay for different ways of converting radioactive decay energy into electricity are represented in Table 2.3.

**Table 2.3. Parameters of different type of nuclear batteries**

Battery Type	Open circuit voltage	Achievable efficiency, %	Rate of power decreasing
Direct Conversion, betavoltaic cell	$\leq 5 \text{ V}$	$\leq 1.7$	2-3 times faster than isotope radioactive decay
Direct Conversion, CPD	0.5 V	0.5	no data
Indirect Conversion	$\leq 5 \text{ V}$	$\leq 2$	2-3 times faster than isotope radioactive decay
Direct Charge	dozens kV	$\leq 3$	follow the isotope radioactive decay

As shown from this brief summary and the information in previously paragraphs, the direct and indirect conversion methods give an open circuit voltage of less than 5 V and an efficiency of less than 2%. The rate of power degradation is 2-3 times more than the rate of isotope radioactive decay. Contact Potential-Difference Batteries have lower open circuit voltage and conversion efficiency.

On the other hand, the Direct Charge Nuclear Battery has these features:

- open circuit voltage (multiplied on elementary charge) of DCNB is comparable with the average energy of charging particles, i.e. several, several dozen, or several hundred kilovolts;
- conversion efficiency of DCNB was demonstrated at a few percent. But, theoretical analysis performed by G. Miley, et al., shows that the theoretical efficiency of the Direct Charge Nuclear Battery reaches 15-17%;<sup>56, 57</sup>
- in the design of nuclear batteries with direct charge radiation sensitive materials, like semiconductor voltaics and phosphors, are absent. Therefore, power loss with time is from isotope decay only and the lifetime such type of battery is reliably longer;
- during operation of nuclear batteries with direct charge, temperature, pressure, and humidity sensitive materials are absent. Therefore, these devices can work in a wide range of environmental conditions;
- some applications of nuclear batteries, such as electrostatic motors which require high voltage, can be provided without up-conversion.

These advantages of Direct Charge Nuclear Batteries make these devices attractive candidates. They have autonomous high voltage power supplies, are long lived and suitable for extreme environmental conditions. This type of nuclear battery was chosen for theoretical and experimental investigations in the present dissertation research.

## REFERENCES

- <sup>1</sup> W. R. Corliss, and D. J. Harvey, "Radioisotopic power generation," *Englewood Cliffs: Prentice-Hall* (1964).
- <sup>2</sup> W. Ehrenberg, et al., "The Electron Voltaic Effect," *Processing Royal Society* **64**, 424 (1951).
- <sup>3</sup> P. Rappoport, "The electron-Voltaic Effect in p-n Junction Induced by Beta Particle Bombardment," *Physical Review* **93**, 246 (1953).

- <sup>4</sup> L. C. Olsen, "Review of Betavoltaic Energy Conversion," *Processing of the 12<sup>th</sup> Space Photovoltaic Research and Technology Conference*, 256 (1993).
- <sup>5</sup> A. B. Garrett, "Nuclear Batteries," *Journal of Chemical Education* **33** (9), 446 (1956).
- <sup>6</sup> P. Rappaport and E. G. Linder, "Radioactive Charging Effects With Dielectrics," *J. Appl. Phys.*, **24**, 9 (1953).
- <sup>7</sup> H. Flicker, J. J. Loferski, and T. S. Elleman, "Construction of a Promethium-147 Atomic Battery," *IEEE Transactions on Electron Devices*, 2 (1964).
- <sup>8</sup> T. Kostasiki, N. P. Knerani, P. Stradins, F. Gaspari, et al., "Tritiated amorphous silicon betavoltaic devices," *IEE Proceeding Circuit Devices Systems* **150** (4), 274 (2003).
- <sup>9</sup> H. Guo, and A. Lal, "Nanopower Betavoltaic Microbatteries," *IEEE Transducer*, 36 (2003).
- <sup>10</sup> W. Sun, N. P. Kherani, et al., "A Three-Dimensional Porous Silicon p-n Diode for Betavoltaics and Photovoltaics," *Advanced Materials* **17** (10), 1230 (2005).
- <sup>11</sup> C. Honsberg, et al., "GaN Betavoltaic Energy Converters," *31<sup>th</sup> IEEE Photovoltaics Specialist Conference*, Orlando, Florida, 3-7 January (2005).
- <sup>12</sup> C. J. Eiting, V. Krishnamoorthy, S. Rodgers, and T. George, "Demonstration of a radiation resistant, high efficiency SiC betavoltaic," *Applied Physics Letters* **88**, 064101 (2006).
- <sup>13</sup> M.V.S. Chandrashekhar, et al. "Demonstration of a 4H SiC betavoltaic cell," *Applied Physics Letters* **88**, 033506 (2006).
- <sup>14</sup> C. J. Eiting, V. Krishnamoorthy, E. Romero, and S. Jones, "Betavoltaic Power Cells," *Proceeding of the 42 Power Source Conference*, 601 (2006).
- <sup>15</sup> V. M. Andreev, A. G. Kavetsky, et al., "Tritium-Powered Betacells Based on  $\text{Al}_x\text{Ga}_{1-x}\text{As}$ ," *Conference Record of the Twenty-Eighth IEEE Photovoltaic Specialists Conference*, 1253 (2000).
- <sup>16</sup> G. C. Rybicki, "Silicon Carbide Radioisotope Batteries," *NASA/CP-2001-210747/REV1*, 200 (2001).
- <sup>17</sup> J. Chu, and X. Piao, "Research of radioisotope microbattery based on beta-radio-voltaic effect," *Journal Micro/Nanolithograph MEMS MOEMS* **8** (2), 021180 (2009).
- <sup>18</sup> S. Deus, "Alpha- and Betavoltaic Cells Based on Amorphous Silicon," *16<sup>th</sup> European Photovoltaic Solar Energy Conference*, TRACE Photonics, Inc., 218 (2000).
- <sup>19</sup> W. F. Windle, "Pm-147-Silicon Betavoltaic Battery Feasibility," *Report Sandia Corporation SC-RR-65-671* (1966).
- <sup>20</sup> V. V. Emtsev, et al., "Radiation-induced defects in n-type GaN and InN," *Physica B* **308-310**, 58 (2001).
- <sup>21</sup> J. V. Kramer, *The Electrician*, **93**, 497 (1924).
- <sup>22</sup> B. Liu, K. P. Chen, N. P. Kherany, et al., "Betavoltaics using scandium tritide and contact potential difference," *Applied Physics Letters* **92**, 083511 (2008).
- <sup>23</sup> A. G. Kavetsky, S. N. Nekhoroshkov, S. P. Meleshkov et al., "Radioactive materials, ionizing radiation sources, and radioluminescent light sources for nuclear batteries." In: K.

- Bower, Y. A. Barbanel, Y. Shreter, G. Bohnert, (Eds.), *Polymers, Phosphors, and Voltaics for Radioisotope Microbatteries*. CRC Press, 39 (2002).
- <sup>24</sup> Y. V. Lazarenko, V. V. Gusev, and A. A. Pystovalov, "Basic parameters of a radionuclide thermoelectric generator," *Atomic Energy* **64** (2), 131 (1988).
- <sup>25</sup> E. Schwartz, "Secondary-Emission Nuclear Battery," AD-66176 (1955).
- <sup>26</sup> R. D. Young, J. P. Hageman et al., US Patent # 5,861,701 (1999).
- <sup>27</sup> V.M. Balebanov, S.S. Moiseev, V.I. Karas et al. "Secondary emission radioisotopic current source," *Atomic Energy* **84** (5), 324 (1998)
- <sup>28</sup> M. Romer, G. H. Miley, and N. Luo, "Computer-Based Study of Secondary Emission Cell (SEC) Efficiency Compared to That of a Vacuum-Type Direct Collection Cell," *IEEE Transactions on Energy Conversion* **23** (1), 331 (2008).
- <sup>29</sup> G. H. Miley, "Direct Conversion of Nuclear Radiation Energy," *American Nuclear Society* (1970).
- <sup>30</sup> H. T. Sampson, and G. H. Miley, "Gamma-Electric Cell," *US Patent* 3,591,860 (1968).
- <sup>31</sup> B. Gross, and P. V. Murphy, "Currents from Gammas Make Detectors and Batteries," *Nucleonics* **19**, 86 (1961).
- <sup>32</sup> "Atomic Battery Lasts for Years," *Popular Science* April 1957, 97.
- <sup>33</sup> R. J. Walko, C. S. Ashley, C. J. Brinker, et al., "Electronic and Photonic Power Application," *Radioluminescent Lighting Technology*, CONF-9009201, 13-1 (1990).
- <sup>34</sup> A. G. Kavetsky, S. P. Meleshkov, and M. M. Sychov, "Conversion of Radioactive Decay Energy to Electricity," In: K. Bower, Y. A. Barbanel, Y. Shreter, G. Bohnert, (Eds.), *Polymers, Phosphors, and Voltaics for Radioisotope Microbatteries*. CRC Press, 39 (2002).
- <sup>35</sup> R. S. Rivenburg, et al., "Power source using a photovoltaic array and self-luminous microspheres," *US Patent* 5,443,657 (1995).
- <sup>36</sup> C.L. Renschler, J.T. Gill, R.J. Walko et al., "Solid State Radioluminescent Lighting," *Radiation Physics and Chemistry* **44** (6), 629 (1994).
- <sup>37</sup> V. M. Andreev, "Nuclear Batteries Based on III-V Semiconductors," In: K. Bower, Y. A. Barbanel, Y. Shreter, G. Bohnert, (Eds.), *Polymers, Phosphors, and Voltaics for Radioisotope Microbatteries*. CRC Press, 39 (2002).
- <sup>38</sup> R. J. Walko, C. S. Ashley, C. J. Brinker, et al., "Electronic and Photonic Power Application," *Radioluminescent Lighting Technology*, CONF-9009201, 13-1 (1990).
- <sup>39</sup> A. G. Kavetsky, S. N. Nekhoroshkov, S. P. Meleshkov, et al., "Radioactive materials, Ionizing Radiation Sources, and Radioluminescent Light Sources for Nuclear Batteries," In: K. Bower, Y. A. Barbanel, Y. Shreter, G. Bohnert, (Eds.), *Polymers, Phosphors, and Voltaics for Radioisotope Microbatteries*. CRC Press, 39 (2002).
- <sup>40</sup> A. G. Kavetsky, S. N. Nekhoroshkov, S. P. Meleshkov, and V. A. Ustinov, "An Efficiency of Energy Conversion Inside Betavoltaic Batteries," *Preprint RI-257* (2001).
- <sup>41</sup> V. Baranov, et al., "Radioactive isotopes as energy sources in photovoltaic nuclear battery based on plasma-dusty structures," *Isotopes, IzdAT* (2000).

- <sup>42</sup> M. Sychov, A. Kavetsky, G. Yakubova, et al., "Alpha indirect conversion radioisotope power source," *Applied Radiation and Isotopes* **66** (2), 173 (2008).
- <sup>43</sup> H. G. J. Moseley, and J. Harling, "The Attainment of High Potentials by the Use of Radium," *Proc. R. Soc. (London) A*, **88**, 471 (1913).
- <sup>44</sup> J. N. Anno, "A Direct-Energy Conversion Device Using Alpha Particles," *Nucl. News*, **6**, 3 (1962).
- <sup>45</sup> E. G. Linder and S. M. Christian, "Use of Radioactive Material for the Generation of High Voltage," *J. Appl. Phys.*, **23**, 11, 1213 (1952).
- <sup>46</sup> P. Rappaport and E. G. Linder, "Radioactive Charging Effects With Dielectrics," *J. Appl. Phys.*, **24**, 9 (1953).
- <sup>47</sup> J. H. Coleman, "Nuclear Energy Sources," *Proc. 12th Annual Battery Research and Development Conf.*, Fort Monmouth, New Jersey, May 1958, 108, Power Source Divisions (1958).
- <sup>48</sup> Y. V. Lazarenko, A. A. Pystovalov, and V. P. Shapovalov, "Desk-Size Nuclear Sources of the Electricity Energy," *Energoatomizdat, Moscow* (1992).
- <sup>49</sup> J. H. Coleman, "Nuclear Batteries," *Proc. 10th Annual Battery Research and Development Conference*, 56, Power Sources Division, Ft. Monmouth, N. J. (1956).
- <sup>50</sup> J. H. Coleman, "Constant Current Charging Type Nuclear Batteries," *Proc. 11th Annual Battery Research and Development Conference*, 106, Power Sources Division, Ft. Monmouth, N. J. (1957).
- <sup>51</sup> J. H. Coleman, "Nuclear Energy Sources," *Proc. 12th Annual Battery Research and Development Conference*, 108, Power Sources Division, Ft. Monmouth, N. J. (1958).
- <sup>52</sup> J. H. Coleman, "Radioisotope High-Potential Low-Current Sources," *Nucleonics*, **11**, 12, 42 (1953).
- <sup>53</sup> W. F. Windle, "Microwatt Radioisotope Energy Converters," *IEEE Transactions on Aerospace*, **2**, 2, 646 (1964).
- <sup>54</sup> G. D. Gorlovoy and E. G. Karbash, "Charging Device With Nuclear Battery," *Atomic Energy*, **4**, 382 (1950).
- <sup>55</sup> J. Braun, L. Fermvik, and A. Stenback, "Theory and Performance of a Tritium Battery for the Microwatt Range," *Journal of Physics E: Scientific Instruments*, **6**, 727 (1973).
- <sup>56</sup> J. R. Lee, G. H. Miley, N. Luo, and M. Ragheb, "Radioisotopic Battery With Vacuum Electrical Insulation," *5th International Energy Conversion Engineering Conference and Exhibit*, St. Louis, Missouri (June 2007)
- <sup>57</sup> J. R. Lee, B. Ulmen, and G. H. Miley, "Honeycomb Betavoltaic Battery for Space Applications," *American Institute of Physics Conference Processing* **969**, 557 (2008).

## CHAPTER 3

### THEORETICAL ESTIMATION OF THE DIRECT CHARGE NUCLEAR BATTERY EFFICIENCY <sup>1</sup>

#### 3.1 EQUATION FOR CALCULATION OF THE EFFICIENCY OF THE DIRECT CHARGE NUCLEAR BATTERY

The efficiency of the nuclear battery is the ratio of the electrical power,  $P_{el}$ , and radioactive decay power,  $P_{RD}$ , of the fuel. We know that  $P_{el}$  has a maximum value at  $R_{load}=R_{cell}$ . In this case

$$I_{load} = \frac{I_{Ch} \cdot R_{cell}}{R_{cell} + R_{load}} = \frac{I_{Ch}}{2} \quad (3.1)$$

Generally,  $I_{Ch}$  will depend on beta particle flux. The charging current is bounded by the charging particles current,  $I_{ChP}$ . Here  $3.7 \cdot 10^{10}$  Bq (1 Ci) of beta radioactivity is equal, by definition, to  $3.7 \cdot 10^{10}$  (electrons/s)  $\cdot 1.6 \cdot 10^{-19}$  C = 5.92 nA.  $I_{Ch}$  approaches  $I_{ChP}$  in the ideal case of a point source and spherical collector. Otherwise,  $I_{Ch}$  is less than  $I_{ChP}$ . The fraction of the beta particle flux which converts to  $I_{Ch}$  is less than full flux of beta particles (which is numerically equal to the isotope activity) due to:

- self absorption of the beta particles into the active layer of the radioactive source. This can be characterized by the efficiency of sources,  $\eta_s$ , which is the ratio of beta particles on the active surface of the source to all beta particles emitted in the source;
- loss of beta particles as they travel from the source to the collector. This can be characterized by a geometrical factor,  $k_g$ . It is the ratio of beta particles flux which reach the collector to the beta particles flux on the active surface of the source;

---

<sup>1</sup> In this Chapter the material from: A. Kavetsky, G. Yakubova et al., "Tritium-Charged Capacitor," *Nuclear Science and Engineering* **159**, 321 (2008) is included. Copyright 2008 by the American Nuclear Society, La Grange Park, Illinois. Permission to reprint at February 3, 2010.



- loss (repulsion) of beta particles due to the increasing high voltage potential on the collector. This can be characterized by a repulsing factor,  $\eta_R(U)$ ;
- Finally, the backscatter and low energy secondary electrons can decrease charging current. This can be characterized by a coefficient of backscattering,  $b$ , and secondary electrons yield,  $s$ .

Then

$$I_{Ch} = q_e \cdot A \cdot \eta_S \cdot k_g \cdot \eta_R(U) \cdot (1-s) \cdot (1-b) \quad (3.2)$$

Efficiency can be represented as

$$\xi = \frac{U \cdot I_{load}}{\varepsilon_{avg} \cdot A} = \frac{U \cdot I_{Ch}}{\varepsilon_{avg} \cdot A \cdot 2} = \frac{1}{2} \cdot \frac{U \cdot \eta_R(U)}{\varepsilon_{avg}} \cdot \eta_S \cdot k_g \cdot (1-s) \cdot (1-b) \quad (3.3)$$

if  $\varepsilon_{avg}$  is measured in electron-volts. The importance of different factors in this equation can be estimated.

## 3.2 FACTORS AFFECTING EFFICIENCY OF DIRECT CHARGE NUCLEAR BATTERY

### 3.2.1 Isotopes for Direct Charge Nuclear Battery

Nearly 3000 radioactive isotopes are known today.<sup>1</sup> Some of them are used in medicine and industry. For each application the radioisotopes must satisfy certain criterions. The same is true for fuel in nuclear batteries.

The radioactive isotopes used in the DCNB should satisfy these conditions:

– First, beta isotopes are preferred because alpha emitters generate copious secondary electrons from the source which are difficult to suppress. To suppress them, a mesh with high negative potential is usually used<sup>2</sup>. This makes construction of the battery more complicated, costly, and larger.

– Second, the isotope half-life should be several months to hundreds of years, to ensure long operating life in comparison with chemical batteries, while also having adequate specific activity. If the isotope has a half life of less than 3-4 month, the maximum engineered battery life will be less than a year. Or, it will be need a very large excess of isotope for prolonged working time. If the half life of the isotope is very long, the specific power will too low for making the battery.

– Third, the radiation hazard of the isotopes should be as low as reasonably achievable. Low photon emission is preferred. Gamma or very strong beta radiation will require extensive shielding to protect personnel and electronics from the radioactive hazard.

Isotopes which best satisfy these conditions include tritium, nickel-63, promethium-147, and strontium-90.

### 3.2.2 Efficiency of sources

The power (specific power) and efficiency of the nuclear battery depend fundamentally on the charging particle current (specific charging particle current) and the efficiency of the external emission of the ionizing radiation sources. Three factors determine the density of the beta particle flux from sources:

- The specific activity of the radioactive isotope in the layer,
- The mass thickness of that formed source layer, and
- Absorption of the beta particles in the protective layer.

#### 3.2.2.1 Beta particle flux and current from the sources

The specific power of the beta particle flux from the source surface can be estimated on the basis of a point beta source function.<sup>3</sup> It describes the distribution of absorbed energy in a homogeneous medium around a small beta source. A point beta source function is determinate through the value  $W(r)$ .<sup>3</sup>  $W(r)$  is the energy absorbed in the spherical layer having radius  $r$ . A working expression for description of  $W(r)$  is given by Equation (3.4):<sup>4</sup>

$$W(r) = 0.25 \cdot W_0 \cdot e^{-10 \cdot r \cdot \nu} + 0.75 \cdot W_0 \cdot e^{-2 \cdot r \cdot \nu} + (\varepsilon_{avg} \cdot \nu - 0.4 \cdot W_0) \cdot r \cdot \nu \cdot e^{-r \cdot \nu} \quad (3.4)$$

where  $r$  is the radius in units of mass thickness,  $\text{mg}/\text{cm}^2$ ;  $\nu$  is the mass absorption coefficient,  $\text{cm}^2/\text{mg}$ ;  $W_0$  is the stopping power near the source,  $\text{keV}\cdot\text{cm}^2/\text{mg}$ . The parameters in Equation (3.4) for tritium, nickel-63, promethium-147, and strontium-90 (with yttrium-90) are given in Table 3.1.

**Table 3.1. Beta particle energy, mass absorption coefficient and stopping power for tritium, Ni-63, Pm-147, and Sr-90<sup>5, 6</sup>**

Isotope	Maximum energy of the beta particles, $\varepsilon_{max}$ , keV	Average energy of the beta particles, $\varepsilon_{avg}$ , keV	The mass absorption coefficient, $\nu$ , $\text{cm}^2/\text{mg}$	Stopping power near the source $W_0$ , $\text{keV}\cdot\text{cm}^2/\text{mg}$
Tritium	18	5.7	15.1	56.6
Ni-63	67	17.4	1.48	30.6
Pm-147	225	62	0.19	13.8
Sr-90	540	198	0.044	5.76
Y-90	2240	930	0.0066	2.31

The equation for calculation of the specific power of the beta particles flux  $\frac{dP(A_{sp}, D)}{dS}$  on the surface of the radioactive isotope contained layer based on the point source function are given in Kavetsky et al.<sup>7</sup> From  $\frac{dP(A_{sp}, D)}{dS}$ , the beta particles current density,  $\frac{dI_{\beta}(A_{sp}, D)}{dS}$ , can be calculated as

$$\frac{dI_{\beta}(A_{sp}, D)}{dS} = \frac{1}{\varepsilon_{avg}} \cdot \frac{dP(A_{sp}, D)}{dS} = \frac{0.08 \cdot A_{sp}}{\varepsilon_{avg}} \int_0^{\pi/2} \sin \theta \cdot \cos \theta \int_0^{D/\cos \theta} \left( \varepsilon_{avg} - \int_0^{\rho} W(r) dr \right) d\rho d\theta \quad (3.5)$$

where  $\frac{dI_{\beta}(A_{sp}, D)}{dS}$  is in nA/cm<sup>2</sup>,  $\varepsilon_{avg}$  is the average energy of the beta particles in keV,  $A_{sp}$  is the specific activity of the radioactive isotope layer, GBq/mg, and  $D$  is the mass thickness of that layer in mg/cm<sup>2</sup>;  $\rho$  and  $\theta$  are a parameters of integration.<sup>7</sup>

### 3.2.2.2 Beta particles current from tritium, Ni-63, Pm-147, and Sr-90 sources

The specific activity of radioactive formations which contain tritium, Ni-63, Pm-147, or Sr-90 may practically be used as beta sources. They are calculated by Equation (3.6) and shown in Table 3.2.

$$A_{sp} = \frac{n \cdot N_A \cdot \lambda}{Mw \cdot 10^{12}}, \text{ GBq/mg} \quad (A_{sp} = \frac{n \cdot N_A \cdot \lambda}{Mw \cdot 3.7 \cdot 10^{13}}, \text{ Ci/mg}) \quad (3.6)$$

where  $n$  is number of atoms in the radioactive isotope in molecules,  $\lambda$  is the decay constant, s<sup>-1</sup>,  $N_A=6.022 \cdot 10^{23}$  mol<sup>-1</sup> is Avogadro's number, and  $Mw$  is the molecular weight, g·mol<sup>-1</sup>.

Radioactive isotope formations uniformly distributed have specific activities reduced from the pure isotope. Therefore, the actual chemical compounds of these isotopes are also considered. Tritium sources for practical application are most commonly used as titanium or scandium tritide.<sup>8, 9, 10</sup> Titanium and scandium can be saturated up to 1100 Ci/g.<sup>8</sup> The practical achievable specific activity of the radioactive isotope contained layer is 1000 Ci/g.<sup>11</sup> The specific activity of the pure Ni-63 is 57 Ci/g. But, metal nickel is always a mixture of the isotopes. It has about 10 Ci Ni-63/g Ni metal.<sup>11, 12</sup> The common chemical compound for Pm-147 is Pm<sub>2</sub>O<sub>3</sub> with a specific activity of 800 Ci/g. Usually sources of promethium-147 are made in enamel. Using enamel as a matrix gives a specific activity of approximately 10 Ci/g in the radioactive layer. The technology developed in TRACE Photonics, Inc., for preparing the Pm-147 sources in silica-titanium sol-gel as binder, increased the specific activity to 400 Ci/g.<sup>13</sup> The chemical compound for Sr-90 is usually Sr(NO<sub>3</sub>)<sub>2</sub> with a specific activity 58 Ci/g. Graphite or ceramic when used as a matrix give 10 Ci/g, or 20 Ci/g. This takes into account that Sr-90 is in secular equilibrium with its Y-90 daughter. Practical achievable specific activities<sup>11, 12</sup> are shown in Table 3.2.

**Table 3.2. Specific activity of the chemical carriers for tritium, Ni-63, Pm-147, and Sr-90 and practical achievable specific activity of radioactive layer**

Parameter	Isotope				
	Tritium	Ni-63	Pm-147		Sr-90
Half-life, yr <sup>5</sup>	12.32	100.1	2.62		28.9
Decay constant, c <sup>-1</sup>	1.78·10 <sup>-9</sup>	2.2·10 <sup>-10</sup>	8.4·10 <sup>-9</sup>		7.6·10 <sup>-10</sup>
Chemical compound	Ti <sup>3</sup> H <sub>2</sub> Sc <sup>3</sup> H <sub>2</sub>	<sup>63</sup> Ni	<sup>147</sup> Pm <sub>2</sub> O <sub>3</sub>		<sup>90</sup> Sr(NO <sub>3</sub> ) <sub>2</sub>
Specific activity of the chemical compound, GBq/mg (Ci/mg)	41 (1.1)	2.1 (0.057)	30 (0.8)		2.1 (0.058)
Matrix or binder	Titanium or scandium	Metallic nickel	Enamel	Silica-titana sol-gel	Graphite, ceramic
Specific activity of the radioactive layer, GBq/mg (Ci/mg)	37 (1.0)	0.37 (0.01)	0.37(0.01)	15 (0.4)	0.37(0.01) (0.74(0.02)) <sup>a</sup>

<sup>a</sup> Including activity of daughter isotope <sup>90</sup>Y in the secular equilibrium with <sup>90</sup>Sr.

Figures 3.1a and 3.1b show how beta particle current density (flux) depend on mass thickness and surface activity for tritium, Ni-63, Pm-147, and Sr-90. Flux is calculated using Equation (3.5). The calculations were made with practical specific activities using current production/separation techniques. As is shown, the practical beta flux for Ni-63 is one to two orders lower than tritium or Pm-147 and Sr-90, with the same mass thickness of the radioactive layer. If we compare Pm-147 and Sr-90 sources, we see the flux is about 4-5 nanoampere per square centimeter (nA/cm<sup>2</sup>) for both isotopes. Sr-90 is a larger radiation hazard than Pm-147 with approximately the same surface activity mostly due to the very strong beta irradiation of Y-90. Therefore, using the Pm-147 is preferable than Sr-90.

Based on these considerations, Pm-147 and tritium were chosen for the present research to build the DCNB.

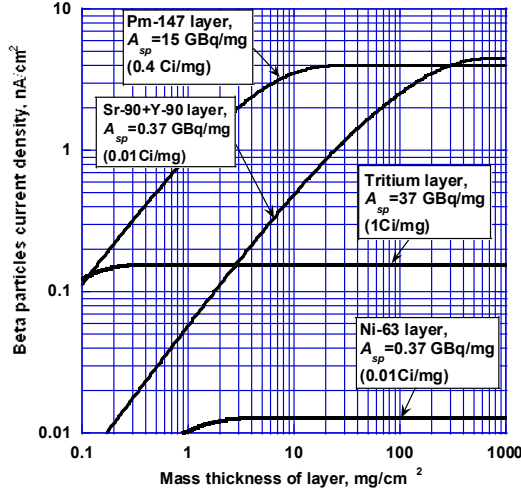


Figure 3.1a. Dependence of beta particle current density on mass thickness of the radioactive isotope layer for tritium, Ni-63, Pm-147, and Sr-90. Specific activities are marked on the plot.

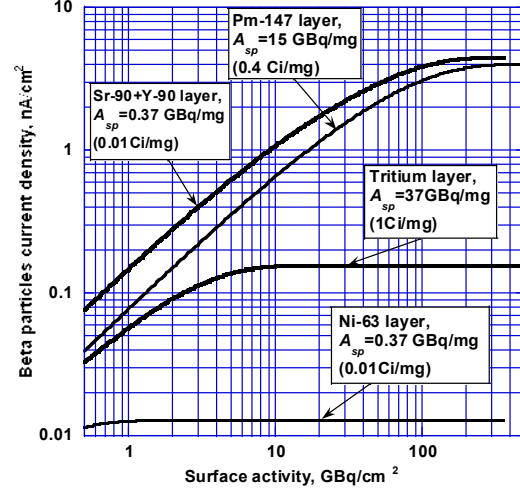


Figure 3.1b. Dependence of beta particle current density on surface activity of the radioactive isotope layer for tritium, Ni-63, Pm-147, and Sr-90. Specific activities are marked on the plot.

### 3.2.2.3. Efficiency of source $\eta_S$ versus thickness of radioactive layer

The efficiency of the source,  $\eta_S$ , depends on thickness (mass thickness,  $D$ ) of radioactive layer of source. Based on calculations of the beta particle current densities using Equation (3.5), calculation of  $\eta_S$  can be made.

$$\eta_S = \frac{1}{q_e \cdot A_{sp} \cdot D} \cdot \frac{dI_\beta(A_{sp}, D)}{dS} \quad (3.7)$$

The dependence of  $\eta_S$  with  $D$  for tritium, having  $A_{sp} = 1$  Ci/mg and for Pm-147 with  $A_{sp} = 0.4$  Ci/mg, were calculated and are plotted in the Figure 3.2. As seen from Figure 3.2, the

efficiency of the source can reach 50%. It's clear that the 50% efficiency is limited by the  $2\pi$  configuration in which half of the flux is directed at the substrate. If beta particle flux from both sides can be used, then the efficiency is doubled (the so-called  $4\pi$ -source). Producing  $4\pi$ -sources from tritium with a mass thickness of approximately  $0.03 \text{ mg/cm}^2$  and from Pm-147 with a mass thickness of approximately  $0.7 \text{ mg/cm}^2$  is possible. Therefore, one can conservatively estimate the possible efficiency of the DCNB source to be 0.7 for tritium and 0.8 for Pm-147.

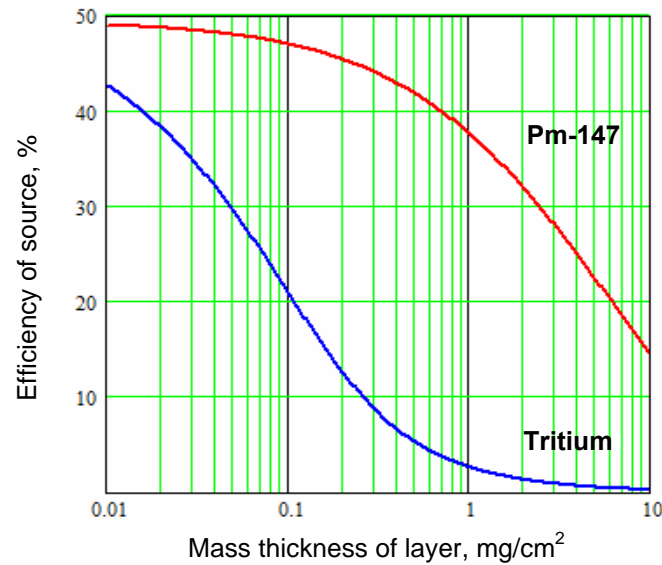


Figure 3.2. Source efficiency vs. mass thickness of the radioactive layer for tritium and Pm-147 using  $2\pi$  geometry

### 3.2.3 Effect of battery geometry

#### 3.2.3.1 Battery with round parallel plane electrodes

Consider a direct charge battery with round plane-parallel electrodes having radius  $R$  (Figure 3.3). One electrode is the source of the beta particles while the second is their collector. The electrodes are separated by a distance  $d$ , and their centers share an axis perpendicular to the planes of the electrodes.

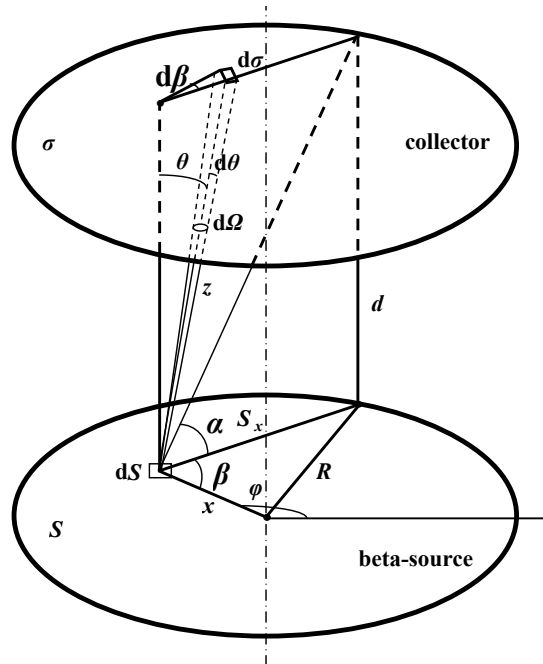


Figure 3.3. Scheme for calculation of the fractional beta flux in parallel plane collectors

Denote the beta particle flux from each element of the surface in the direction determined by the angles  $\theta$  and  $\beta$  as  $\Phi(\theta, \beta)$ . To a first approximation, each element of the surface is a flat Lamberts source. That is,  $\Phi(\theta, \beta) = \Phi_0 \cos \theta$ , where  $\Phi_0$  is the beta particle flux in the direction perpendicular to the element of the surface. One can calculate the beta particle flux  $\Phi$  from the all surfaces of the source in the solid angle  $\Omega$  as



$$\Phi = \int_{S_{source}} \int_{\Omega} \Phi(\theta, \beta) d\Omega dS \quad (3.8)$$

In this equation, with  $\Omega=2\pi$ , total beta particle flux from one side of the source,  $\Phi_{total}$ , is included. The beta particle flux which reaches the collector is designated as  $\Phi_{collector}$ . The geometrical factor  $k_g$  is

$$k_g = \frac{\Phi_{collector}}{\Phi_{total}} \quad (3.9)$$

If one assumes that the beta source uniformly ejects beta particles,  $\Phi_0$  is a constant value. Then it is possible to calculate  $k_g$  as

$$k_g = \frac{\int_{S_{source}} \int_{\Omega} \Phi(\theta, \beta) d\Omega dS}{\int_{S_{source}} \int_{2\pi} \Phi(\theta, \beta) d\Omega dS} = \frac{\int_{S_{source}} \int_{\Omega} \cos \theta d\Omega dS}{\int_{S_{source}} \int_{2\pi} \cos \theta d\Omega dS} \quad (3.10)$$

Taking into account that  $d\Omega = \sin \theta d\theta d\beta$ , then

$$\int_{\Omega} \cos \theta d\Omega = \int_0^{2\pi} \int_0^{\frac{\pi}{2}-\alpha} \cos \theta \cdot \sin \theta d\theta d\beta = \frac{1}{2} \cdot \int_0^{2\pi} \cos^2 \alpha d\beta \quad (3.11)$$

and

$$\int_{2\pi} \cos \theta d\Omega = \int_0^{2\pi} \int_0^{\frac{\pi}{2}} \cos \theta \cdot \sin \theta d\theta d\beta = \pi \quad (3.12)$$

where angles  $\alpha$  and  $\beta$ , as well as  $z$  and  $dS$ , are as designated in Figure 3.3.

Angle  $\alpha$  depends on angle  $\beta$  and on the distance  $x$  between  $dS$  and the centre of the source. Using polar coordinates with the origin at the center of the source one can write

$$dS = x \cdot dx \cdot d\varphi \quad (3.13)$$

Substituting (3.11), (3.12) and (3.13) in (3.10) and integrating, we derive

$$k_g = \frac{1}{2\pi \cdot \pi R^2} \cdot \int_0^R \int_0^{2\pi} \int_0^{2\pi} \cos^2 \alpha \cdot x \cdot d\beta d\varphi dx = \frac{1}{\pi R^2} \cdot \int_0^R \int_0^{2\pi} \cos^2 \alpha \cdot x \cdot d\beta dx \quad (3.14)$$

The dependence of distance  $S_x$  between  $dS$  and the edge of a source from  $x$  and angle  $\beta$  can be written as

$$S_x = x \cdot \cos \beta + \sqrt{R^2 - x^2 \cdot \sin^2 \beta} \quad (3.15)$$

and

$$\cos \alpha = \frac{S_x}{\sqrt{S_x^2 + d^2}} \quad (3.16)$$

The calculated result for  $k_g$  is displayed in Figures 3.4a and 3.4b. Not surprisingly, the fraction of beta particle flux which reaches a collector decreases with an increased distance between electrodes, and increases as the radii of electrodes increases.

For example, a source with a radius of 5 cm and a distance to collector of 5 mm, only 90% of the emitted beta particle flux will reach the collector. This estimate assumes that the beta source uniformly ejects beta particles and each element of the surface of the beta source is a Lambert's Source. For a real source, surface distribution of the flux is not completely uniform and angular distribution of the flux may vary from a Lambert's source. Therefore,  $k_g$  is estimated conservatively.

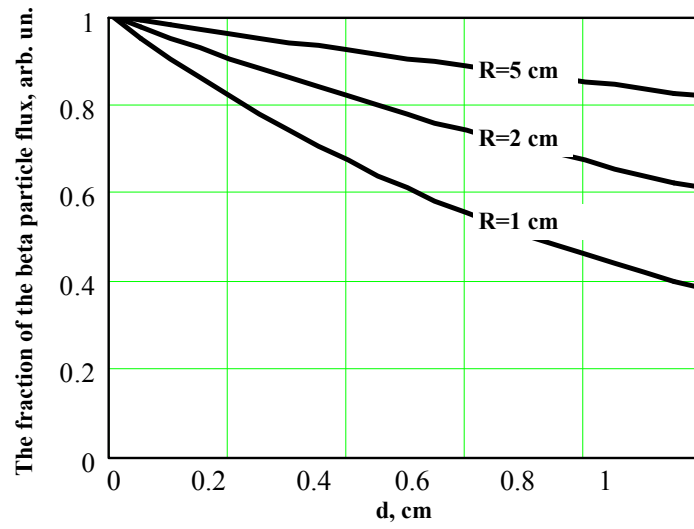


Fig. 3.4a. Beta flux reaching collector for different distances between source and collector and various radii of source (and collector)

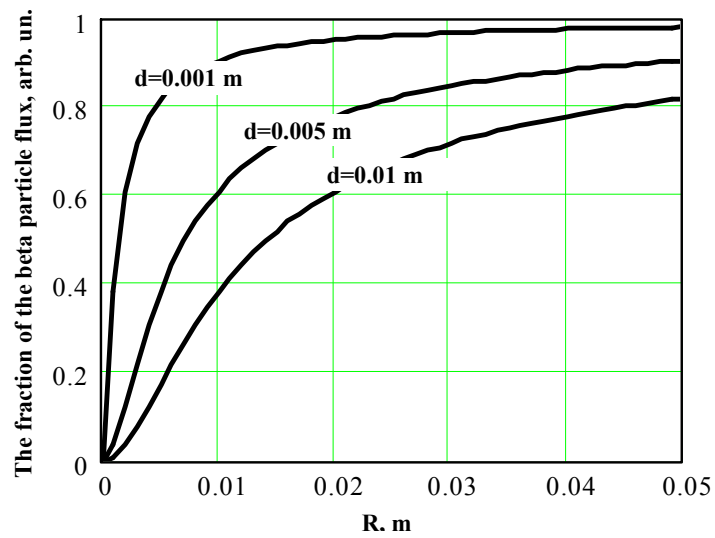


Fig. 3.4b. Beta flux reaching a collector based on different electrode radii and distances between source and collector

### 3.2.3.2 Battery with cylindrical collector and flat rectangular source

The scheme for calculation of the beta flux fraction in a direct charge cell with cylindrical collector and flat rectangular source are shown in Figure 3.5. In this case the calculation of the fraction of beta particle flux which reach the collector ( $k_g$ ), for simplicity and clarity, was made for a rectangular source with width,  $w$ . This is much less than the diameter of the cylindrical collector.

As shown in Figure 3.5, dependence of  $\cos\alpha$  on angle  $\beta$  and coordinates of the elements of the source surface  $dS$  can be written in terms of angles  $\alpha$  and  $\beta$ , as well as the  $L$ -length of the collector and source,  $R_{cyl}$ -radii of collector. They are also in terms of  $y$  and  $dS$ , as designated in Figure (3.3) by Equations (3.17).

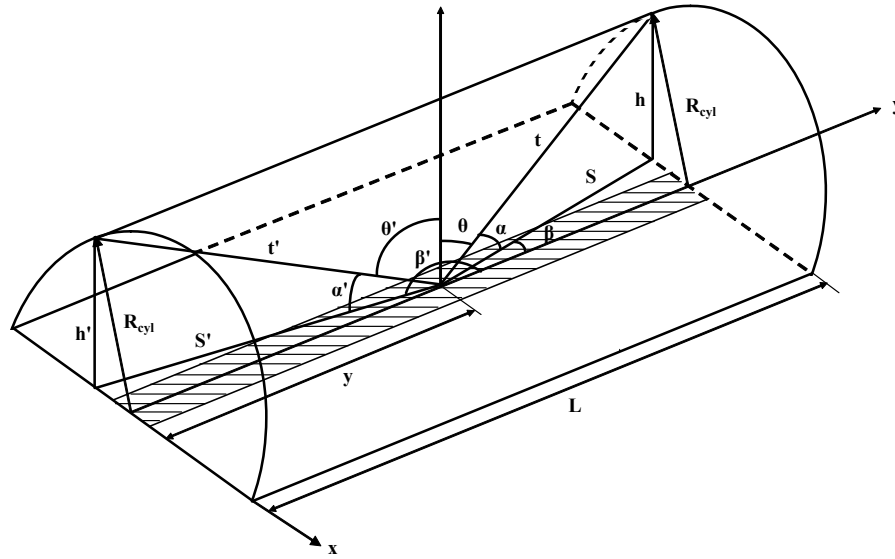


Figure 3.5. Scheme for calculation of the beta flux fraction in a direct charge battery with cylindrical collector and flat rectangular source

$$\begin{aligned}
\cos \alpha &= \frac{L-y}{\cos \beta} \cdot \frac{1}{\sqrt{R_{cyl}^2 + (L-y)^2}} \quad \text{for} \quad 0 \leq \beta \leq \arctan \frac{R_{cyl}}{L-y} \\
\cos \alpha &= 1 \quad \text{for} \quad \arctan \frac{R_{cyl}}{L-y} \leq \beta \leq \pi - \arctan \frac{R_{cyl}}{L-y} \\
\cos \alpha &= \frac{y}{\cos(\pi - \beta)} \cdot \frac{1}{\sqrt{R_{cyl}^2 + y^2}} \quad \text{for} \quad \pi - \arctan \frac{R_{cyl}}{L-y} \leq \beta \leq \pi \\
\cos \alpha &= \frac{y}{\cos(\beta - \pi)} \cdot \frac{1}{\sqrt{R_{cyl}^2 + y^2}} \quad \text{for} \quad \pi < \beta \leq \pi + \arctan \frac{R_{cyl}}{y} \\
\cos \alpha &= 1 \quad \text{for} \quad \pi + \arctan \frac{R_{cyl}}{y} < \beta < 2\pi - \arctan \frac{R_{cyl}}{L-y} \\
\cos \alpha &= \frac{L-y}{\cos(2\pi - \beta)} \cdot \frac{1}{\sqrt{R_{cyl}^2 + (L-y)^2}} \quad \text{for} \quad 2\pi - \arctan \frac{R_{cyl}}{L-y} \leq \beta \leq 2\pi
\end{aligned} \tag{3.17}$$

For Cartesian coordinates as in this case,  $dS=dx \cdot dy=w \cdot dy$ , where  $w \ll 2R_{cyl}$ .

Substitute (3.11) and (3.12) in (3.10) and integrate to give

$$k_g = \frac{1}{2\pi \cdot L} \cdot \int_0^L \int_0^{2\pi} \cos^2 \alpha \cdot d\beta dy \tag{3.18}$$

Calculated dependencies using equation (3.18) for the fraction of beta particles flux which reach the collector with  $L$  for radii of collector equal 1, 2, 3 cm as shown in Figure 3.6.

For example, for a collector of radius 2 cm and length 10 cm, about 90% of the emitted beta particle flux will reach the collector. This estimate also assumes that the beta source uniformly ejects beta particles. For a real source, surface distribution of the flux is not strongly uniform. Therefore, we have estimated  $k_g$  conservatively.

For spherical geometry this factor is very close to one.

We take, for estimation, the possible efficiency of DCNB to be a value of the geometrical factor  $k_g=0.95$ .

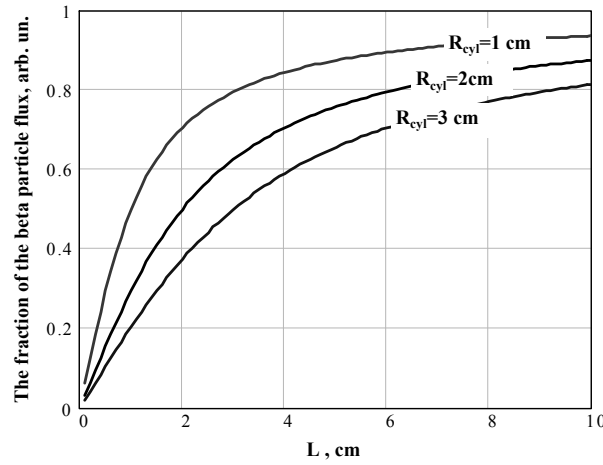


Figure 3.6. Beta flux reaching collector with length of source and collector for various radii of collector

### 3.2.4 Effect of electrostatic repulsion

The effect of accumulated voltage between electrodes on  $\eta_R(U)$  is considered next. The voltage will increase as a result of the negative collector charge accumulation. This results in increasing repulsion of the incoming beta particles. If the energy of beta particles moving through the growing potential field between the electrodes of a battery is less or equal to that field, those beta particles cannot reach the collector. If the particle energy is greater than the product of voltage on a collector and an elementary charge, and the particle is moving under an angle to the source surface, then under action of the electric field will deviate from its initial rectilinear trajectory. Increasingly fewer beta particles will reach the charging collector compared to the collector at its zero starting voltage.

Any source of beta particles has a specific distribution of energy. In the case of tritium, the beta particle distribution can be represented as:<sup>14</sup>

$$w(\varepsilon_\beta)d\varepsilon_\beta = k_n \cdot (\varepsilon_{\max} - \varepsilon_\beta)^2 \left\{ 1 - \exp\left(-\frac{1.47}{\sqrt{\varepsilon_\beta}}\right) \right\}^{-1} d\varepsilon_\beta \quad (3.19)$$

where  $k_n = 1/4120$  is the constant normalizing factor and  $\varepsilon_{\max} = 18.6 \text{ keV}^{15}$  is the maximum energy of tritium beta particles.

In the case of Pm-147, the beta energy spectrum was calculated from Fermi–Curie data as given in Langer et al. (1950).<sup>16</sup>

The path of beta particle  $\eta(U)$  with energy greater than  $q_e \cdot U$ , which can consequently reach the collector, where  $q_e$  is the elementary charge, and  $U$  is the voltage on the collector, is given by:

$$\eta(U) = \int_{qU}^{\varepsilon_{\max}} w(\varepsilon_{\beta}) d\varepsilon_{\beta} \quad (3.20)$$

The beta energy spectrums and dependencies calculated with Equation (3.20) are plotted on Figure 3.7 and Figure 3.8. For the cylindrical battery geometry  $\eta_R(U) = \eta(U)$ .

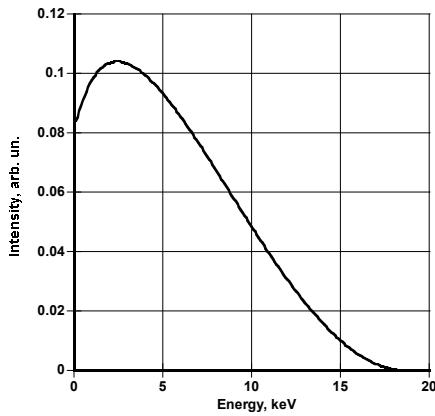


Figure 3.7a. Beta particles spectrum of tritium. Spectrum calculated by Equation (3.19)

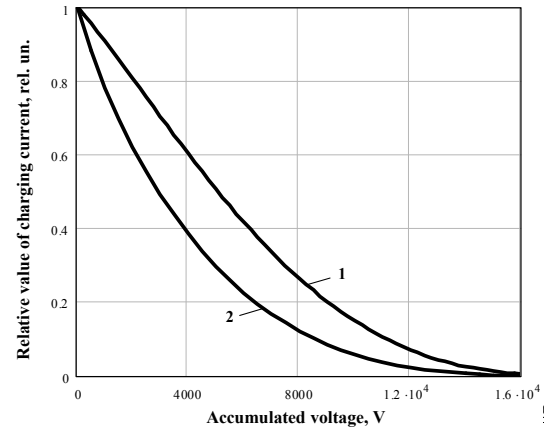


Figure 3.7b. Fraction of tritium beta particles flux reaching collector with accumulated voltage. Curve 1 calculated using Equation (3.20); Curve 2 calculated using Equation (3.38) for the case of electrodes with 5cm radii separated by 5 mm

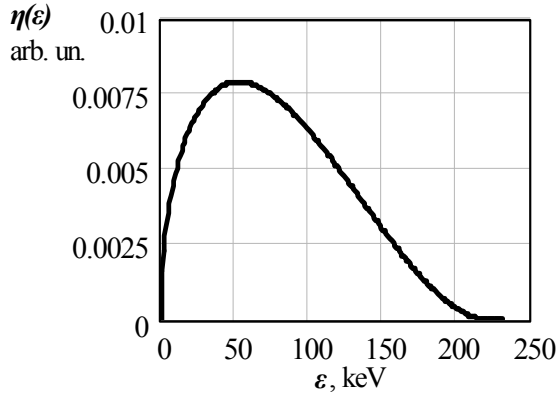


Figure 3.8a. Beta energy spectrum of Pm-147 calculated from Fermi-Curie data as given Langer (1950)<sup>16</sup>

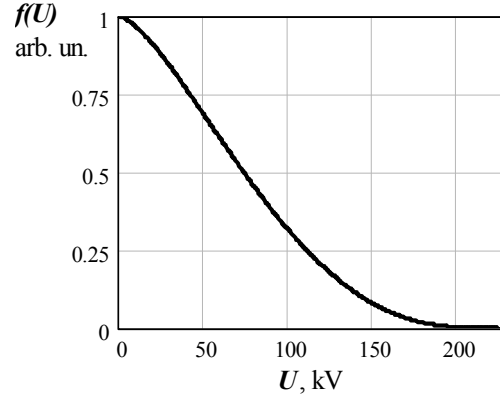


Figure 3.8b. Fraction of Pm-147 beta flux reaching collector with accumulated voltage

For parallel plane battery geometry, it is necessary to include the electrical field as it affects electron trajectories that miss the collector plates (Figure 3.9, Case 1, 4). For these central cases, Equation (3.14) was used. The critical angle  $\alpha$  under which emitted beta particles will still reach a collector depends not only on position,  $dS$ , on the surface of the source, but also on the voltage of the collector. A plane on which the angle  $\alpha$  lies was considered. The trajectory of the charged particle in an electric field is parabolic. The maximum trajectory depends on its origin in the source and the magnitude of the electrical field. Different cases were considered. When the magnitude of the electrical field is not large, the maximum point of the parabola lies outside of the collector (Figure 3.9a). When the magnitude of the electrical field is large, the maximum of the parabola lies inside of the collector (Figure 3.9b). If the angle of the beta particle emission is less than  $\alpha$ , the particle will miss the collector (case 1 in Figure 3.9a and Case 4 in Figure 3.9b). In case 2 (Figure 3.9a) and case 3 (Figure 3.9b) the beta particle will reach the collector.



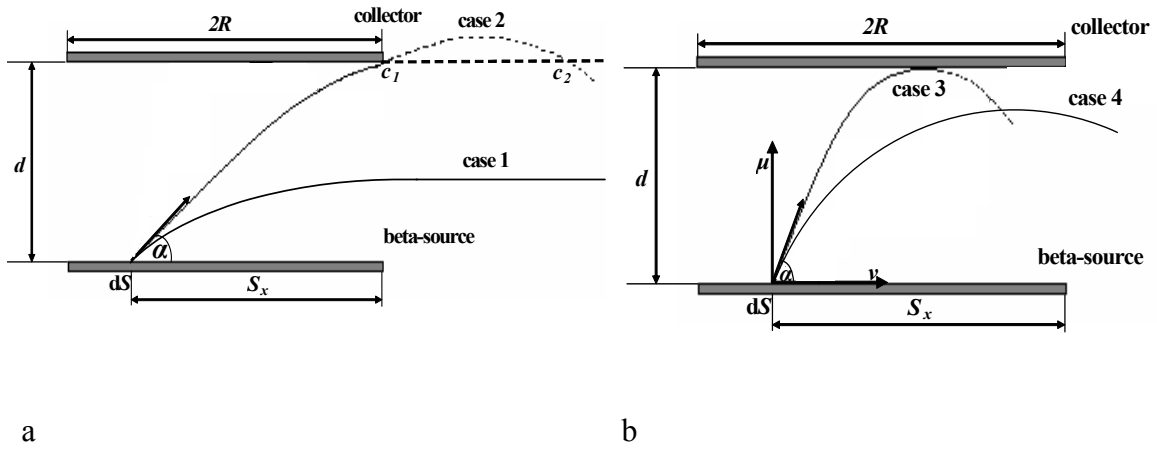


Figure 3.9. Effect of building collector potential on the trajectories of beta particles.

a) low potential on the collector; b) the collector potential can have significant influence on the beta particles.

In the first case (Figure 3.9a), the value of the critical angle at which the beta particle still reaches the collector is determined by the boundary conditions

$$S_x = V \cdot \cos \alpha \cdot t \quad (3.21)$$

$$d = V \cdot \sin \alpha \cdot t - \frac{a \cdot t^2}{2} \quad (3.22)$$

where  $t$  is the moment of beta particle emission in seconds and  $V$  is the initial speed of the beta particle in meters per second:

$$V = \sqrt{\frac{2 \cdot \varepsilon_\beta}{m_e}} \quad (3.23)$$

$\varepsilon_\beta$  is the energy of the beta particle (Joules),  $m_e$  is the mass of an electron ( $9.1 \cdot 10^{-31}$  kg), and  $a$  is the acceleration of the beta particle caused by the interaction with the electric field ( $\text{m/s}^2$ ) determined with the formula:

$$a = \frac{q_e}{m_e} \cdot \frac{U}{d}, \quad (3.24)$$

$q_e$  is the electronic charge ( $1.6 \cdot 10^{-19}$  C);  $U$  is the voltage between electrodes (volts).

From Equations (3.21) and (3.22)

$$d = S_x \cdot \operatorname{tg} \alpha - \frac{a \cdot S_x^2}{2 \cdot V^2 \cdot \cos^2 \alpha} \quad (3.25)$$

And taking into account that  $\cos^2 \alpha = \frac{1}{1 + \operatorname{tg}^2 \alpha}$

$$S_x \cdot \operatorname{tg} \alpha - \frac{a \cdot S_x^2}{2 \cdot V^2} \cdot (1 + \operatorname{tg}^2 \alpha) = d \quad (3.26)$$

Solving Equation (3.26), one gets two values of a root:

$$\operatorname{tg} \alpha_{1,2} = \frac{S_x \pm \sqrt{S_x^2 - 2 \cdot \frac{a \cdot S_x^2}{V^2} \cdot \left( \frac{a \cdot S_x^2}{2 \cdot V^2} + d \right)}}{\frac{a \cdot S_x^2}{V^2}} \quad (3.27)$$

For these values, the trajectory of the electron movement crossing the collector plane is the point  $c_l$  (see Figure 3.9a). For larger roots, the electron misses the collector. The smaller value of  $\operatorname{tg} \alpha$  corresponds to case 2. Therefore, expression (3.27) should use the negative root.

It is possible to determine the critical angle  $\alpha$  using:

$$\alpha = \arctg \left( \frac{V^2 \cdot S_x - \sqrt{(V^2 \cdot S_x)^2 - a \cdot S_x^2 \cdot (a \cdot S_x^2 + 2 \cdot V^2 \cdot d)}}{a \cdot S_x^2} \right) \quad (3.28)$$

In the second case (Figure 3.9b), the critical angle gives the maximum trajectory in which the electron can reach the collector. Particles with a starting angle that is less than their critical angle will not reach the surface of the collector (Case 4 Figure 3.9b). Below shows the planes of an angle  $\alpha$  and rectangular coordinates ( $v, \mu$ ) with origin  $dS$  (Figure 3.9b). The trajectory of beta particles from an angle  $\alpha$  can be written as

$$v = V \cdot \cos \alpha \cdot t \quad (3.29)$$

$$\mu = V \cdot \sin \alpha \cdot t - \frac{a \cdot t^2}{2} \quad (3.30)$$

From Equations (3.29) and (3.30)

$$\mu = v \cdot \operatorname{tg} \alpha - \frac{a \cdot v^2}{2 \cdot V^2} \cdot (1 + \operatorname{tg}^2 \alpha) \quad (3.31)$$

If the point of maximum trajectory coincides with the collector plane of a collector:

$$\frac{d\mu}{dv} = \operatorname{tg} \alpha - \frac{a \cdot v}{V^2} \cdot (1 + \operatorname{tg}^2 \alpha) = 0 \quad (3.32)$$

$$d = v \cdot \operatorname{tg} \alpha - \frac{a \cdot v^2}{2 \cdot V^2} \cdot (1 + \operatorname{tg}^2 \alpha) \quad (3.33)$$

From Equations (3.32) and (3.33)

$$\operatorname{tg} \alpha = \sqrt{\frac{2 \cdot a \cdot d}{V^2 - 2 \cdot a \cdot d}} \quad \text{or} \quad \alpha = \operatorname{arctg}\left(\sqrt{\frac{2 \cdot a \cdot d}{V^2 - 2 \cdot a \cdot d}}\right) \quad (3.34)$$

$$v = \frac{V^2 \cdot \operatorname{tg} \alpha}{a \cdot (1 + \operatorname{tg}^2 \alpha)} \quad (3.35)$$

Thus the angle  $\alpha$ , in the second case represented in Figure 3.9b, is determined by the Expression (3.34). Thus, the following condition should be satisfied

$$v = \frac{V^2 \cdot \operatorname{tg} \alpha}{a \cdot (1 + \operatorname{tg}^2 \alpha)} \leq S_x \quad (3.36)$$

From Equations (3.34) and (3.36)

$$\sqrt{\frac{2 \cdot d \cdot (V^2 - 2 \cdot a \cdot d)}{a}} \leq S_x \quad (3.37)$$

If this condition is not satisfied, the situation reduces to the first case.

Then, Equation (3.14) for calculation of the fraction of beta particles reaching the collector takes into account the tritium beta particle energy spectrum (Equation 3.19) and repulsion of beta particles by accumulated voltage can be rewritten as

$$\eta = \int_0^{\varepsilon_{\max}} w(\varepsilon_{\beta}) \frac{1}{\pi R^2} \cdot \int_0^R \int_0^{2\pi} \cos^2 \alpha \cdot x \cdot d\beta dx d\varepsilon_{\beta} \quad (3.38)$$

where  $\alpha$  is determined by Expressions (3.28) or (3.34).

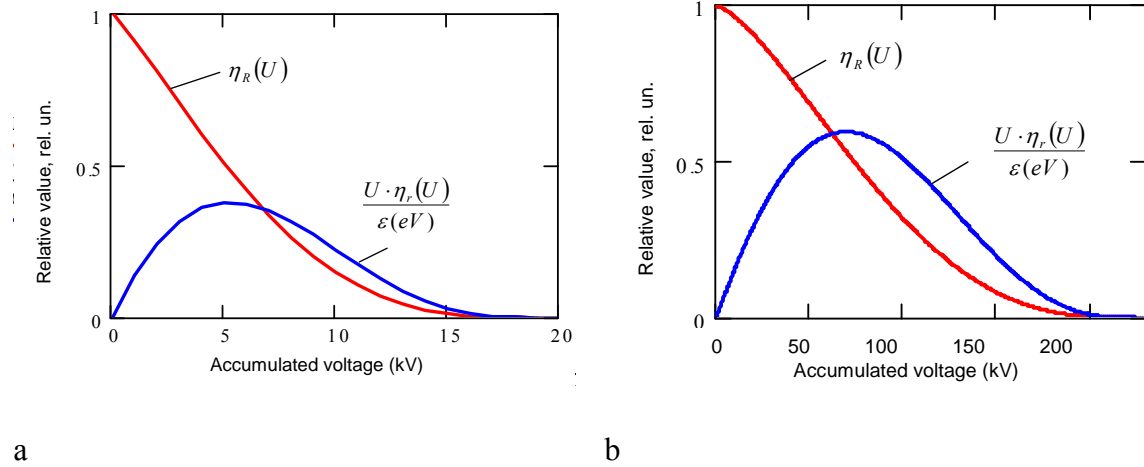
Equation (3.38) describes the dependence of the fraction of the beta particles that can reach the collector not only based on battery geometry, but from voltage on the collector. This dependence can be taken as  $\eta_R(U)$  for the parallel plane battery.

The fraction of tritium beta particle flux reaching the collector with accumulated voltage, with electrodes of 5 cm radii and distance between source and collector of 5 mm, was calculated using Equation (3.38). Results are graphed in Figure 3.8b, curve 2. This fraction decreases with increasing voltage between electrodes. As the voltage on the collector approaches 15 kV, the fraction is almost zero. For the parallel plane battery, the accumulating electric field inhibits a growing fraction of the beta flux from reaching the collector.

As seen from Figure 3.8b, the difference between these two ways of calculating changing beta flux reaching the collector with accumulated voltage is not significant. Therefore, for future calculations and for processing experimental data the first approach was used, as it is easier.

Taking this factor into account, the ratio  $\frac{U \cdot \eta_R(U)}{\varepsilon(eV)}$  in Equation (3.3) was looked at next. This ratio will initially increase  $\xi$  as voltage increases, and then reduce  $\xi$  above a certain voltage, accounting for the dropping  $\eta_R(U)$ . Results of calculation  $\eta_R(U)$  and  $\frac{U \cdot \eta_R(U)}{\varepsilon(eV)}$  with  $U$  are represented in Figure 3.10a, b. As shown, the  $\frac{U \cdot \eta_R(U)}{\varepsilon(eV)}$  has a maximum value

near 0.45 for a tritium cell, and near 0.6 for a Pm-147 cell. These values were then used as efficiency estimates.



a

b

Figure 3.10.  $\eta_R(U)$  and  $\frac{U \cdot \eta_R(U)}{\varepsilon(eV)}$  vs. accumulated voltage for tritium (a) and Pm-147 (b) battery

The decreasing current with accumulated voltage on the collector should be taken into account as  $I_{Ch} = I_{sc} \cdot \eta_R(U)$ . Then the charging Equation (2.3) becomes:

$$\frac{dU(t)}{dt} + \frac{U(t)}{R_{leak} \cdot C} = \frac{I_{sc} \cdot \eta_R(U)}{C} \quad (3.39)$$

Numerical solutions of Equation (3.39) describe the voltage on the collector of DCNB when  $q_e \cdot U$  and are comparable with  $\varepsilon_{avg}$  of the used isotope.

### 3.2.5 Effect of secondary electron emission

Secondary emission is a phenomenon where primary incident particles of sufficient energy hitting a surface or passing through some material induce the emission of secondary particles. If the secondary particles are electrons, the effect is termed secondary electron emission.<sup>17</sup> Secondary emission is characterized by secondary electron yield, that is, the number of secondary electrons (SE) emitted per incident primary. The emission of secondary

electrons can be described with three processes: excitation of the electrons in the solid into high-energy states by the impact of high-energy primary electrons, transport of these SE to the solid surface, and escape of the electrons over the surface barrier into the vacuum. The secondary electrons have a mean escape depth of about 0.5-1.5 nm from metal and 10-20 nm from insulators. Therefore, SE emission are influenced by very thin surface layers.<sup>18</sup> The efficiency of the secondary emission yield varies for different materials, the energy of incident particles, and the roughness of the surface.<sup>19</sup> The general view of the SE energy distribution for primary electron energy ( $E_{PE}$ ) 100-1000 eV is shown in Figure 3.11.<sup>3</sup> Traditionally the secondary electrons are divided into two groups: those with energy less than 50 eV (Figure 3.11 - SE) and electrons with energy from 50 eV to  $E_{PE}$  – inelastic backscattering and reflected electrons (RE). Contribution of the RE electrons in the total number of SE for primary electron with energy less than 200 keV is not more than 25%, and very rapidly decrease with decreasing  $E_{PE}$ . These also decrease with decreasing atomic number of material (Figure 3.12).<sup>20</sup>

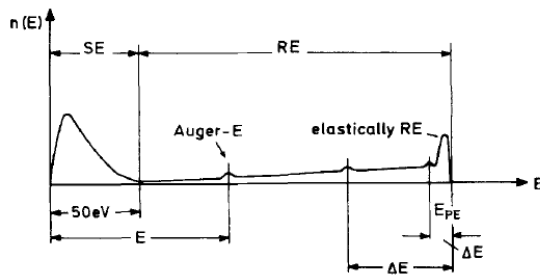


Figure 3.11.<sup>19</sup> General view of the secondary electrons energy distribution

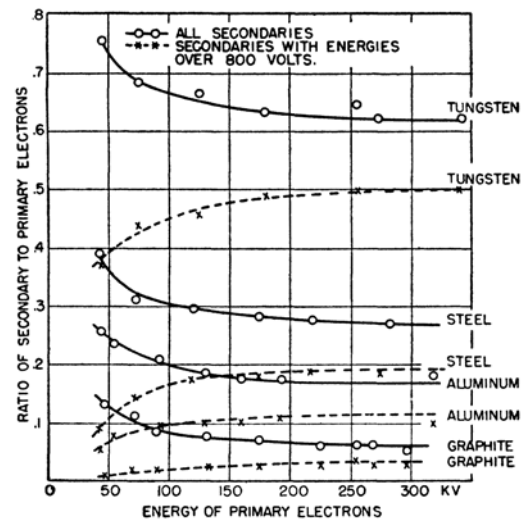


Figure 3.12.<sup>20</sup> Secondary electron emission by electrons with energy up to 340 keV

For insulators, SE distribution has an asymmetric bell-like type with a major peak energy  $E_{SE}^m$  and full width at half maximum (HW), and steady decay in intensity up to a 50 eV cut-off energy.<sup>21</sup> A comparison of the secondary electron energy spectrum of metal and insulator surfaces is shown in Figure 3.13. As shown, the SE yields for insulators are less than for metal and the SE energy is also approximately two times smaller. This is explained by the weaker electronic bonds in organic molecules compared with the electronic bonds in metal atoms.<sup>22</sup>

Secondary electrons produced in the nuclear battery fall into the accelerating electric field and create a counterproductive electron current in the opposite direction of the main beta particles current. Therefore, the collector material chosen should have the lowest SE yield (SEY), or the collector can be covered a low SE emission material, or have a treatment.

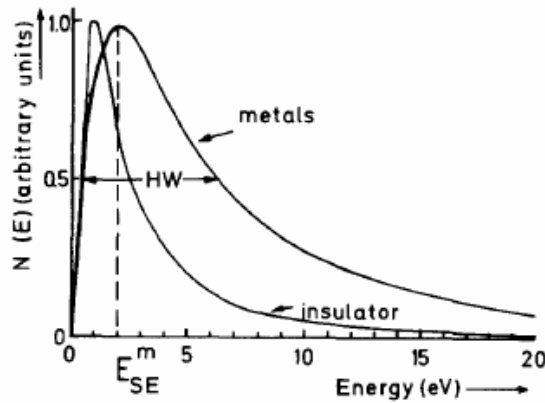


Figure 3.13. Energy distribution of SE from metal and insulator surface<sup>18</sup>

The dependences of SEY on primary electron energy for aluminum, polyethylene, carbon and Kapton, as taken from the database by D.C. Joy<sup>23</sup>, are shown in Figure 3.14.

A carbon or polyimide (Kapton) coating on the aluminum collector reduces the SE yield from 0.5 to 0.17 for primary electron energy of 6 keV (tritium beta particles average energy); and from 0.06 to 0.03 for primary electron energy of 60 keV (prometium-147 beta particles average energy). For metals with a higher atomic number, like copper or iron, the SEY is large compared with aluminum.<sup>20</sup> Therefore, a carbon or polyimide coating gives an even greater advantage.

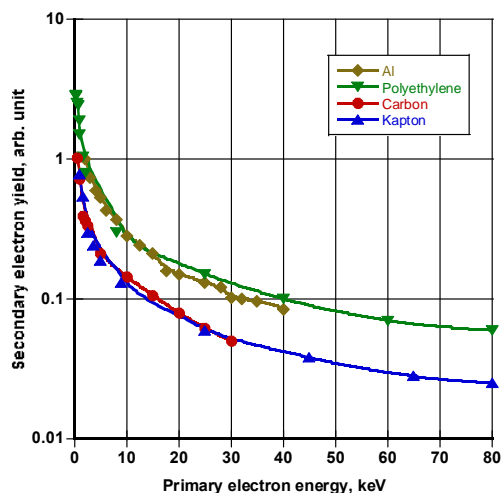


Figure 3.14. The dependence of SEY on primary electron energy for different materials

J. Cazaux<sup>24</sup> created a new dependence model of SEY on primary electron energy for polymers and collected some data for different polymers (see Table 3.3). It shows that polyimide has the lowest yield for a primary electron energy of 5 keV.

**Table 3.3. Secondary electron yield (arb. unit) for primary electron energy 5 keV<sup>24</sup> in polymers considered as suitable candidates for suppressing coating**

PET	Polystyrene	PTFE	Nylon	PMMA	Polyimide
0.3	0.3	0.5	0.6	0.7	0.15

Boron nitride is widely used for coating internal metal surfaces in vacuum devices for reducing SE emission. Yu. G. Malynin<sup>25</sup> had shown that this coating can reduce SE two fold on aluminum. Data from D.C. Joy<sup>23</sup> gives approximately the same coefficient of SE emission for boron nitride as for carbon. So, boron nitride can also be considered a suitable material for collector coating.

Another possible way to lower the SE yield is to change the surface roughness. This indirectly causes a reduction in the emissions from the surface since the solid angle for electrons to escape without further interaction with escape surface is significantly reduced. Y.V. Lazarenko<sup>6</sup> added roughness to aluminum and carbon surfaces and reduced SEY from promethium-147 beta particles irradiation two-fold.



V. Baglin et al.<sup>26</sup> experimented on reducing the SEY of copper. The first step was the oxidation of copper in air at 350°C, which reduced SE 1.2 times. Further increasing the surface roughness was made (see Figure 3.15<sup>26</sup>) to reduce SEY three to five fold for SE energy 0.5-2 keV (see Figure 3.16<sup>26</sup>). An analogous result was received by N. Hilbert et al.<sup>27</sup>

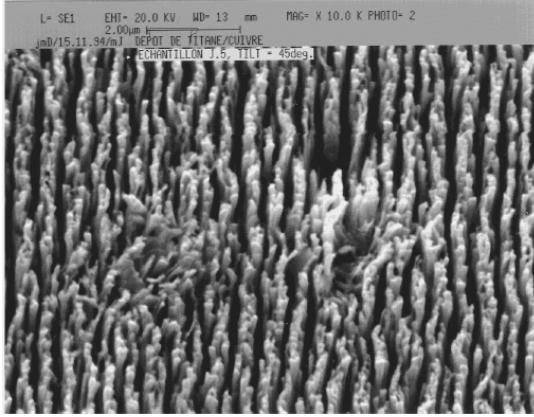


Figure 3.15. Photograph of a textured copper surface<sup>26</sup>

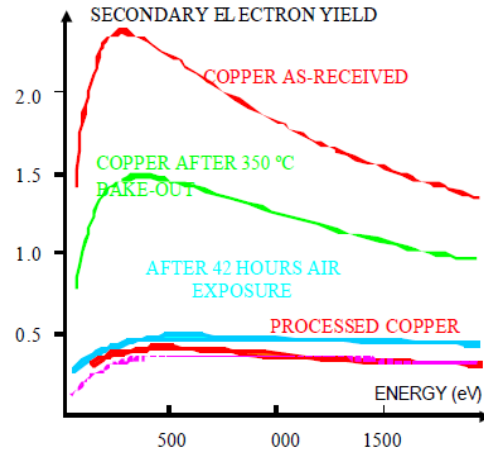


Figure 3.16. SEY of a textured copper surface<sup>26</sup>

Based on these considerations, the value of SEY  $s=0.17$  for tritium NB, and  $s=0.03$  for promethium-147 NB at estimation of the theoretical efficiency of NB were used.

### 3.2.6 Effect of backscattering

Backscattered electrons (BSE) are electrons reflected or back-scattered out of the specimen interaction volume by elastic scattering interactions with specimen atoms.<sup>28</sup> There are several approaches to the theory of backscattering which provide semi-empirical equations to approximate the experimental data for particular ranges of atomic number and primary electron energy.<sup>29,30,31</sup> What was important this research is that the BSE coefficient ( $b$ ) increases with higher effective atomic number  $Z_{eff}$  of reflected surface material.

For estimation of BSE the coefficient, we can use this formula<sup>32</sup>

$$b = \frac{\ln(Z_{eff})}{6} - 0.25 \quad (3.40)$$

Clearly, it is better to use a low atomic number material for the collector and a high atomic number material for the beta source substrate. The results from calculations of the BSE coefficient by Monte Carlo method (program Casino) for aluminum, molybdenum, iron, carbon, and Kapton are shown in Figure 3.17. Applying the carbon or polyimide coating on collectors reduced the BSE coefficient to 0.05 for primary electron energy 6 keV (tritium beta particles average energy); and to 0.03 for primary electron energy 60 keV (Pm-147 beta particles average energy). Using metal substrate for sources with higher atomic numbers may increase the number of outgoing beta particles to 0.5 for tritium beta particles and to 0.3 for promethium beta particles, while the energy of the BSE will be less than the primary electron energy by about 0.1.<sup>33</sup>

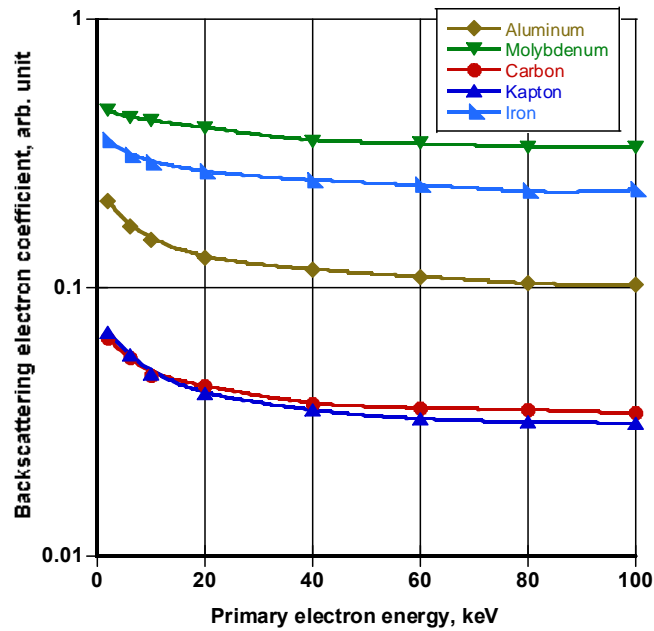


Figure 3.17. The BSE coefficient with changing primary electron energy for different materials

We therefore take the value of BSE coefficient ( $b$ ) to be 0.05 for tritium NB, and 0.03 for promethium-147 NB for estimation of the theoretical efficiency of battery.

### 3.3. ESTIMATION OF THE THEORETICAL EFFICIENCY OF DIRECT CHARGE NUCLEAR BATTERY

The above estimated factors are given in Table 3.4.

**Table 3.4 Values of factors have effect on tritium and Pm-147 nuclear battery efficiency**

Factor influencing efficiency of NB	Tritium NB	Pm-147 NB
Efficiency of source (for $4\pi$ geometry), $\eta_s$	0.7	0.8
Geometrical factor, $k_g$	0.95	0.95
Effect of accumulated voltage, $\frac{U \cdot \eta_R(U)}{\mathcal{E}_{avg}}$	0.45	0.60
Secondary electron yield, $s$	0.17	0.03
Backscattering yield, $b$	0.05	0.03

Equation (3.3) gives the following values for theoretical efficiency:

For tritium NB:

$$\xi = \frac{1}{2} \cdot \frac{U \cdot \eta_R(U)}{\mathcal{E}_{avg}} \cdot \eta_s \cdot k_g \cdot (1-s) \cdot (1-b) = \frac{1}{2} \cdot 0.45 \cdot 0.7 \cdot 0.95 \cdot 0.87 \cdot 0.95 = 0.12 \quad (3.41)$$

For Pm-147 NB:

$$\xi = \frac{1}{2} \cdot \frac{U \cdot \eta_R(U)}{\mathcal{E}_{avg}} \cdot \eta_s \cdot k_g \cdot (1-s) \cdot (1-b) = \frac{1}{2} \cdot 0.60 \cdot 0.8 \cdot 0.95 \cdot 0.97 \cdot 0.97 = 0.21 \quad (3.42)$$

### 3.4. DIRECTIONS OF RESEARCH

Based on the considerations above, a practical Direct Charge Nuclear Battery could benefit from more thorough work in these research areas:

- Experimental making and testing of the Direct Charge Nuclear Battery using tritium and promethium-147 radioactive sources. In such DCNB high efficiency beta sources, suppression of backscatter and secondary electron outlet collector's coating and vacuum spacer as dielectric should be used. The main purpose of this research area is to experimentally confirm the theoretical estimation of the efficiency of DCNB, and determine the possibilities of making DCNB with an efficiency comparable to RTG efficiency (5-10%). DCNB optimization characteristics must be considered.
- The second direction is the investigation of the possibility of using a solid dielectric instead of a vacuum. Experimental fabrication and testing parameters of the tritium nuclear battery with solid dielectric would be explored.
- Experimental testing and determination of the possible DCNB applications (for instance, power supply for flash lamp, photomultiplier and others).

### REFERENCES

- <sup>1</sup> J. K. Shultis, and R. E. Faw, "Fundamentals of Nuclear Science and Engineering," CRC Press (2007).
- <sup>2</sup> J. N. Anno, "A Direct-Energy Conversion Device Using Alpha Particles," *Nucl. News*, **6**, 3 (1962).
- <sup>3</sup> V. I. Ivanov, "A Dosimetry Course," Energoatomizdat, Moscow (1988) [Russian].
- <sup>4</sup> V. V. Bochkarev, G. B. Radsievsky, L. V. Timofeev, and N. A. Demianov, "Distribution of absorbed energy from a point beta source in a tissue-equivalent medium," *Int. J. of Applied Radiation and Isotopes*, **23**, 493 (1972).
- <sup>5</sup> <http://www.nndc.bnl.gov/chart/chartNuc.jsp>
- <sup>6</sup> Y. V. Lazarenko, A. A. Pystovalov, and V. P. Shapovalov, "Desk-Size Nuclear Sources of the Electricity Energy," *Energoatomizdat, Moscow* (1992).

- <sup>7</sup> A. G. Kavetsky, S. N. Nekhoroshkov, S. P. Meleshkov et al., "Radioactive materials, ionizing radiation sources, and radioluminescent light sources for nuclear batteries." In: K. Bower, Y. A. Barbanel, Y. Shreter, G. Bohnert, (Eds.), *Polymers, Phosphors, and Voltaics for Radioisotope Microbatteries*. CRC Press, 39 (2002).
- <sup>8</sup> L. F. Belovodskii, V. K. Gaenov, and V. I. Grishmanovskii, "Tritium," *Energoatomizdat*, Moskow (1985) [Russian].
- <sup>9</sup> G. D. Gorlovoi, and V. A. Stepanenko, "Tritium-Based Emitters," *Atomizdat*, Moskow (1965) [Russian].
- <sup>10</sup> J. A. Tompkins, et al., "Tritide based radioluminescent light sources," *Radioluminescent Lighting Technology. Technology Transfer Conference Processing*, DOE, Annapolis, MD (1990).
- <sup>11</sup> Ritverc. *Isotope products*. 2003-2008, url: <<http://ritverc.com/>>.
- <sup>12</sup> QSA Global. *Sources*. 2008, url: <<http://www.qsa-global.com/Sources.html>>.
- <sup>13</sup> A. Kavetsky, G. Yakubova, Q. Lin et al. "Promethium-147 Capacitor," *Applied radiation and isotopes*, **67**, 6, 1057 (2009).
- <sup>14</sup> J. Braun, L. Fermvik and A. Stenback, "Theory and Performance of a Tritium Battery for the Microwatt Range," *Journal of Physics E: Scientific Instruments*, **6**, 727 (1973).
- <sup>15</sup> L. F. Belovodskii, V. K. Gaenoi, and V. I. Grishmanovskii, "Tritium," *Energoatomizdat*, Moskow (1985).
- <sup>16</sup> L. M. Langer, J. W. Motz, H. C. Price, "Low energy beta spectra: Pm-147, S-35," *Physical review*, **77** (6), 798 (1950).
- <sup>17</sup> [http://en.wikipedia.org/wiki/Secondary\\_emission](http://en.wikipedia.org/wiki/Secondary_emission)
- <sup>18</sup> H. Seiler, "Secondary electron emission in the scanning electron microscope," *Journal Applied Physics* **54** (11), R1 (1983).
- <sup>19</sup> E. K. Malyshev, et al., "Effects of surface state on the yield of true secondary electrons from a metal bombarded by photons and fast electrons," *Atomnaya Energiya* **74** (3), 262 (1993).
- <sup>20</sup> J. C. Trump, and R.J. Van de Graaff, "The secondary Emission of Electrons by High Energy Electrons," *Physical Review* **75** (1), 44 (1949).
- <sup>21</sup> Y. C. Yong, and J.T.L. Thong, "Determination of Secondary Electron Spectra from Insulators," *Scanning* **22**, 161 (2000).
- <sup>22</sup> Y. Kishimoto, T. Ohshima, et al., "A Consideration of Secondary Electron Emission from Organic Solids," *Journal of Applied Polymer Science* **39**, 2055 (1990).
- <sup>23</sup> D. C. Joy, "A Database of Electron-Solid Interactions," <http://web.utk.edu/~srcutk/htm/interact.htm> (2008).
- <sup>24</sup> J. Cazaux, "A new model of dependence of secondary electron emission yield on primary electron energy for application to polymers," *Journal of Physics D: Applied Physics* **38**, 2433 (2005).
- <sup>25</sup> Yu. G. Malynin, "Secondary electron emission of certain ceramics and antidynatron coatinds," *Army Foreign Science and Technology Center* (1974).
- <sup>26</sup> V. Baglin, J. Bojko, et al., "The secondary electron yield of technical materials and its variation with surface treatments," *Proceedings of EPAC*, 217 (2000)
- <sup>27</sup> N. Hillbert, C. Scheuerlein, and M. Taborrelli, "The secondary-electron yield of air-exposed metal surfaces," *Applied Physics A* **76**, 1085 (2003).
- <sup>28</sup> [http://en.wikipedia.org/wiki/Scanning\\_electron\\_microscope](http://en.wikipedia.org/wiki/Scanning_electron_microscope)
- <sup>29</sup> G. Archard, "Backscattering of Electrons", *Journal of Applied Physics* **32**, 1505 (1961).

- <sup>30</sup> T. Tabata, R. Ito, and S. Okabe, “An empirical equation for the backscattering coefficient of electrons,” *Nuclear Instruments and Methods* **94**, 509 (1971).
- <sup>31</sup> J. W. Martin, J. Yuan, et al., “Measurement of electron backscattering in the energy range of neutron beta decay,” *Physical Review C* **68**, 055503 (2003).
- <sup>32</sup> S. Shionoya and W.M.Yen, Eds., “Phosphor Handbook,” *CRC Press LLC*, Boca Raton, Fl, 1999
- <sup>33</sup> E. J. Sternglass, “Backscattering of Kilovolt Electrons from Solid,” *Physical Review* **95** (2), 345 (1954).

## CHAPTER 4

### TRITIUM DIRECT CHARGE NUCLEAR BATTERY

#### 4.1 TRITIUM BETA SOURCE (MANUFACTURING AND CHARACTERISTICS)

##### 4.1.1 Characteristics of tritium beta sources

The tritium beta sources which can be used in nuclear batteries are usually thin layers of titanium or scandium on metal substrate saturated with tritium. These metal dihydrides (ditritide) are used for fixing tritium on surfaces as they are stable at room temperature and have the highest specific content of hydrogen (up to 4% by mass) or tritium (up to 11% by mass). Equation (1.1) shows that specific activity that titanium and scandium tritide can reach 1100 Ci/g. Due to self-adsorption of tritium beta particles in the tritide layer, beta flux increases with thickness (mass thickness) and then reaches saturation at thickness of 600-800 nm.<sup>1</sup> Therefore, making the tritide thicker serves no applicable purpose. The value of current density of outgoing beta particles  $dI_\beta/dS$  (nA/cm<sup>2</sup>) is the most important characteristic of the source for building the DCNB. This value can be calculated as

$$\frac{dI_\beta}{dS} = \frac{q_e}{\varepsilon_{avg}} \cdot \frac{dP_\beta}{dS} = 0.175 \cdot \frac{dP_\beta}{dS} \quad (4.1)$$

where  $dP_\beta/dS$  is the outgoing beta particle power flux surface density in  $\mu\text{W}/\text{cm}^2$ .

At saturation, the maximum possible value of  $dP_\beta/dS$  for titanium and scandium tritide is approximately 0.72-0.99  $\mu\text{W}/\text{cm}^2$ .<sup>1</sup> Thus, the calculation gives the maximum current density of outgoing beta particles as  $\frac{dI_\beta}{dS} = 0.13\text{-}0.17$  nA/cm<sup>2</sup>.

For real sources the determination of  $dI_\beta/dS$  can be done through measurement of the ionization current density  $dI_{ion}/dS$  from the source. These values are connected through the relationship

$$\frac{dI_\beta}{dS} = \frac{dI_{ion}}{dS} \cdot \frac{\varepsilon_{ion\_pair}}{\varepsilon_{avg}} \quad (4.2)$$

where  $\varepsilon_{ion\_pair}$  is the energy from producing an ion pair in air. It is approximately 34 eV.<sup>2</sup>

From this relationship the upper limit of ionization current density for tritium sources in titanium or scandium was found to be approximately 29 nA/cm<sup>2</sup>.

For calculating the battery efficiency one needs to know the activity of tritium in the source. For estimation of the activity the form of tritium (TiT<sub>2</sub> or ScT<sub>2</sub>), thickness of layer, and the efficiency of source,  $\eta_s$ , were considered. The ratio of beta particles emitted from the surface of the source to the beta particles in the source can be estimated by the next equation (see paragraph 3.2.2.3):

$$\eta_s = \frac{1}{q_e \cdot A_{sp} \cdot D} \cdot \frac{dI_\beta(A_{sp}, D)}{dS} \quad (4.3)$$

where  $A_{sp}$  is the specific activity in the layer and  $D$  is its mass thickness.

$dI_\beta/dS$  dependence on  $A_{sp}$  and  $D$  is given in Equation (3.5) and shows that  $dI_\beta/dS$  and  $A_{sp}$  are directly proportional. Therefore, the efficiency of the source depends on  $D$  only.  $\eta_s$  dependence on the thickness of the active source layer is plotted in Figure 4.1. These curves are plotted based on the above equation for  $\eta_s$  versus the thickness of the layer. The average density of titanium tritide is 3.8 g/cm<sup>3</sup><sup>3</sup> and scandium tritide is 2.9 g/cm<sup>3</sup>.<sup>4</sup> Both values were used for calculations.

The source surface specific activity,  $A_s$ , and total activity,  $A$ , can be estimated based on the efficiency of the source at the fixed layer thickness and its beta particle current density (ionization current density) or total ionization current, using the next equation:



$$A_s = \frac{1}{q_e \cdot \eta_s} \cdot \frac{dI_\beta}{dS} \quad (4.4)$$

or 
$$A_s = \frac{1}{q_e \cdot \eta_s} \cdot \frac{dI_{ion}}{dS} \cdot \frac{\varepsilon_{ion\_pair}}{\varepsilon_{avg}} \quad (4.5)$$

or 
$$A_s \left( \frac{mCi}{cm^2} \right) = \frac{1.01}{\eta_s} \cdot \frac{dI_{ion}}{dS} \quad (4.6)$$

and 
$$A(mCi) = \frac{1.01}{\eta_s} \cdot I_{ion} \quad (4.7)$$

where  $\eta_s$  is given in arbitrary units;  $dI_{ion}/dS$  and  $I_{ion}$  are given in nA/cm<sup>2</sup> and nA, respectively.

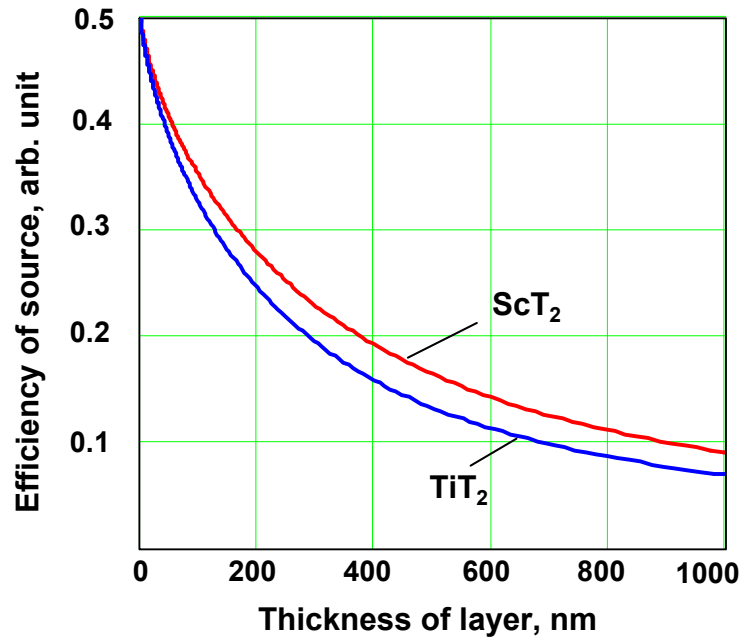


Figure 4.1. Efficiency of tritium beta sources with thickness of active layer

From the data on thickness of the tritide layer one can define the efficiency of the source using Figure 4.1. Then the ionizing current was measured and the surface specific activity or activity of the source was calculated using Equation (4.6) or (4.7).

#### 4.1.2 Manufacturing and determination the activity of sources

##### 4.1.2.1. Manufacturing of sources

Tritium sources are usually the  $\text{ScT}_2$  or  $\text{TiT}_2$  layers on a metal substrate.

One of the manufacturing technologies is described by B. Liu and K. P. Chen.<sup>5</sup> The source is manufactured in two stages. At the first stage, a thin layer (around 300 nm) of Sc or Ti is evaporated on a metal substrate. Then this layer is saturated by tritium. The saturation with tritium is carried out in a closed vacuum loading system. The main parts of the system are a temperature-controlled uranium tritide storage bed (activity of tritium is  $10^3$ - $10^4$  Ci), an intermediate tritium transfer chamber, and the sample exposure chamber. The process begins by transferring the tritium from the uranium storage bed to the cryogenically cooled (77K) transfer chamber at one atmosphere. Next, the temperature of the transfer and exposure chambers were raised to room temperature to release all tritium, and then heated to 250°C to create pressure in the chambers of about 12 MPa. Under these conditions, the sample is held for 7 days. After that, the temperature of the system was reduced and the remaining tritium is absorbed back onto the uranium bed. Using this technology, PitU-100 and PitU-50 type sources (see Table 4.1) were prepared by Professor K. P. Chen et al. (Pittsburg University) for this research.

Also the tritium-titanium sources on molybdenum substrate (BITR type, see Figure 4.2a) were used. The main features involved in making these sources were the temperature at saturation (350-400°C), pressure (50-100 Torr), and time of saturation (2 hours).

Pictures of the different types of sources used in the present research are shown in Figure 4.2a, b.

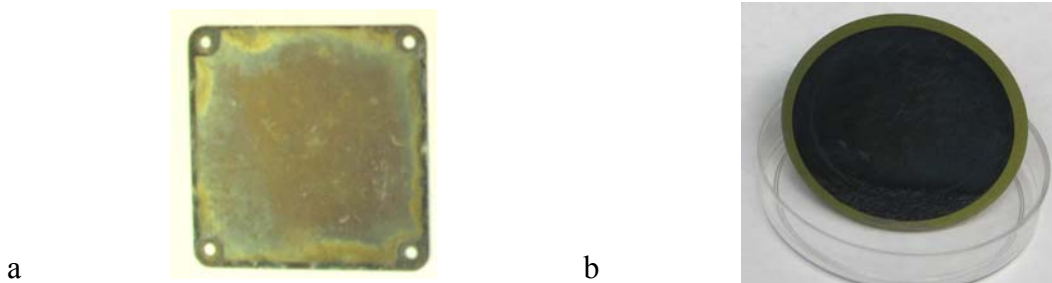


Figure 4.2. The view of BITR type (a) and PitU-100 and PitU-50 types (b) tritium sources

#### 4.1.2.2. Determination of the activity of sources

The activity of the sources can be determined from ionization current.

The setup shown in Figure 4.3 was used for measuring the ionization current ( $I_{ion}$ ). The setup has two metal electrodes with a diameter of 76 mm at a distance of 28 mm (or 120 mm for source diameter of 100 mm) between them. This is more than the maximum 6 mm range of tritium beta particles.<sup>6</sup> A Keithley Power Supply K248 and Keithley Electrometer K6514 were used to measure the ionizing current. The tritium source was placed on one of the electrodes, and an increasing potential difference between the electrodes was applied.

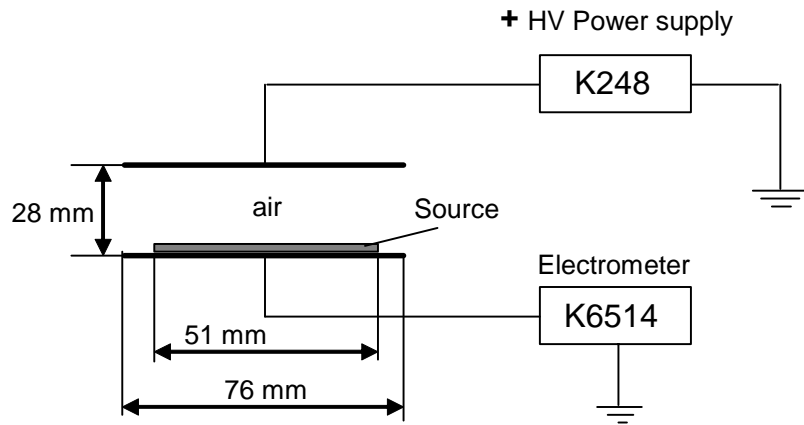


Figure 4.3. Experimental setup to measure ionization current of tritium sources

Some examples of the dependencies of ionization current with applied voltage for the PitU-50 type of tritium sources on stainless steel (curve 1) and aluminum (curve 2) are shown in Figure 4.4. Current increases with rising voltage and reaches saturation when all ionizing particles are collected on the electrodes.

The characteristics of sources used in the present research, measured values of ionization current, values of beta particle current and source activity calculated by Equations (4.2) and (4.7), respectively, are shown in Table 4.1.

**Table 4.1. Characteristics of tritium sources**

Source type	Size, mm	Substrate material	Radioactive layer material	$dI_{ion}/dS,^*$ nA/cm <sup>2</sup>	$dI_{\beta}/dS,^*$ pA/cm <sup>2</sup>	Surface activity, mCi/cm <sup>2</sup>	Total activity, mCi
BITR	40x40	Mo	Ti	4.4	26	26	420
PitU-100	Dia100 x 0.25	SS**	Sc	13	78	57	4500
PitU-50	Dia50 x 0.25	SS	Sc	12	72	53	1040
	Dia50 x 0.8	Al	Sc	9.7	58	43	840

\* Average value for particular type of source

\*\* Stainless Steel

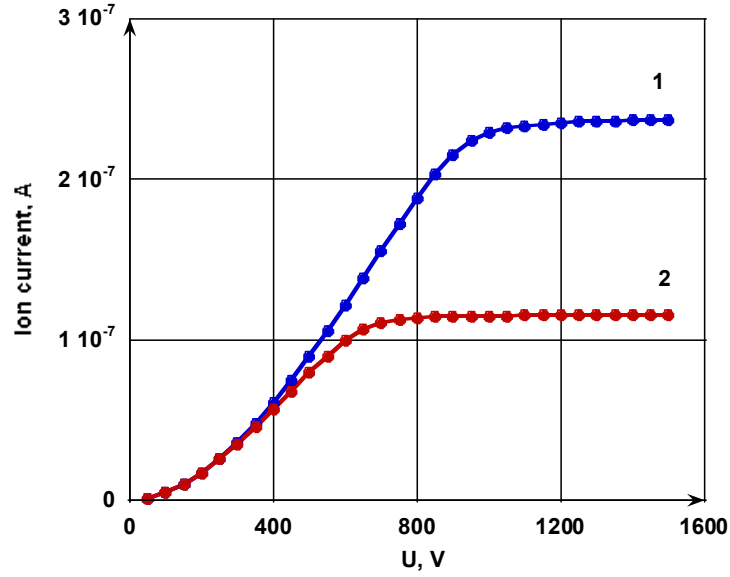


Figure 4.4. Dependency of ionizing current with applied voltage of tritium source type PitU-50 on stainless steel (1) and aluminum substrate (2)

#### 4.2 EXPERIMENTAL SETUP FOR TESTING TRITIUM DIRECT CHARGE NUCLEAR BATTERY

Two types of experimental setups were used in this research. The main distinctions in setup were the different ways of measuring the tritium nuclear battery characteristics.

The tritium direct charge experimental setup is shown on Figure 4.5 with the vacuum chamber, electrical feed-through, and measurement devices. The vacuum chamber has two ports for connection to a low vacuum line (mechanical pump) and a high vacuum line (turbo molecular pump). The pressure in the vacuum chamber was pumped below  $10^{-5}$  Torr. A convectron gauge and ion gauge were used for the measurement of residual pressure in the chamber. For measurement of the charging current, the Keithley 6514 Electrometer was used. A Monroe Electronics 257F electrostatic field meter with probe 1036F was used for measurement of the accumulated voltage. A 2 cm thick cover for the vacuum chamber was made from Teflon. On the inner side of the cover was a metal gradient plate for the

electrostatic field meter. On the external side of the cover the probe with ground plate was positioned.

For tritium direct charge experiments, the experimental setup was placed in the fume hood to ensure the safe handling of tritium sources.

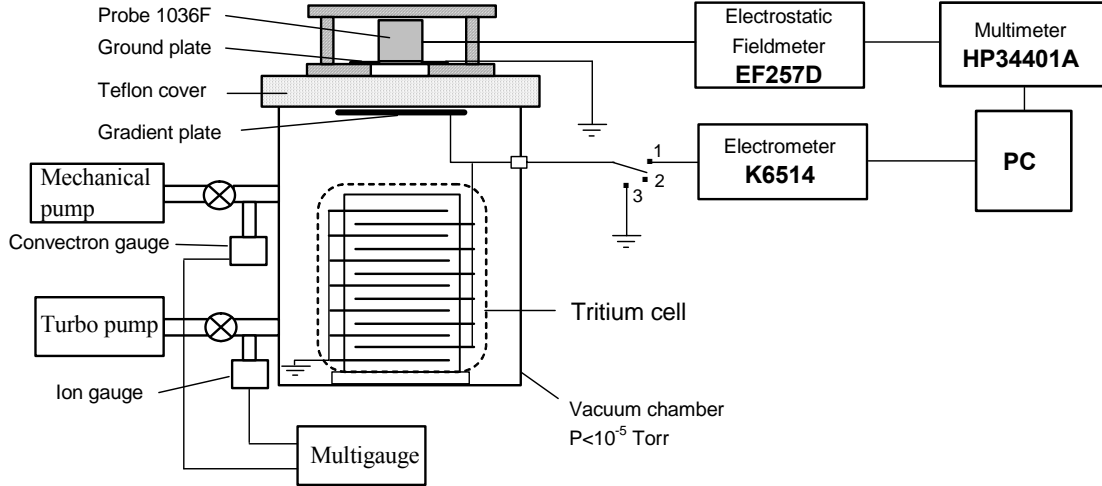


Figure 4.5. The tritium direct charge experimental setup #1

Before carrying out experiments, calibration of the noncontact high voltage measure system based on the electrostatic field meter using a high voltage power supply (Keithley 248 connected instead of Electrometer K6514, without tritium cell) was performed. The calibration curve is shown in Figure 4.6. As shown, this dependence is linear through the origin. The calibration relation determined for the high accumulated voltage value was

$$U_{collector} = 9490 \cdot U_{meas}.$$

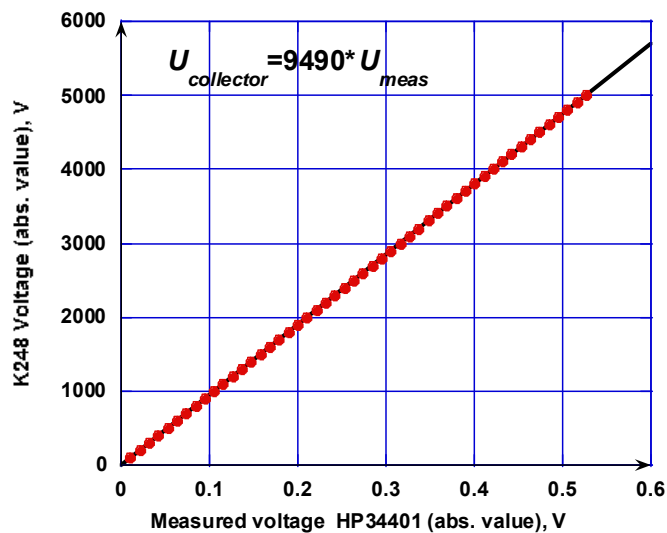


Figure 4.6. Calibrated Fieldmeter EF257D with Teflon Covered Vacuum Chamber

The setup shown in Figure 4.7 was used for the determination of the optimal electrode distance spacing (see part 4.3.1). The accumulated voltage was measured directly by an electrostatic voltmeter.

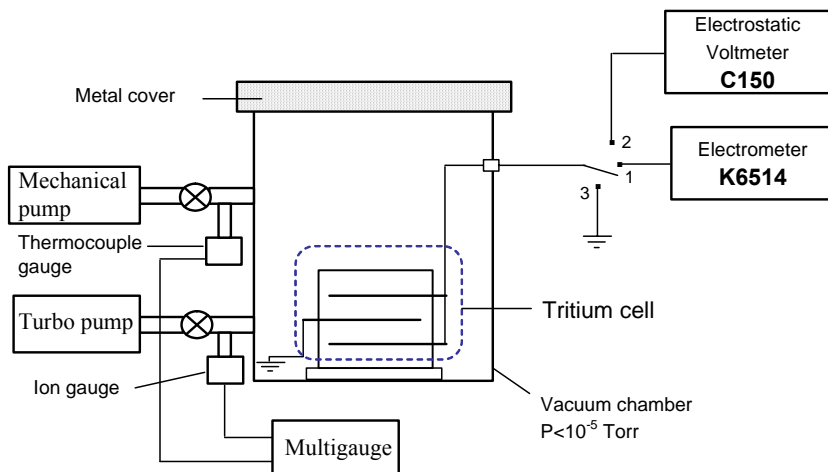


Figure 4.7. The tritium direct charge experimental setup #2

## 4.3 DESIGN OF TRITIUM DIRECT CHARGE NUCLEAR BATTERY

### 4.3.1 Interelectrode distance

To determine optimum electrode spacing in the multi-layer direct charge nuclear cells with a vacuum dielectric experimental battery model, two tritium sources and two collectors were used. Two tritium beta sources, BTR type, were put together back-to-back and two aluminum collectors were used in this model. The distance between the source and the collector were varied using small plastic spacers. The battery model for measurement was set into the vacuum chamber with a residual pressure  $< 10^{-4}$  Torr. Accumulated voltage at open circuit was measured using an electrostatic voltmeter and short current was measured to picoampere resolution using an electrometer.

Accumulated voltages with time for different interelectrode distance are represented in Figure 4.8 by points.

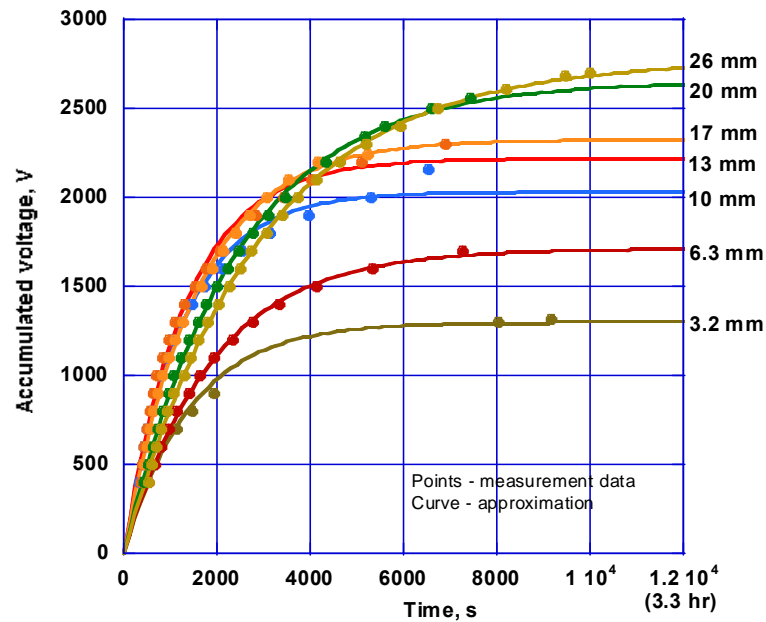


Figure 4.8. Accumulated voltage with time for battery model with two tritium sources and two collectors at different interelectrode distances



Experimentally measured changes in short circuit current and saturation voltages for different interelectrode distances are plotted in Figure 4.9 by points.

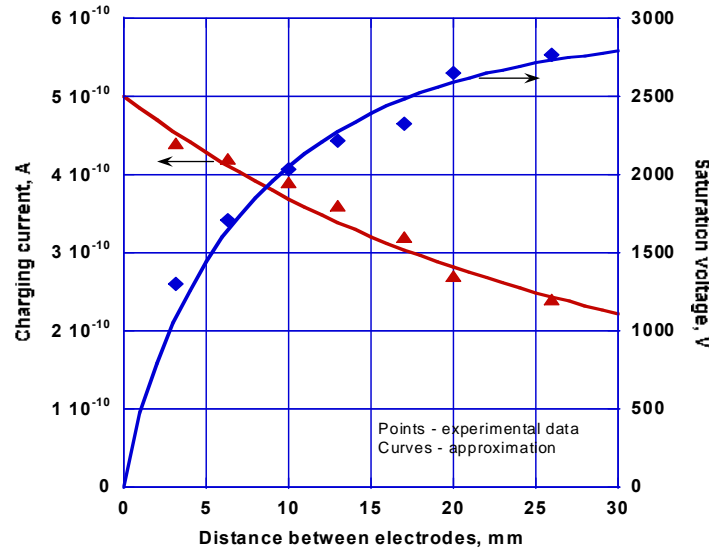


Figure 4.9. Short circuit current and voltage at saturation for different interelectrode distance for battery model consist from two tritium sources and two collectors

Short circuit current decreases with increasing electrode spacing as shown in Figure 4.9. This is probably due to the loss of beta particles to the side. The dependence of beta particle current reaching the collector in the parallel plane model of the direct charge battery with dimensions of the electrodes and their spacing is represented in part 3.2.2.1, Equation (3.14). In these experiments with different interelectrode distances,  $d$ , the radii of the electrodes were each 2 cm. A calculation using Equation (3.14) was used for approximation of the short circuit current with the electrode spacing as plotted in Figure 4.9. It compares well to the experimental data and is evidence of the workability described in part 3.2.2.1 model and calculations. The approximation equation for  $I_{Ch}=I_{sc}$  in ampere with  $d$  in millimeters is

$$I_{Ch} = 0.5 \cdot 10^{-9} \cdot k_g(0.02, d/1000) \quad (4.8)$$

where  $k_g(0.02, d/1000)$  is the fraction of beta particle flux that reaches the collector, (geometrical factor) versus  $d$  calculated by Equation (3.14).

Approximated accumulated voltage with time as represented in Figure 4.9 was made by solving Equation (3.39), which accounts for the decreasing charging current with voltage. The charging current calculated using Equation (4.8) was used for each interelectrode distance. The leakage resistivity was calculated by equation

$$R_{leak} = \frac{U_{sat}}{I_{Ch} \cdot \eta_R(U_{sat})} \quad (4.9)$$

where  $\eta_R(U_{sat})$  is the fraction of beta flux reaching the collector using  $U_{sat}$ , calculated from Equation (3.20).

Calculated  $R_{leak}$  with interelectrode distance is plotted in Figure 4.10 and represented by points. This dependence  $R_{leak}$  in Ohm versus interelectrode distance in millimeters can be approximated with suitable accuracy by the equation below.

$$R_{leak} = 1.025 \cdot 10^{12} \cdot d^{0.83} \quad (4.10)$$

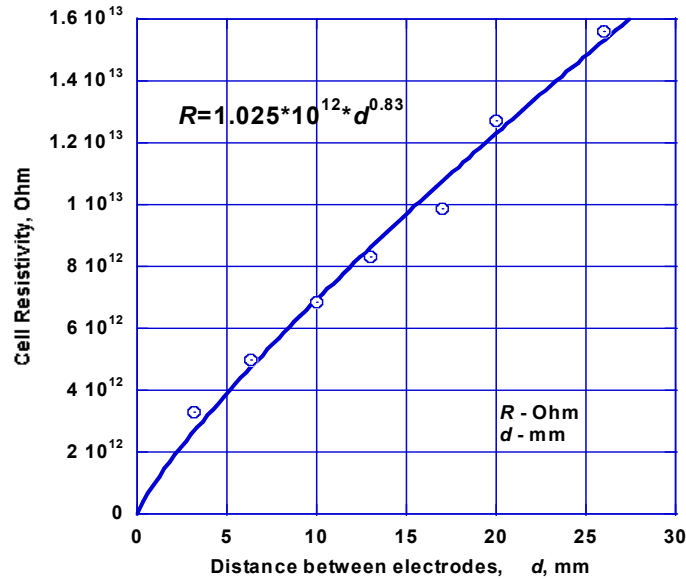


Figure 4.10. Dependence calculated  $R_{leak}$  with interelectrode distance for battery model consist from two tritium sources and two collectors

In order to optimize interelectrode distance, the dependence of useful electrical power versus interelectrode distance was plotted in Figure 4.11. On this plot the product of experimentally measured short circuit current and open circuit voltage at saturation is represented as points. The curve on this plot is the product of short circuit current calculated using Equation (4.8) and saturation voltage calculated from equation:

$$U_{sat} = R_{leak} \cdot I_{Ch} \cdot \eta_R(U_{sat}) \quad (4.11)$$

The numerical solution of Equation (4.11) used Equations (4.8) and (4.10). In both cases, the useful electrical power factor of 0.25 (see Equation (2.10)) was applied. The useful electrical power is maximized by an interelectrode distance of 12 mm, as shown from this plot.

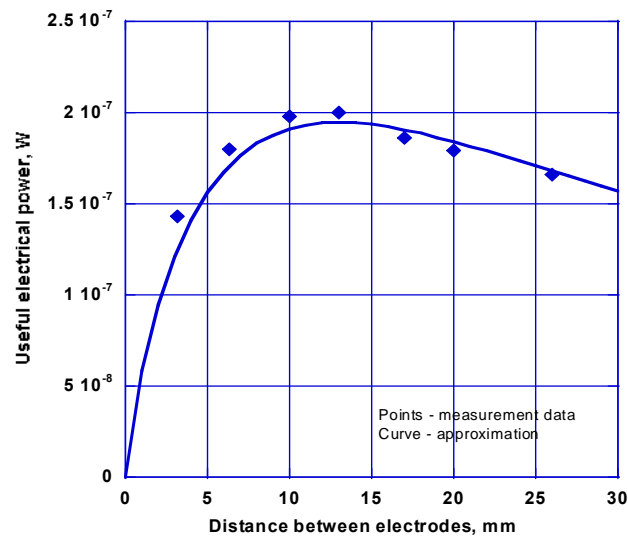


Figure 4.11. Useful electrical power with interelectrode distance for battery model with two tritium sources and two collectors

The optimal interelectrode distance at the building the DCNB with the 24 round PitU-100 type tritium sources available for this research were chosen using the method described below. A battery consisting of 24 round sources each having a 10 cm diameter (see part 4.1) and an electrode with a separation of 5 mm were built. For this battery, short circuit current was 148 nA and open circuit voltage at saturation was 5300 V. Assuming that the rules

described for the case of a battery with two sources is correct for multiple sources, namely, the short circuit current with interelectrode distance as described by an equation similar Equation (4.8), leakage resistance is proportional to interelectrode distance in power 0.83 (Equation (4.10)), and open circuit voltage is described by Equation (4.11), then it is possible to write:

$$I_{ch}(d) = \frac{148 \cdot 10^{-9}}{k_g(0.05, 0.005)} \cdot \eta_R(0.05, d/1000) = 158 \cdot 10^{-9} \cdot k_g(0.05, d/1000) \quad (4.12)$$

$$R_{leak}(d) = \frac{5300}{148 \cdot 10^{-9} \cdot \eta_R(5300) \cdot 5^{0.83}} \cdot d^{0.83} = 1.96 \cdot 10^{10} \cdot d^{0.83} \quad (4.13)$$

Useful electrical power is the product of  $I_{ch}$  and  $U_{sat}$ . For a battery with 24 sources against electrode separation, distance was calculated according to Equations (4.12) and (4.13) using MathCad and plotted in the Figure 4.12. A factor of 0.25 was assumed. As can be seen from this plot, the optimum electrode separation distance for this case was around 20 mm. Maximum power occurs at 20 mm and at 5 mm a difference of 17% is shown. At the same time, the total volume of the battery, with the tighter spacing, will 4 times smaller. Therefore, the battery with 5 mm spacing was built as a working model of tritium DCNB.

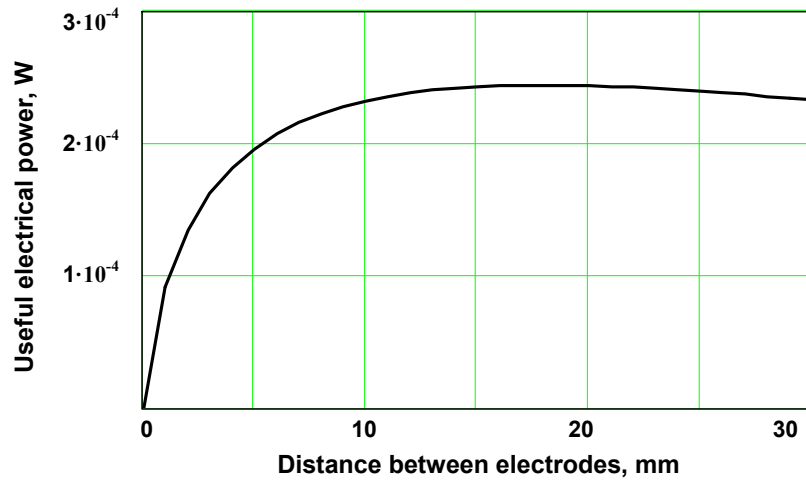


Figure 4.12. Useful electrical power against electrode spacing for battery models using 24 tritium sources

#### 4.3.2 Collector material and coverage

As described in Chapter 3, the material of the collector is critical for building the DCNB due to the secondary electron emission yield and backscattering dependence on particular materials. For this investigation the measurements of charging current (short circuit current) of a beta cell with one tritium source and one collector was made. The results of the measurements are shown in Table 4.2. As can be seen from the Table, the aluminum collector is more promising.

**Table 4.2. Charging current of beta cell for different collector material**

Collector material	Stainless steel	Al	Cu	Ni
Charging current, pA	440	923	743	585

Investigation of the effect of collector roughness on the charging current was made by sanding stainless steel and aluminum collectors to different roughness levels,  $R_a$ . The results of the measurements are shown in Table 4.3. Stainless steel collectors show charging current increasing with increasing roughness to saturation. For aluminum collectors, the charging current is practically the same across different level of roughness.

**Table 4.3. Charging current (pA) of beta cell for different collector roughness**

Roughness, $R_a$ , $\mu\text{m}$	Stainless steel	Al
0	440	923
0.15	650	1056
0.33	740	1100
0.5	738	1018
1.5	718	969
3.3	734	1028

Measurements of open circuit accumulated voltage show only -4 V. Even a very small negative potential on the collector is enough to repel all secondary electrons under the conditions of an uncoated collector.

Investigations of collector coatings for the purpose of suppressing secondary electrons and backscattering were done. At first, the aluminum collector was covered with graphite by hand. Charging current was measured to be 915 pA and the cell accumulated 16 V.

The previous literature research (see Chapter 3) showed that polyimide can be a good collector coating. At this stage of work, the stainless steel collector was coated with 1  $\mu\text{m}$  of polyimide. All the described work of collector coating was done by Dr. S. Yousaf, chemist, TRACE Photonics, Inc. Measured short circuit current was 670 pA, but voltage was accumulated to 310 V (compare with 16 V received early). Given these results, further study in this direction was pursued.

Next, investigations were done with round tritium sources measuring 10 cm diameter. The stainless steel collectors (with a diameter of 10 cm) with various polyimide (PI) coating thicknesses were prepared. The charging current versus polyimide layer thickness was measured with Setup # 1. In this experiment, one tritium source type PitU-100 and different collectors with different thickness of the PI layer were used. The distance between the source and collector was 5 mm. Data is shown in Figure 4.13.

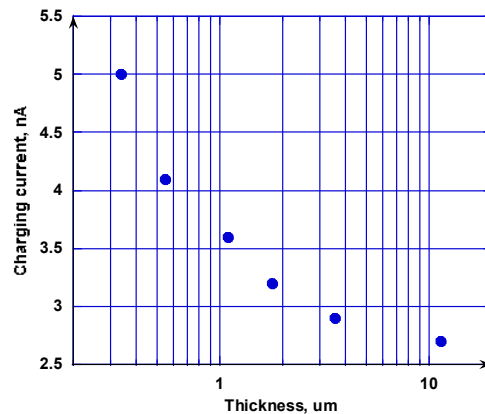


Figure 4.13. Charging current vs thickness of the polyimide layer. The charging current with a clean stainless steel collector (without polyimide coating) was 2.4 nA

When the charging current value with clean stainless steel collectors (without polyimide coating) of 2.4 nA is taken into account, a layer less 0.3  $\mu\text{m}$  for secondary electron suppression may be optimal. Collectors with 0.3  $\mu\text{m}$  polyimide coating are best for tritium DCNB with multiple tritium source DCNB.

#### 4.3.3 Multilayer tritium DCNB

For testing the tritium direct charge multilayer nuclear battery, scandium tritide sources type PitU-100 fabricated by the University of Pittsburg were used. The activity of the tritium in each source was approximately  $1.7 \cdot 10^{11}$  Bq (4.5 Ci). These sources were stainless steel disks (diameter of 10 cm and thickness 0.5 mm). One side of each disk was coated with 300 nm of scandium and then saturated with tritium gas. Collectors are the same size and material of construction as sources. However, the collectors also had a thin polyimide coverage (0.3-0.4  $\mu\text{m}$ ) on both sides. This polyimide coverage suppressed secondary electrons and backscatter. The battery has unit cells of collectors and back-to-back sources. Sources and collectors were fixed in holder slots. The distance between source and collector was 5 mm using 24 sources for total activity of  $4.0 \cdot 10^{12}$  Bq (108 Ci)). Sources were connected in parallel and grounded. Collectors were connected in parallel and also to a gradient plate for measuring the accumulated voltage by a fieldmeter. Electrical feedthroughs were used to measure the charging current (see Figure 4.5). The general view of the battery is shown in Figure 4.14.

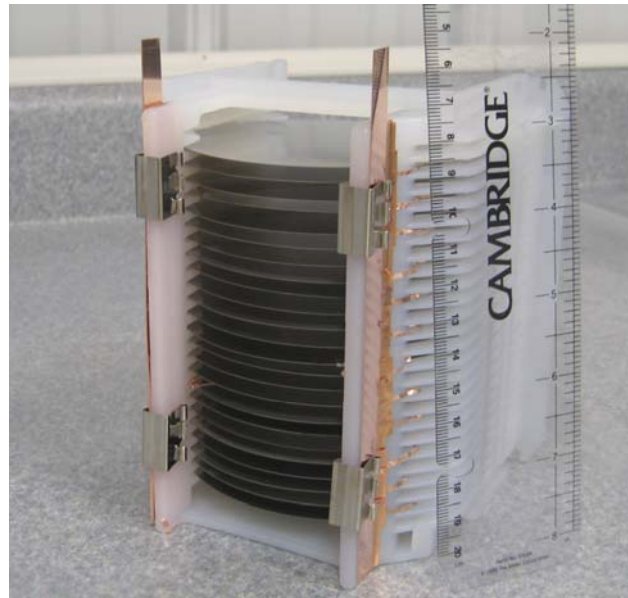


Figure 4.14. Overview of the tritium battery with 24 tritium sources (total  $4.0 \cdot 10^{12}$  Bq (108 Ci)) and 13 ss-collectors with polyimide coating. Distance between each source and collector is 5 mm

#### 4.4 TESTING RESULTS OF MULTILAYER TRITIUM DIRECT CHARGE NUCLEAR BATTERY, EFFICIENCY OF TRITIUM DIRECT CHARGE NUCLEAR BATTERY

The purposes of the experiments were to define the characteristics of this tritium DCNB: charging current, process of voltage accumulation, and level of saturation and efficiency of the battery. The experimental data was compared to the theoretical description of the charging process.

The experiments were done on setup #1. Results of experiments with DC tritium battery described above are shown by points in Figure 4.15. As can be seen from this plot, the voltage on the tritium DCNB reached saturation at 5300V in 10 min where it was then stable for at least 20 minutes. The charging current (short circuit current  $I_{sc}$ ) was approximately 148 nA.

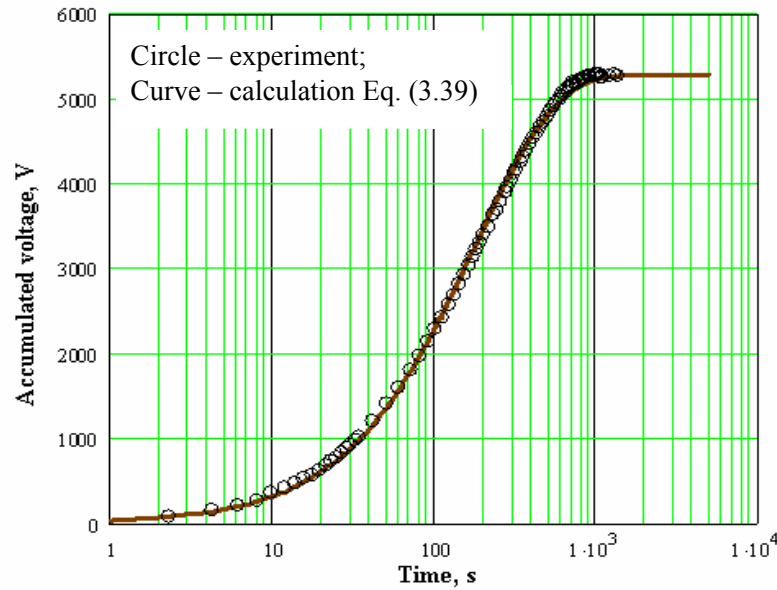


Figure 4.15. Accumulated voltage of the tritium direct charge nuclear battery with time. Circles are experimental results. The curve is the solution to Equation (3.39).

$$R_{leak}=R_{cell}=75 \text{ GOhm}, C=5 \text{ nF}$$



The numerical solution of Equation (3.39) takes into account the increasing repulsion of beta particles by the building potential on the collector, as illustrated by the curve in Figure 4.15. The fit leakage resistance ( $R_{leak}=R_{cell}$  at open circuit) and capacitance were 75 GOhm and 5 nF, respectively. The measured capacitance was 3 nF. There were strong similarities between the experiment and calculation data.

From these results it is possible to determine the maximum power of this nuclear battery as well as voltage and current at the highest electrical power.

The saturation voltage which takes into account electrostatic repulsion can be calculated by

$$U_{sat} = I_{sc} \cdot R_{leak} \cdot \eta_R(U_{sat}) \quad (4.14)$$

where  $R_{leak} = \frac{R_{cell} \cdot R_{load}}{R_{cell} + R_{load}}$  (Equation (2.7))

Then from Equation (2.7)

$$R_{load} = \frac{R_{cell} \cdot R_{leak}}{R_{cell} - R_{leak}} \quad (4.15)$$

Using Equations (4.14) and (4.15) we can calculate  $I_{load}$  as

$$I_{load} = \frac{U_{sat}}{R_{load}} = I_{sc} \cdot \left[ \eta_R(U_{sat}) - \frac{U_{sat}}{U_{oc}} \cdot \eta_R(U_{oc}) \right] \quad (4.16)$$

$U_{sat}$  and  $I_{load}$  are functions of  $R_{load}$ . Figure 4.16 shows these dependencies as calculated by MathCad.

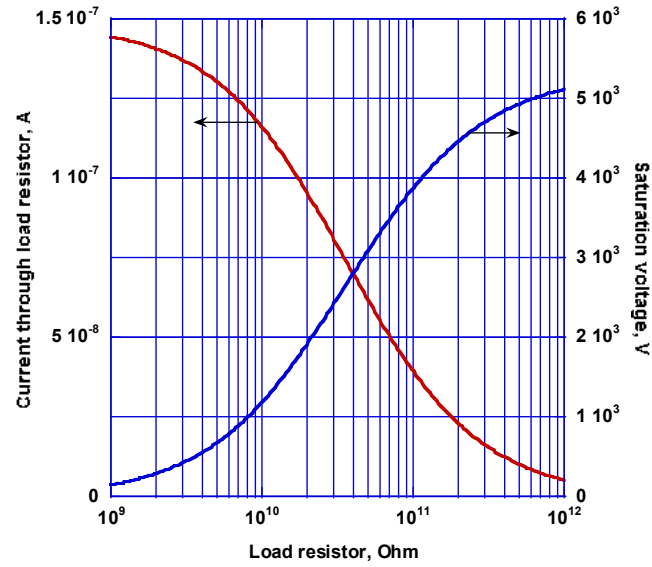


Figure 4.16. Saturation voltage and current through load resistor vs. load resistor

The plot of electrical power on load calculated as a product of  $U_{sat}$  and  $I_{load}$  versus load resistor is shown in Figure 4.17. At  $R_{load}=35$  GOhm, there is a maximum of approximately 200  $\mu$ W.

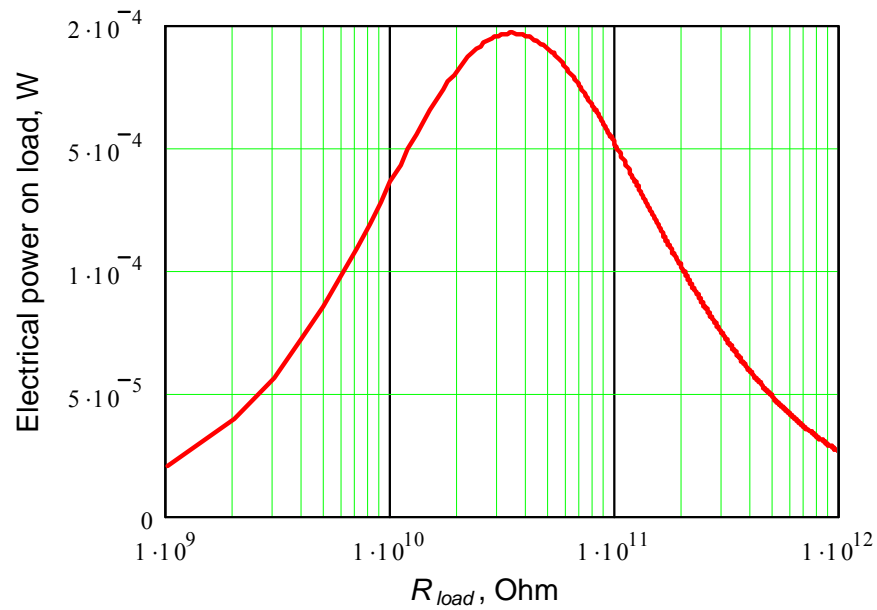


Figure 4.17. Output electrical power on load vs. load resistor

To calculate the overall efficiency of the DCNB one needs to know the activity of the sources. This value can be calculated using Equation (4.7), the measured value of short circuit current at 148 nA, and the efficiency of these 300 nm thick ScT<sub>2</sub> layers from the plot in Figure 4.1, which is 0.23.

$$A = \frac{1.01}{\eta_S} \cdot I_{ion} = \frac{1.01}{\eta_S} \cdot I_{\beta} \cdot \frac{\varepsilon_{avg}}{\varepsilon_{ion\_pair}} = \frac{1.01}{0.23} \cdot 148 \cdot \frac{5700}{34} = 108 \text{ Ci} \quad (4.17)$$

The efficiency of tritium direct charge nuclear battery can be calculated by Equation (2.12).

$$\xi = \frac{P_{el,max}}{P_{RD}} \cdot 100\% = \frac{P_{el,max}}{A \cdot \varepsilon_{avg}} \cdot 100\% = \frac{200 \cdot 10^{-6}}{108 \cdot 3.7 \cdot 10^{10} \cdot 5.7 \cdot 1.6 \cdot 10^{-16}} \cdot 100\% = 5.5\%$$

Taking into account that this battery was not at optimal electrode separation distance, which reduced the output power 17%, and that  $2\pi$  sources were used in this battery, one can calculate the overall efficiency of a tritium direct charge nuclear battery for  $4\pi$  geometry and at optimal interelectrode distance:

$$\xi = 5.5\% \cdot 1.17 \cdot 2 = 12.6\%$$

In this case, the overall efficiency will be equal to the theoretical efficiency calculated by Equation (3.41).

As shown in Figure 4.16, the maximum electrical power for this battery will occur at 2600 V output voltage. As a result, the working stability of the tritium battery was examined. For this purpose the battery with 15 tritium sources and a similar geometry was built. The charging process saturated at 2500 V and was stable over 25 hours (see Figure 4.18).

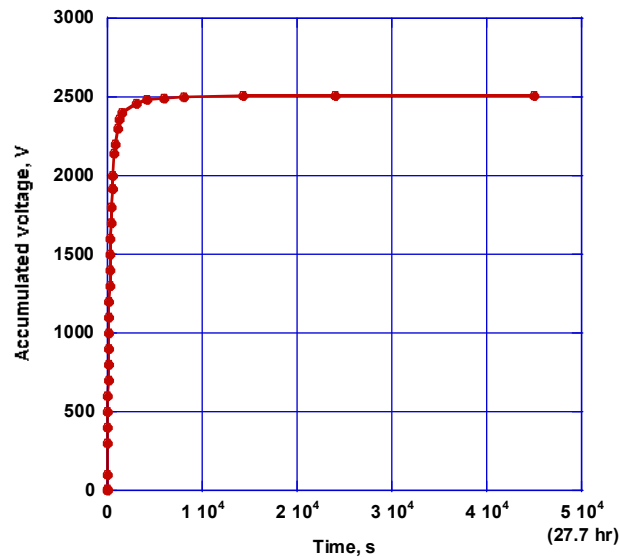


Figure 4.18. Dependency of the saturation accumulated voltage with time

As a result of the design and testing of the tritium direct charge nuclear battery it can be said:

- an overall efficiency of 5.5% in the tritium DCNB was achieved;
- at optimum electrode separation distance and with  $4\pi$  sources, the efficiency of tritium DCNB would be 12.6% (very close to upper theoretical estimation);
- reducing the thickness of the  $\text{ScT}_2$  layer gives increasing overall efficiency but decreasing output power, and vice versa.

Hence, it was demonstrated experimentally that the efficiency of the tritium direct charge battery with vacuum dielectrics, collectors with secondary electron emission suppression and backscattering coating, and  $4\pi$  tritium source can be close to theoretical limit.

## REFERENCES

- <sup>1</sup> A. G. Kavetsky, S. N. Nekhoroshkov, S. P. Meleshkov et al., "Radioactive materials, ionizing radiation sources, and radioluminescent light sources for nuclear batteries." In: K. Bower, Y. A. Barbanel, Y. Shreter, G. Bohnert, (Eds.), *Polymers, Phosphors, and Voltaics for Radioisotope Microbatteries*. CRC Press, 39 (2002).
- <sup>2</sup> G. F. Knoll, *Radiation Detection and Measurement*, 3<sup>rd</sup> ed., John Wiley & Sons (2000).
- <sup>3</sup> L. F. Belovodskii, V. K. Gaenov, and V. I. Grishmanovskii, "Tritium," *Energoatomizdat*, Moskow (1985).
- <sup>4</sup> J. C. McGuire, and C. P. Kempter, "Preparation and Properties of Scandium Dihydride," *Journal of Chemical Physics* **33**, 1584 (1960).
- <sup>5</sup> B. Liu, and K. P. Chen, "Tritium locked in silica using 248 nm KrF laser irradiation," *Applied Physics Letters* **88**, 134101 (2006).
- <sup>6</sup> "Tritium Handling and Safe Storage", *DOE-HDBK-1129-2007*, A3 (2007).

## CHAPTER 5

### PROMETHIUM-147 DIRECT CHARGE NUCLEAR BATTERY<sup>2</sup>

#### 5.1. PROMETHIUM-147 BETA SOURCE (FABRICATION AND CHARACTERISTICS)

##### 5.1.1 Background for Pm-147 source design

In Chapters 2 and 3, Pm-147 and tritium were chosen for design and testing of direct charge nuclear battery efficiency. In comparison with tritium, Pm-147 has a higher energy distribution of beta particles ( $\varepsilon_{avg}=62$  keV,  $\varepsilon_{max}=225$  keV), but a shorter half-life (2.62 years).<sup>1</sup> The thermal power of this isotope is 367  $\mu$ W per curie. The beta spectrum of Pm-147 is represented in Figure 3.8a. The mass absorption coefficient for Pm-147 beta particles is 0.19 cm<sup>2</sup>/mg. This value is known both from reference<sup>2</sup> and from measurement of beta particle penetration through aluminum foils (see Figure 5.1).

Pm<sub>2</sub>O<sub>3</sub> is the most common form of promethium. This oxide with isotope Pm-147 is available now as a fine powder in quantities of hundreds of milligrams. This amount is sufficient for producing sources with an area of 10-20 cm<sup>2</sup> and an activity of several curies. Using Equation (3.6), the specific activity of <sup>147</sup>Pm<sub>2</sub>O<sub>3</sub> can reach 800 Ci/g. Generally, enrichment of this product is less than 100% and practical specific activity is not more than 500 Ci/g.

The beta particle current density for a Pm-147 compound layer with a specific activity of 400 Ci/g was calculated in 3.2.2.1. This value of 4-5 nA/cm<sup>2</sup> is significantly more than from a tritium compound layer of 0.15 nA/cm<sup>2</sup>. The high beta particle current which gives high charging current is very important for the direct charge battery design. Furthermore, secondary electrons generated from promethium beta particles ( $\varepsilon_{avg}=62$  keV) are much less than from tritium (see part 3.2.5.). So, the secondary electron emission problem in the case of promethium battery is basically nonexistent. The problem of

---

<sup>2</sup> In this Chapter the material from: A. Kavetsky, G. Yakubova et al., "Prometium-147 Capacitor," *Applied Radiation and Isotopes* **67**, 321 (2008) is included. Copyright 2009 by Elsevier. Permission to reprint at February 9, 2010.

backscattering electrons, however, remains significant. For clear metal surfaces the value of the backscattering coefficient is more than 0.1, but can be reduced to 0.03 by applying the polyimide coating, as in the case of tritium batteries (see Figure 3.17).

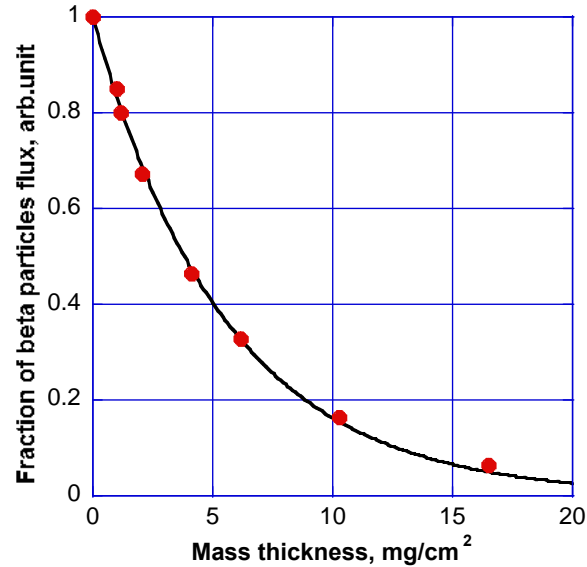


Figure 5.1. Beta particle flux fraction penetrating aluminum foil versus mass thickness of foil. Points are experimental while the curve is approximated by  $\exp(-\nu \cdot D)$ , where  $D$  is the mass thickness, and  $\nu=0.19 \text{ cm}^2/\text{mg}$  is the mass absorption coefficient for Pm-147

To build an efficient promethium-147 source for beta irradiation, the mass thickness of the promethium compound layer should not be more than  $2 \text{ mg/cm}^2$ . In this case, the efficiency of a one-sided source can be 30-35% (see Figure 3.2) and the final efficiency of the promethium direct charge battery with a double-sided source can approach its upper theoretical limit (see part 3.3). The promethium compound can be deposited between two thin aluminum films which serve as an enclosure. As illustrated in Figure 5.1, approximately 80% of the promethium beta particles penetrate a layer with mass thickness of  $1 \text{ mg/cm}^2$ . Aluminum films with thicknesses near 4 microns are near this value. The mechanical strength of two aluminum foils with thicknesses of 4 microns each is enough to ensure safe

handling. In this case, the source emits beta particles from both sides ( $4\pi$ -source), which is ideal for our purposes.

Using Pm-147 in a direct charge nuclear battery is very attractive. The design of a high efficiency Pm-147 source is ideal due to the contained thin promethium layer with mass thickness of  $1\text{-}2\text{ mg/cm}^2$  deposited between two aluminum films.

#### 5.1.2. Pm-147 beta sources

The Pm-147 sources described above were fabricated at the Missouri University Research Reactor (MURR) using technology developed by Dr. S. Yousaf at TRACE Photonics, Inc. Promethium oxide mixed with silica-titana sol-gel was spread on aluminum foil 6 or 8 microns thick. Silica-titana sol-gel can be loaded with high masses of salts or oxides. Use of the sol-gel yields a high specific activity source that strongly adheres to the substrate. Before complete curing of the sol-gel film, a second foil of aluminum or titanium (1-2 micron) is placed over the film to seal the glass precursor into the conductive source. The sol-gel binder, once cured, forms a glass matrix which serves as primary containment for the radioactive material, while the aluminum serves as a secondary containment. These sources were mounted in round or rectangular metal frames. Overviews of the different types of fabricated promethium sources are shown in Figure 5.2 and a profile of a source is shown in Figure 5.3.



a) Rectangular source



b) round source

Figure 5.2. Overview of Pm-147 sources



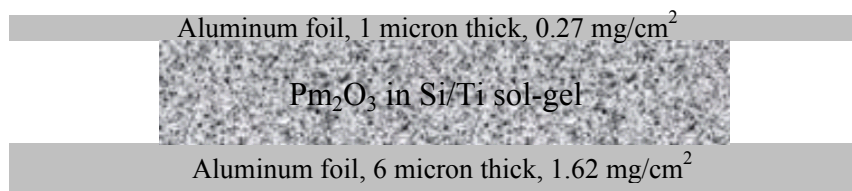


Figure 5.3. Profile of the double-sided Pm-147 source

Table 5.1 summarizes the activity of the sources on date of fabrication, the active area of the sources, the mass thickness of the active layer in  $\text{mg}/\text{cm}^2$ , the specific activity of the layer in  $\text{Ci}/\text{mg}$ , and the measured current beta particles from the sources in  $\text{nA}$ .

Promethium-147 oxide with a specific activity of  $10.7 \text{ GBq}/\text{mg}$  ( $0.29 \text{ Ci}/\text{mg}$ ) was available for preparing sources. The specific activity of the substance was determined by dissolving a weighed quantity of the sample in acid and counting the activity of a small known amount of that solution using liquid scintillation. The promethium-147 oxide had specific activity approximately 2.7 times less than theoretically possible for pure promethium-147 oxide. This was due presumably to its production age and carrier quantity.

The activity of the source was determined both by weighing the promethium-147 oxide used in preparing the sources and by direct gamma spectrometry. The gamma line of Pm-147 with energy  $121 \text{ keV}$  has a yield  $0.0000285^1$  and can be quantified accurately. Both methods gave results within 10% of each other. The detailed procedure for activity measurements is given in Appendix A.

The mass thickness of the radioactive layers was calculated from values of the weight and area of the layer's surface. The specific activities were calculated from the determined source activity and the weight of the layer.

On the basis of the data for the mass thickness of the promethium compound layer, the efficiency of sources,  $\eta_s$ , could be calculated and is also represented in Table 5.1. The efficiency calculations using Equation (3.7) takes into account the adsorption of beta particles in substrate and protective sheet.

$$\eta_s = \frac{1}{q_e \cdot A_{sp} \cdot D} \cdot \frac{dI_\beta(A_{sp}, D)}{dS} \cdot [\exp(-\nu \cdot D_{sub}) + \exp(-\nu \cdot D_{prot})] \quad (5.1)$$

where  $D_{sub}$  is the mass thickness of the substrate in  $\text{mg}/\text{cm}^2$  and  $D_{prot}$  is the mass thickness of the cover sheet in  $\text{mg}/\text{cm}^2$ .

For experimental determination of source efficiency, the beta particle current from the sources was measured. Beta particle current was measured in both the parallel plane design of the battery and in the cylindrical design. These measurement results are also given in Table 5.1. For each design, the geometrical factor was calculated using Equation (3.14) for the parallel plane geometry and Equation (3.18) for cylindrical geometry. Taking into account these geometrical factors, experimental efficiencies of sources were calculated (Table 5.1).

As shown in all cases, the experimental efficiency is less than the theoretical possibilities. The difference between theoretical and experimental values can be explained primarily by inhomogeneous promethium oxide distribution in the source. The large promethium oxide particles have a much higher density than the sol-gel media and the electron emissions are counterproductively absorbed in these particles. It is possible that using a finer powder of promethium oxide with homogeneous particle distribution will approach the theoretical limit.

**Table 5.1. Characteristics of Pm-147 sources.**

Number and type of sources	Activity, Ci (on date of fabrication)	Active area of source, cm <sup>2</sup>	Mass thickness of layer, mg/cm <sup>2</sup>	Specific activity of layer, Ci/mg	Measured current, nA	Geometrical factor (calculated)	Efficiency of source, %	
							Calculated	Measured
BPm7-MU08-1 Round	2.14	5.1	4.4	0.097	1.86	0.43	40	34
BPm7-MU08-2 Round	0.41	5.1	1	0.08	0.61	0.43	63	58
BPm7-MU08-3 Rectangular	0.80	6	1.45	0.092	1.12	0.81	59	30
BPm7-MU08-4 Rectangular	0.43	6.3	0.7	0.096	0.99	0.81	67	49
BPm7-MU08-5 Rectangular	0.49	8.5	0.35	0.16	1.15	0.81	73	50
BPm7-MU08-6 Rectangular	2.6	17.1	0.72	0.21	6.0	0.85	67	61

## 5.2. EXPERIMENTAL SETUP FOR TESTING PM-147 DIRECT CHARGE NUCLEAR BATTERY

Two designs of Pm-147 nuclear batteries were built; parallel plane geometry with round sources and cylindrical geometry with rectangular sources.

From the fabricated sources listed in Table 5.1, the sources BPm7-MU08-2 Round and BPm7-MU08-6 Rectangular, were used for the direct charge nuclear battery models, since these sources have a higher beta particle current. Source efficiencies were 58% and 61%, respectively.

The experimental setup for the plane geometry battery is shown in Figure 5.4. In this battery the source and stainless steel collectors, all with diameters of 50 mm, were placed in a Teflon holder (see Figure 5.4) at an interelectrode distance of 20 mm. The Pm-147 cell was placed in the vacuum chamber under residual pressure less than  $10^{-4}$  Torr. A voltage divider consisting of 50 TOhm and 1 GOhm resistors, and a block of 1 TOhm load resistors were also put in a vacuum to reduce discharge at high accumulated voltage. A Keithley K6514 electrometer was used for measuring the current through the different load resistors, and a Keithley K237 multimeter was used for measuring the voltage on a 1 GOhm voltage divider, as shown.

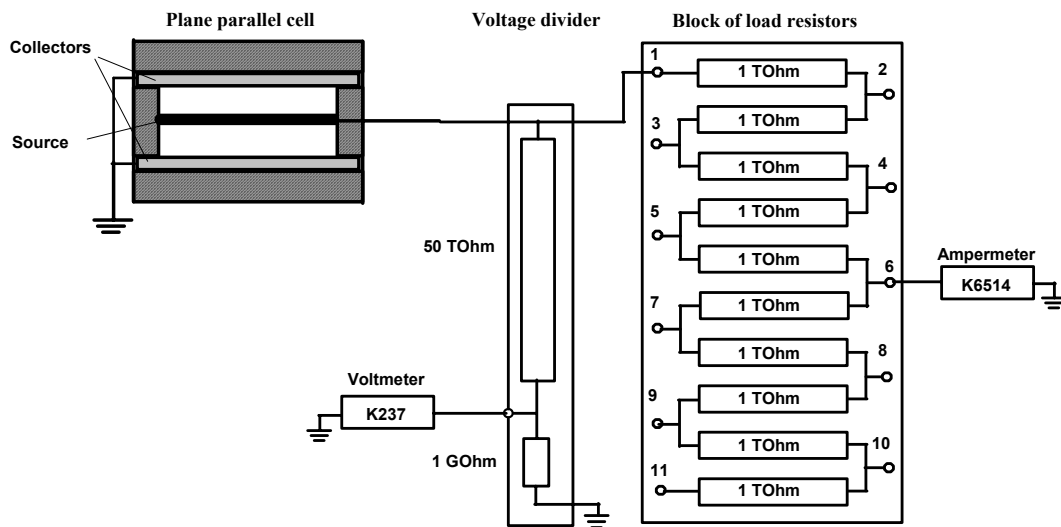


Figure 5.4. Experimental setup for plane geometry battery performance testing

The direct charge nuclear battery model with a rectangular source was made using cylindrical geometry. The rectangular source had overall dimensions of 10.2 cm × 3.3 cm × 0.16 cm and the area of the radioactive isotope was approximately  $S=17 \text{ cm}^2$  (one side). The direct charge nuclear battery model was made in a cylindrical vacuum enclosure with an inner diameter of 54 mm and a length of 150 mm. An overview of this vacuum enclosure is shown in Figure 5.5. On one side of the vacuum enclosure was mounted a high-voltage electrical feed-through produced by CeramTec North America Corporation (2003-2008) with a specified electrical breakdown greater than 50 kV (see Figure 5.6).

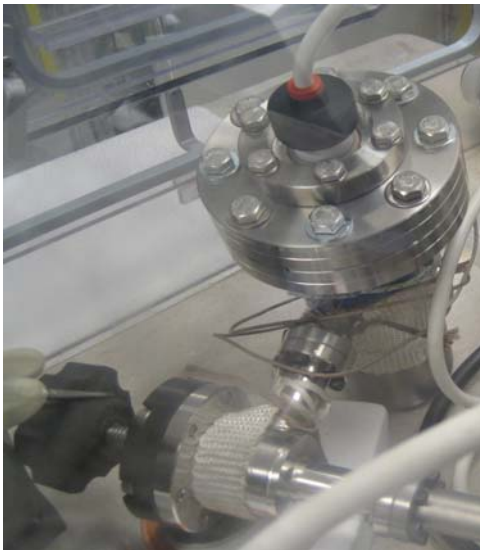


Figure 5.5. The overview of the vacuum enclosure for Pm-147 direct charge nuclear battery of cylindrical model

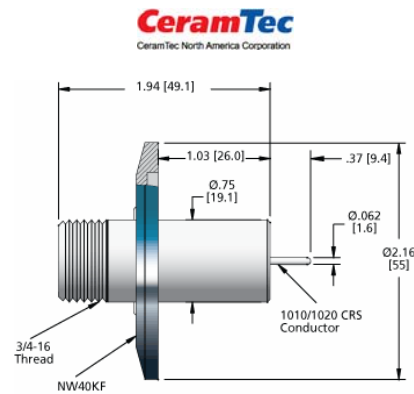


Figure 5.6. The high-voltage electrical feed-through produced by CeramTec North America Corporation

The promethium-147 source was attached to the central electrode of the feed-through coaxially with the cylinder enclosure. The cylindrical surface of the vacuum enclosure had a valve connected to a vacuum pump. The battery was maintained at a pressure of less than  $5 \cdot 10^{-5}$  Torr.

The experimental setup for a promethium direct charge battery with cylindrical geometry is shown in Figure 5.7. The promethium-147 source (1, Fig. 5.7) with an activity of 96 GBq (2.6 Ci) was mounted in the vacuum enclosure (2) as described above. The body of the battery (electron collector) was grounded.

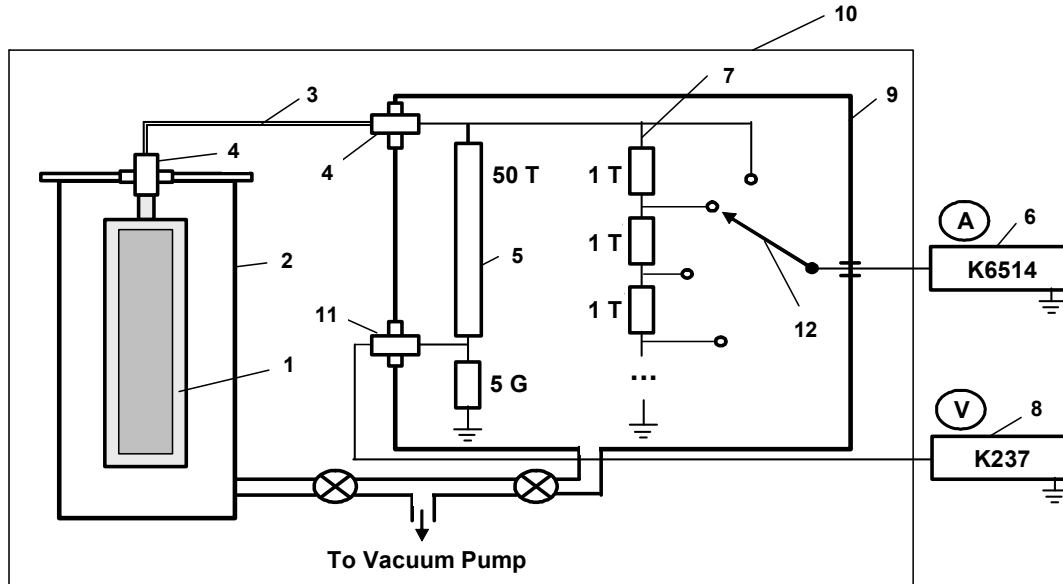


Figure 5.7. Experimental setup for the promethium direct charge nuclear battery with cylindrical geometry. 1 – rectangular promethium-147 source on metallic substrate; 2 – vacuum enclosure; 3 – high-voltage cable; 4 – high-voltage electrical feed-through; 5 - high voltage divider; 6 – electrometer Keithley-6514; 7 – voltage divider; 8 – voltmeter Keithley-237; 9 – vacuum chamber; 10 – glove box; 11- electrical feed-through; 12 – switch

When the residual pressure in the vacuum enclosure fell below  $10^{-3}$  Torr, the charging process began. Positive high voltage accumulated on the source which served as an electrode in this configuration. A high voltage cable (3) was connected to the electrical feed-through (4). An independently calibrated voltage divider (5) was used to directly measure accumulated voltage. This divider was made of 50 TΩ and 5 GΩ resistors connected in series. The voltage drop on the 5 GΩ resistor was measured with a Keithley 237 voltmeter

(8). The voltage on the direct charge battery was determined from the voltage measured on the 5 GOhm resistor. This voltage was then multiplied by the ratio of the voltage divider, which was approximately 10,000. The voltage divider had been previously calibrated using an external high voltage power supply. An advantage of using the voltage divider over an electrostatic method was that adjustment of the load resistors (7) could be connected to the self-charged battery in parallel to determine the matched impedance where efficiency was optimized. The current through the load was measured directly as well. An amperemeter Keithley 6514 (6) was placed between the load resistor and the ground for current measurement. The high voltage divider was set in the vacuum chamber (9) to prevent spontaneous high voltage discharge. The minimum residual pressure needed according to Lazarenko et al.<sup>3</sup> and Rappaport and Linder<sup>4</sup> for direct charge nuclear battery is  $10^{-4}$  Torr. The experiment was performed inside a glove box (10) for radiation protection.

### 5.3 TESTING RESULTS OF PM-147 DIRECT CHARGE NUCLEAR BATTERY, EFFICIENCY OF PM-147 DIRECT CHARGE NUCLEAR BATTERY

The purpose of the experiments and discussion was to determine the characteristics of Pm-147 DCNB in two geometries: charging current, process of voltage accumulation and level of saturation, and efficiency of batteries and comparison of the experimental results with a theoretical description of the charging process.

#### 5.3.1 Pm-147 battery of plane geometry

##### 5.3.1.1 Testing of the plane geometry Pm-147 battery

The building and testing of the plane geometry cell was done for confirming the characteristics of the materials used in building cell holders, feed through, and wires for very high voltage use.

The experiments used the setup shown in Figure 5.4.

Active loads were connected to the direct charge battery in the experiments resembling two resistor banks connected in parallel. Experiments with 60 TOhm used these resistors connected in series. One resistor bank was a  $R_{div}=50$  TOhm voltage divider and the other was a set of 1 TOhm resistors connected in series. Therefore the total resistance of the active load  $R_{load}$  was

$$R_{load} = \left( \frac{1}{R_{div}} + \frac{1}{R_{load}} \right)^{-1} \quad (5.2)$$

where  $R_{load}$  was the total resistivity in a set of 1 TOhm resistors connected in series.

Results of experiments with different load resistors are shown in points in Figure 5.8. The numerical solutions of Equation (3.39) take into account the increasing repulsion of beta particles by collector voltage as shown by the curves in Figure 5.8.

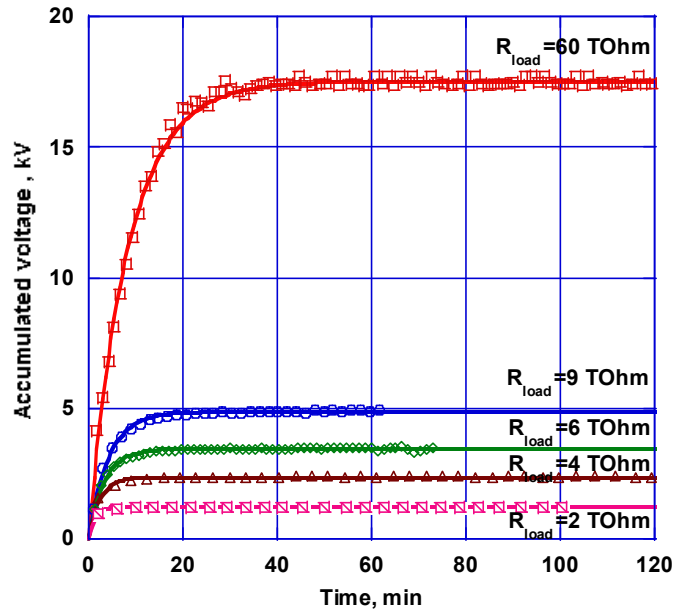


Figure 5.8. Accumulated voltage with time for Pm-147 DCNB in plane geometry



Figure 5.9 shows the dependence of the current through the load resistor and voltage at saturation versus load resistor. Points are experimental data; curves are fit by Equations (5.3) and (4.16) using MathCad.

$$U_{sat} = I_{sc} \cdot \left( \frac{1}{R_{cell}} + \frac{1}{R_{div}} + \frac{1}{R_{load}} \right)^{-1} \cdot \eta_R(U_{sat}) \quad (5.3)$$

Self-leakage resistance of the capacitor  $R_{cell}$  was used as a fitting parameter. The other components

$$R_{leak} = \left( \frac{1}{R_{cell}} + \frac{1}{R_{div}} + \frac{1}{R_{load}} \right)^{-1}, \quad (5.4)$$

$R_{div}$  and  $R_{load}$ , were known from the conditions of the experiment.

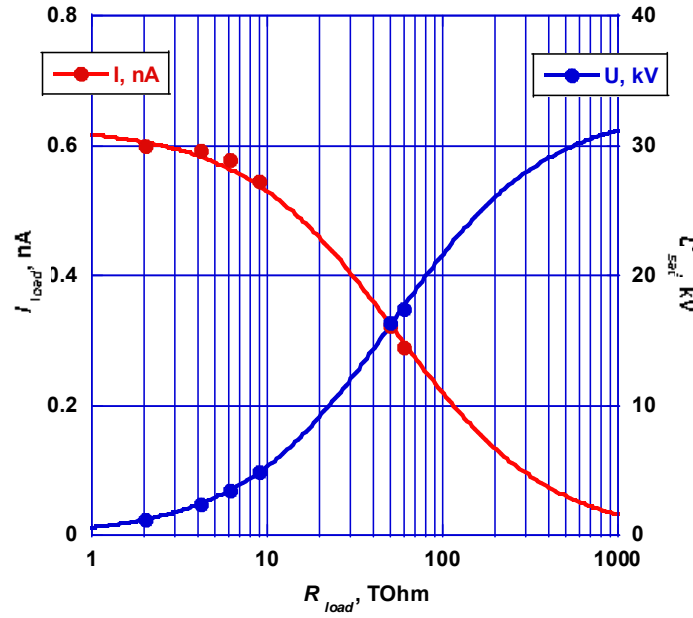


Figure 5.9. Current through load resistor and voltage at saturation against load resistor for Pm-147 DCNB with plane geometry. Points are experimental data, curves are approximated with Equations (5.3) and (4.16)

### 5.3.1.2 Efficiency of the plane geometry Pm-147 battery

The electrical power on load,  $P_{el}$ , calculated as a product of  $U_{sat}$  and  $I_{load}$  versus load is shown in Figure 5.10. As one can see, at  $R_{load}=50$  TOhm there is a maximum of approximately 5.2  $\mu$ W. In addition, the dependence of overall efficiency versus load resistivity calculated by Equation (5.5). is represented on this plot.

$$\xi = \frac{P_{el}}{10^9 \cdot A \cdot 1.6 \cdot 10^{-16} \cdot \varepsilon_{avg}} = \frac{P_{el}}{9.9 \cdot A} \cdot 10^6 \quad (5.5)$$

$$\left( \xi = \frac{P_{el}}{3.7 \cdot 10^{10} \cdot A \cdot 1.6 \cdot 10^{-16} \cdot \varepsilon_{avg}} = \frac{P_{el}}{367 \cdot A} \cdot 10^6 \right)$$

$A$  is the activity of the source in GBq (or in Ci using equation in parentheses) and 9.9  $\mu$ W/GBq (or 367  $\mu$ W/Ci for equation in parentheses) is the specific heat of Pm-147.

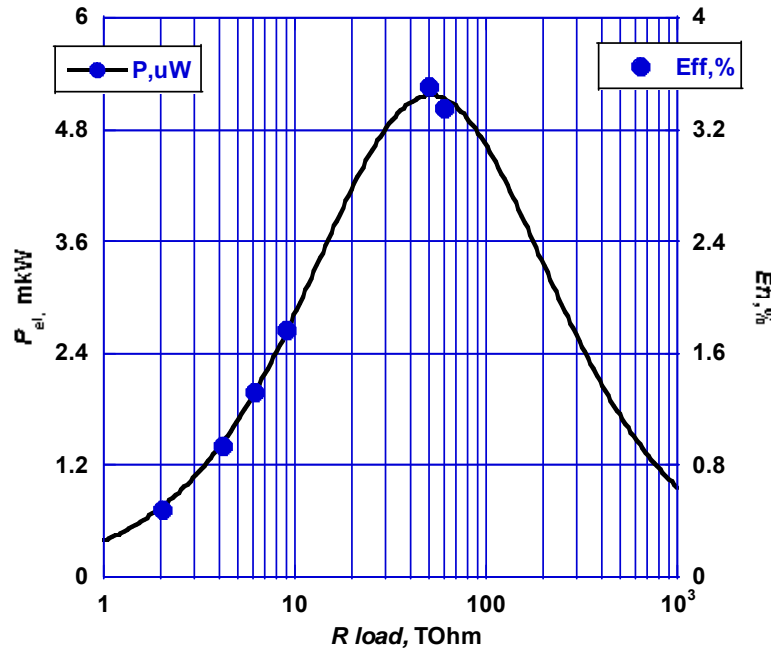


Figure 5.10. Output electrical power on load and overall efficiency vs. load resistor

As illustrated in Figure 5.10, the efficiency of the Pm-147 battery with plane geometry is optimal at 3.5%. The theoretical estimate of efficiency using Equation (3.3) is given in Table 5.2. Obviously, the theoretical estimate and the experimental results compare favorably, confirming the theoretical considerations.

**Table 5.2. Estimation of the theoretical efficiency for plane geometry of Pm-147 battery**

<b>Factor influencing efficiency of DCNB</b>	<b>Value of factor, arb.un.</b>
Efficiency of source (for $4\pi$ geometry), $\eta_S$	0.58 (see Table 5.1)
Geometrical factor, $k_g$	0.43 (see Table 5.1)
Effect of accumulated voltage, $\frac{U \cdot \eta_R(U)}{\mathcal{E}_{avg}}$ (at voltage for optimal load resistor)	0.35 (at 18 kV, Figure 3.10b)
Secondary electron yield, $s$	$0.07^{5,6}$
Backscattering yield, $b$	0.24 (see Figure 3.17)
Theoretical efficiency of Pm-147 battery	3.1%
Experimental efficiency	3.5%

In order to improve the efficiency of the Pm-147 DCNB, cylindrical geometry and collector coatings were used in the next experimental models.

### 5.3.2 Pm-147 battery with cylindrical geometry

#### 5.3.2.1 Testing of the Pm-147 battery with cylindrical geometry

In experiments with the Pm-147 battery with cylindrical geometry two types of collectors were compared: a bare stainless steel electrode and an aluminum electrode coated with polyimide insulation. As previously illustrated,<sup>5,6</sup> the secondary electron yield for iron is 0.07 for the average energy of the promethium beta particles. The backscattering electrons coefficient for an iron collector is approximately 0.24. Carbon and polyimide coatings on collectors reduced the secondary electron yield to 0.027 and the backscattering coefficients to 0.03 (see part. 3.2.5, Figure 3.17). The second type of collector reduced emissions of secondary electrons and backscattering (as compared to the first) because it contained materials with lower atomic numbers and organic coatings. These materials and coatings suppressed low energy secondary electron emission (see part 3.2.4 and 3.2.5). The wall of the vacuum enclosure served as a stainless steel collector. The aluminum collector with thin polyimide coating was made from thin wall aluminum tubing with an outside diameter equal to the inner diameter of the vacuum enclosure. The direct charge battery experiments were carried out with several values of load resistors in the terohm range.

The results of the experiments are shown in Figures 5.11 and 5.12. The points on these plots are experimental data, while the curves are fit to Equation (3.39) taking into account the beta flux with sufficient energy to reach the collector under increasing voltage accumulation. In all cases, the voltage increased to saturation in less than 50 minutes. After reaching steady state (leakage = charge current) the voltage was stable.

Occasionally a spontaneous discharge reset accumulation. The frequency of spontaneous discharge depended on the matching load. At 10 kV with load 2 TOhm, the spontaneous discharge occurred every 2.5 hours, while at 25 kV with load 5 TOhm, discharge was hourly. Resistors were mounted in smooth Teflon and discharges were probably caused by flashover of Teflon in vacuum.<sup>7</sup> Replacement of Teflon with another insulator material, such as ceramic, might eliminate this shorting problem.

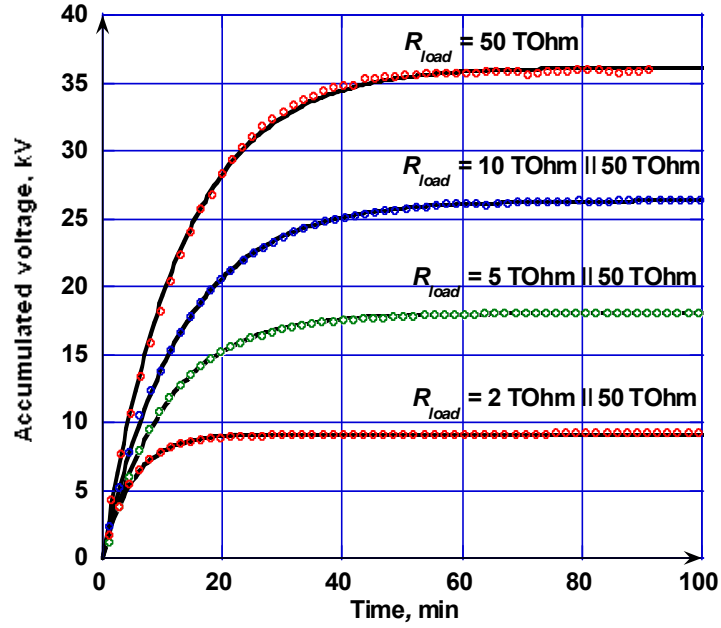


Figure 5.11. Accumulated voltage on the Pm-147 direct charge nuclear battery with a 2.6 Ci source and stainless-steel collector with time at different loads. Points are experimental data, while curves are approximation by solution of Equation (3.39)

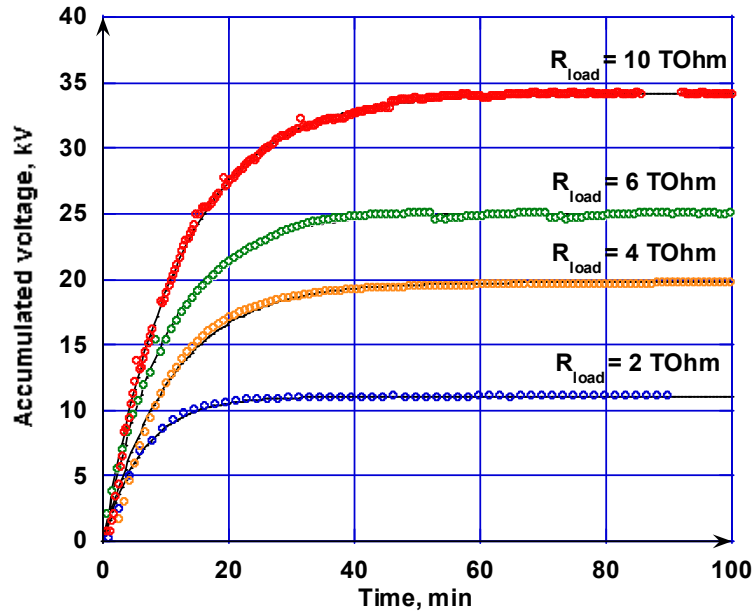


Figure 5.12. Accumulated voltage on the Pm-147 direct charge nuclear battery with 2.6 Ci source and polyimide coated aluminum collector against time at different loads. Points are experimental data, while curves are approximation by solution of Equation (3.39)

Active loads were connected to the direct charge battery in the experiments as two resistor banks connected in parallel. One resistor bank was a  $R_{div}=50$  TOhm voltage divider and the other was a set of 1 TOhm resistors connected in series. Therefore, the total resistance of the active load  $R_{load}$  was calculated by Equation (5.2).

The voltages for saturation versus load resistance are plotted in Figure 5.13 for the stainless steel collector and for aluminum collector with polyimide coating. The points on this plot are experimental results (experimental level of saturation from Figures 5.11 and 5.12), and curves are fit by Equation (5.3).

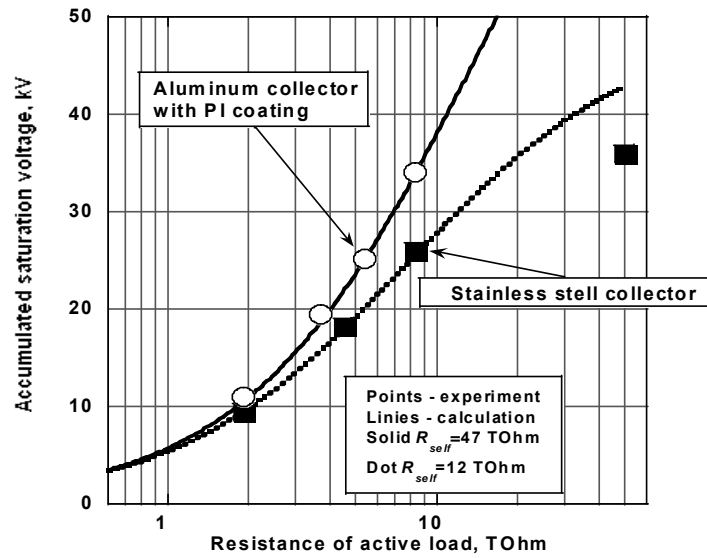


Figure 5.13. Accumulated saturation voltage produced on the load by direct charge Pm-147 nuclear batteries with different types of collectors versus load resistance. Points are experimental data, while curves are approximations by solution of Equation (5.3)

Self-leakage resistance of the battery,  $R_{cell}$ , was used as a fitting parameter. The other components  $R_{leak}$ , especially  $R_{div}$  and  $R_{load}$ , were known independently from the conditions of the experiment. Using the stainless steel collector, self-leakage resistance was 12 TOhm, while the battery with aluminum collectors and polyimide coating had a self-leakage resistance of 47 TOhm. Using these values, the charging curves (Figures 5.11 and 5.12) were approximated as solutions of Equation (3.39). The value of the capacitance in the experiments was the sum of the capacitances from the cell, cables, and connected devices.

The best fit of the experimental curves were at capacitance of  $170 \pm 30$  pF in all cases. The measured value of the full capacitance of the system was in the same range.

#### 5.3.2.2. Efficiency of Pm-147 battery with cylindrical geometry

The useful electrical power on the load,  $P_{el}$ , and the overall efficiency of converting radioactive decay power to electrical power can be calculated from the measured values of accumulated voltage. The electrical power,  $P_{el}$ , in watts, and the efficiency  $\xi$  were estimated by Equations (5.6) and (5.5):

$$P_{el} = \frac{U_{sat}^2}{R_{load}} \quad (5.6)$$

The conversion efficiencies versus load resistance for the promethium-147 battery with different collectors are plotted in Figure 5.14. As can be seen from this plot, the efficiency (power) depends on  $R_{load}$  and has a maximum.

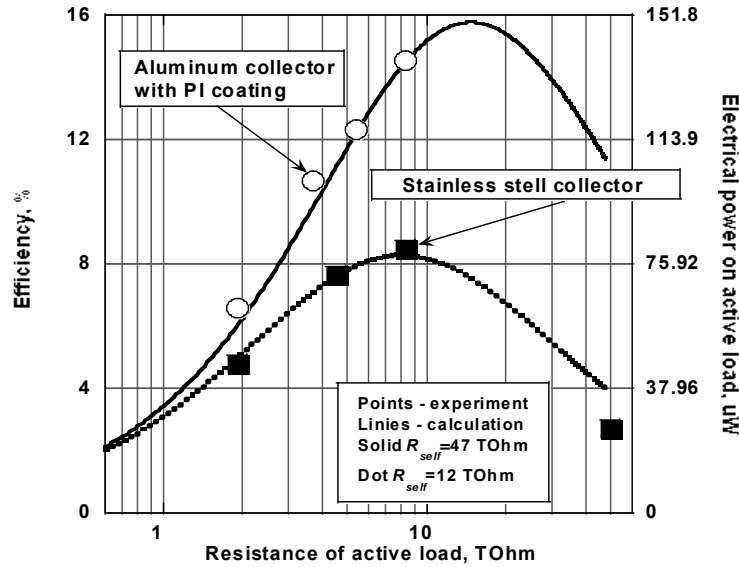


Figure 5.14. Efficiency and electrical power produced on load by Pm-147 direct charge nuclear battery with different types of collector versus load resistance. Points are experimental data; curves are approximations by solution of Equations (5.5) and (5.6)

At best, the promethium-147 direct charge battery with a source activity of 96 GBq (2.6 Ci) and polyimide coated collector, with a load of 8.3 TΩ produced 140 μW electrical power with an efficiency of 14 %. The theoretical estimation of the efficiency from Equation (3.3) is given in Table 5.3. As one can observe from this Table and from Figure 5.14, the experimental results compare favorably with the theoretical estimation.

**Table 5.3. Estimation of the theoretical efficiency for cylindrical geometry of Pm-147 battery**

Factor influencing efficiency of NB	Value, arb.un.	
	Bare SS	Al collector with PI coating
Efficiency of source (for $4\pi$ geometry), $\eta_s$	0.61	0.61 (see Table 5.1)
Geometrical factor, $k_g$	0.85	0.85 (see Table 5.1)
Effect of accumulated voltage, $\frac{U \cdot \eta_R(U)}{\mathcal{E}_{avg}}$ (at voltage for optimal load resistor)	0.4 (at 28 kV)	0.55 (at 45 kV, Figure 3.10b)
Secondary electron yield, $s$	0.07	0.03 (see Figure 3.14)
Backscattering yield, $b$	0.24	0.03 (see Figure 3.17)
Theoretical efficiency of Pm-147 battery	7.4%	13.4%
Experimental efficiency	8%	15%

The efficiency of the demonstrated Pm-147 DCNB is less than the estimated theoretical possibility due to:

- the geometrical factor for this DCNB is 0.85, compared with a possible value of 0.95;
- the source efficiency is 61%, which is less than possible value of 80%.

If these factors are taken into account, the experimental efficiency of Pm-147 DCNB with cylindrical geometry will be comparable with an upper theoretical estimate of 21%.

As demonstrated in these experimental results, the design of direct charge nuclear batteries with effective promethium beta sources and collectors having low backscatter gives the efficiency predicted for these devices.



## REFERENCES

- <sup>1</sup> <http://www.nndc.bnl.gov/nudat2/>
- <sup>2</sup> V. V. Bochkarev, G. B. Radsievsky, L. V. Timofeev, and N. A. Demianov, "Distribution of absorbed energy from a point beta source in a tissue-equivalent medium," *Int. J. of Applied Radiation and Isotopes*, **23**, 493 (1972).
- <sup>3</sup> Yu.V. Lazarenko, A.A. Pystovalov, and V.P. Shapovalov, "Desk-size Nuclear Sources of the Electricity Energy," *Energoatomizdat*, Russia (1992).
- <sup>4</sup> P. Rappaport, E.G. Linder, "Radioactive Charging Effects with Dielectric Medium," *Journal Applied Physics* **24**, 9 (1953).
- <sup>5</sup> [http://www.ccmr.cornell.edu/igert/modular/docs/3\\_Scanning\\_Electron\\_Microscopy.pdf](http://www.ccmr.cornell.edu/igert/modular/docs/3_Scanning_Electron_Microscopy.pdf)
- <sup>6</sup> A.-G. Xie, H.-F. Zhao, B. Song, and Y.-J. Pei, "The formula for the secondary electron yield at high incident electron energy from silver and copper," *Nuclear Instruments and Methods in Physics Research B* **267**, 1761 (2009).
- <sup>7</sup> H.G. Miller, "Flashover of insulators in vacuum. Review of the Phenomena and Techniques to improve hold off voltage," *IEEE Transactions on Electrical Insulation* **77** (4), 512 (1993).
- <sup>8</sup> <http://www.nndc.bnl.gov/chart/chartNuc.jsp>
- <sup>9</sup> G. F. Knoll, "Radiation Detection and Measurement," 3<sup>th</sup> ed., John Wiley&Sons (2000).
- <sup>10</sup> <http://physics.nist.gov/PhysRefData/XrayMassCoef/tab4.html>
- <sup>11</sup> <http://physics.nist.gov/PhysRefData/XrayMassCoef/tab2.html>

## CHAPTER 6

### TRITIUM NUCLEAR BATTERY WITH SOLID DIELECTRIC

#### 6.1 OPERATIONAL PRINCIPLE OF NUCLEAR BATTERY WITH SOLID DIELECTRIC

Direct charge tritium batteries with vacuum dielectric were fabricated and successfully tested. Despite the advantages of this type of battery, multi-millimeter vacuum spacers make the large surface area device relatively large in volume.

To reduce the size of direct charge nuclear batteries, a thin layer of solid dielectrics can be used instead of a vacuum dielectric. For a reasonable fraction of tritium beta particles to reach the collector, the solid dielectric should not be thicker than several hundred nanometers. Even so the loss of the beta particles will be significant. Consider the direct charge nuclear battery consisting of a tritium beta particle source, a layer of solid dielectric and a collector. We observe here a dielectric with volume resistivity  $\rho_v = 2.3 \cdot 10^{16} \text{ Ohm} \cdot \text{cm}^{-1}$  (Kapton film), and source with beta particles flux density  $dI_\beta/dS = 100 \text{ pA/cm}^2$ . Then the surface activity of the source calculated by Equation (4.4) will be about  $73 \text{ mCi/cm}^2$  (efficiency of the source at 23%, see paragraph 4.1.1). As shown in Table 3.1, the mass absorption coefficient of tritium beta particles is  $15.1 \text{ cm}^2/\text{mg}$ . The charging current density,  $dI_{Ch}/dS$ , will decrease due to absorption of beta particles into the dielectric layer and can be estimated as

$$\frac{dI_{Ch}}{dS} = \frac{dI_\beta}{dS} \cdot \exp(-\nu \cdot d_m \cdot t_m) \quad (6.1)$$

where  $d_m$  is the dielectric density in  $\text{mg/cm}^3$ , and  $t_m$  is the dielectric thickness in cm.

If the resistivity  $R_{sq}$  of  $1 \text{ cm}^2$  of dielectric is  $2.3 \cdot 10^{16} \cdot t_m$ , then the open circuit voltage of the battery will equal  $U_{oc} = dI_{Ch}/dS \cdot R_{sq}$ . Useful electrical power on an optimal load can be calculated by Equation (2.12). The calculated useful electrical power dependency with the thickness of dielectric has maximum at  $0.25 \cdot 10^{-4} \text{ cm}$  in this example. Dependency of the

overall efficiency of the direct charge battery with a solid dielectric with the load resistor was calculated by Equation (2.14) where instead  $P_{el,max}$  was used  $P_{el}$  calculated by Equation (2.11) (see Figure 6.4). The maximal overall efficiency gives a value near 0.02%.

Many authors<sup>2,3,4,5</sup> have investigated the steady-state current which are induced in short-circuited dielectrics by electron beams with electron range less than the sample thickness. The investigations can be done with the setup shown in Figure 6.1.<sup>6</sup> A dielectric sample is sandwiched between two electrodes (A and B). Electrodes less than 500 Å thick do not absorb a significant fraction of the incident electron beam. Measurements of the current are made independently for each electrode. The range of the electron beam can vary from small to large where it is greater than the sample thickness.

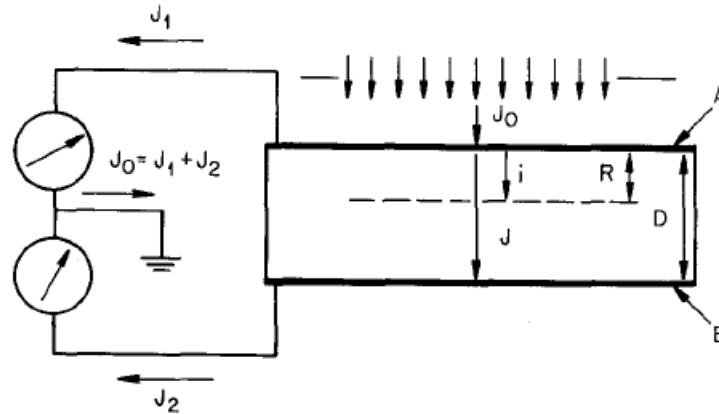


Figure 6.1. Split Faraday cup. A – front electrode, B – rear electrode,  $J_0$  – beam current,  $i$  – injection current,  $J_1$  – front current,  $J_2$  – rear current,  $J$  – dielectric current,  $R$  – centroid of charge distribution,  $D$  – sample thickness<sup>7</sup>

It was found that significant current can flow through the rear electrode even when the extrapolated range of the electrons are less than thickness of sample. This effect, named the threshold effect is described<sup>2,3,4,5</sup> for different materials including  $As_2S_3$ ,  $Al_2O_3$ , mica, Pyrex, Teflon,  $Ta_2O_5$ , and for electron energy 1-45 keV. The current begins to flow through when the electron range is approximately equal to half the thickness of the sample. Formation of a space charge region inside the dielectric functions as a virtual electrode.

Based on the above-mentioned experimental facts another fabrication option for the tritium nuclear battery was considered. This battery with direct charge accumulation will use a thick solid dielectric such that all beta particles are stopped in the dielectric where a charge is accumulated (the thickness of dielectric exceeds the beta particles range). The electric field due to this space charge will create an electrical current toward the collector. If the thickness and conductivity of dielectric are chosen properly, a useful current through the collector can be developed. For analysis of this approach, we assume the beta particles from a source in a “sandwich” metal-source-dielectric-metal configuration accumulate in a charge domain in the dielectric (see Figure 6.2). Due to this charge, an electric field develops (see sketch in Figure 6.2). The electrical capacitance of this domain with a grounded metal plate is  $C_{int}$ . Some electrical charge from this domain will leak to the upper and lower metal electrodes. Leakage from the charge domain to the emitter is denoted as leakage current,  $I_{leak}$ , and resistance between the dielectric charged domain and lower and upper metal plates as  $R_1$  and  $R_2$  respectively. The equivalent circuit is shown in Figure 6.3.  $C_{ext}$  is the capacitance between the two metal plates.  $R_{load}$  is the load resistor.

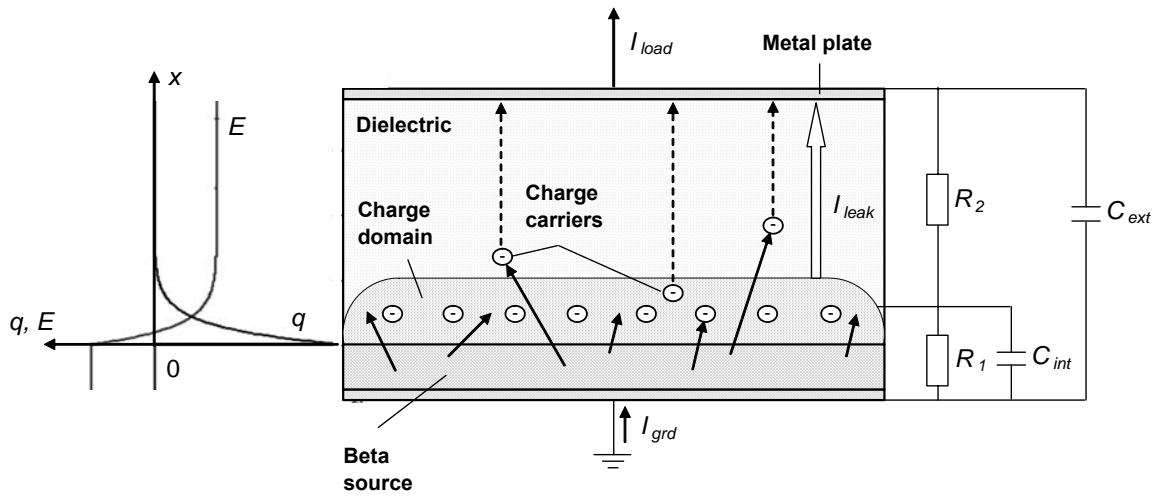


Figure 6.2. Scheme of charge accumulating into dielectric under beta source irradiation

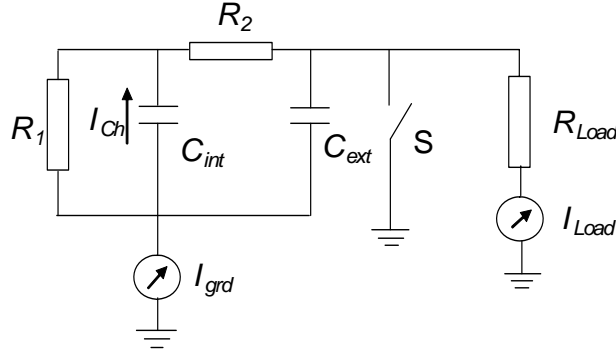


Figure 6.3. Equivalent circuit for calculation of  $I_{grd}$  and  $I_{load}$  with time

It is possible to describe the voltage on the internal and external capacitors ( $U_1$  and  $U_2$ , respectively) as

$$\frac{dU_1}{dt} + \frac{U_1}{C_{int} \cdot R_1} + \frac{U_1 - U_2}{C_{int} \cdot R_2} = \frac{I_{Ch}}{C_{int}} \quad (6.2)$$

$$\frac{dU_2}{dt} + \frac{U_2}{C_{ext} \cdot R_{load}} = \frac{U_1 - U_2}{C_{ext} \cdot R_2} \quad (6.3)$$

The steady state ( $dU/dt=0$ ) voltage on the external capacitor can then be calculated as:

$$U_2 = I_{Ch} \cdot \frac{R_1 \cdot R_{load}}{R_1 + R_2 + R_{load}} \quad (6.4)$$

Useful electrical power on the load resistor and efficiency can be calculated as:

$$P_{el} = \frac{U_2^2}{R_{load}} \quad (6.5)$$

$$\xi = \frac{P_{el}}{A \cdot \varepsilon_{avg}} \cdot 100\% \quad (6.6)$$

Assuming a beta particles flux density  $dI_\beta/dS=100$  pA/cm<sup>2</sup> and dielectric (polyimide) thickness of 10 μm, total resistivity of 1 cm<sup>2</sup> dielectric with  $\rho=2.3 \cdot 10^{16}$  Ohm·cm (Kapton film) will equal 23 TOhm. This value of  $R_2$  is assumed for efficiency estimates in our model.

Figure 6.4 shows dependencies of overall efficiency vs.  $R_{load}$  as calculated by Equations (6.6) for different ratios of  $R_1/R_2$ . As can be seen in this plot, the nuclear battery with a charged solid dielectric consistently has a significant advantage in efficiency over the direct charge battery with a solid dielectric. (The nature of  $R_1$  will be discussed later)

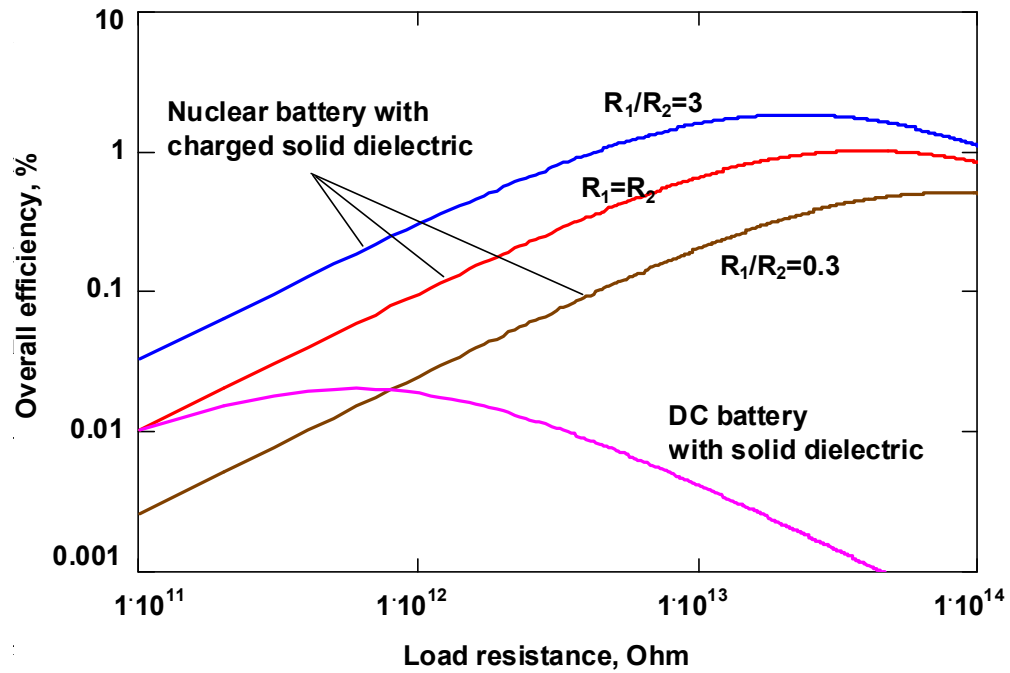


Figure 6.4. Overall efficiency of different types of tritium nuclear batteries with solid dielectric vs. load resistance

The nuclear battery with a thick dielectric has great potential for high efficiency. The behavior of the charged domain in the dielectric induced by electron beam and beta particles irradiation has important implications for research.

## 6.2 CHARGE ACCUMULATION AND STORAGE IN THE DIELECTRIC UNDER IRRADIATION

### 6.2.1 Charge accumulation under mono-energetic electron beam irradiation

Injection of electrons into many dielectrics leads to the formation of a negative space charge layer.<sup>6</sup> The general behavior of charge accumulation and storage is the same for different kind of dielectrics, but some properties vary. Some examples of space charge distribution for different dielectric materials are shown in Figures 6.5 - 6.7.

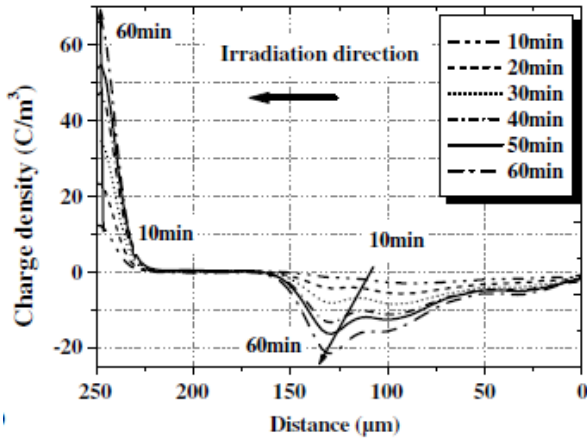


Figure 6.5. Charge distribution in 250  $\mu\text{m}$  thick polyimide sample during mono-energetic electron beam irradiation under 130 keV with a flux of  $50 \text{ pA/cm}^2$ <sup>8</sup>

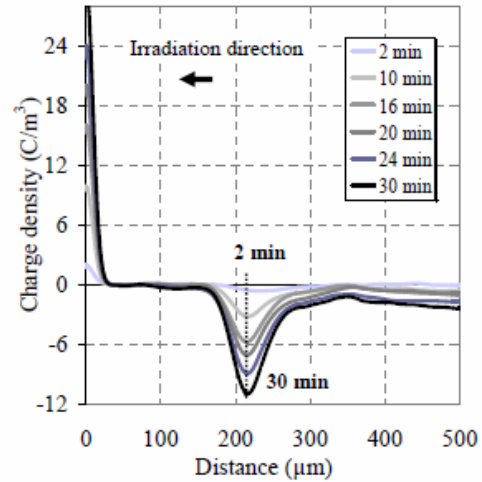
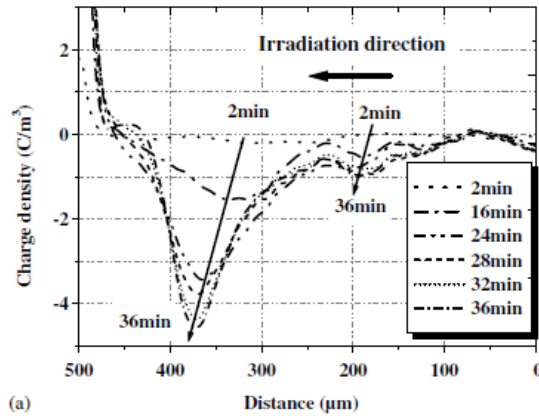
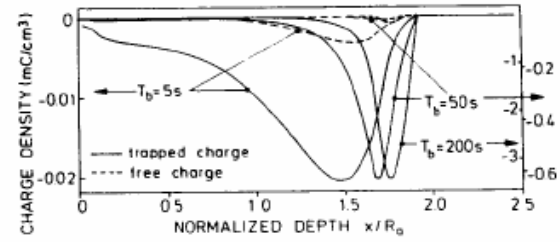


Figure 6.6. Charge distribution in 500  $\mu\text{m}$  thick polytetrafluoroethylene (PTFE) under mono-energetic electron beam irradiation (250 keV with a flux of  $50 \text{ pA/cm}^2$ )<sup>9</sup>



a



b

Figure 6.7. Charge distribution in low density polyethylene sample during mono-energetic electron beam irradiation: a) at 200 keV with a flux of  $50 \text{ pA/cm}^2$ <sup>10</sup> b) 30 keV with a flux of  $2 \text{ nA/cm}^2$ <sup>11</sup>

Generalization from these examples yields several useful observations:

- mono-energetic electron beam irradiation produces bell shaped space charge distributions; the dispersion of this distribution may depend on several factors such as the density of the dielectric, the energy of the incident beam, and the flux density of incident beam;
- the center of this distribution lies approximately at the maximum range of electrons in that material;
- in some dielectrics (for example, polyimide and PTFE) the charge centroid is stable with time; in other dielectrics the centroid of space charge distribution changes with time (for example, polyethylene).



### 6.2.2. Charge accumulation under tritium beta irradiation

In the above described cases, the electron beam uses mono-energetic electrons, so the range of each electron is approximately the same and space charge peaks at the centroid of the charge distribution. In the case of tritium beta particle irradiation with a continuous energy spectrum, the volume space charge is deposited in the medium from the front electrode closest to the source, to the maximum range of these particles in that medium.

The calculation of beta particles ranges (in this case for polyimide) can be done using different methods. Casino v.2.42<sup>12</sup> is an available Monte Carlo simulation code. This code is easy to use. Although the calculations are not extremely accurate,<sup>13</sup> they are adequate for estimates.

The calculation of the distribution of penetration depth of electrons  $n(r_\beta, \varepsilon)$  with energy  $\varepsilon$  (keV) from the range of tritium beta particles  $r_\beta$  (nm) (from 1 to 18 keV in 1 keV steps) was done. The chemical properties of polyimide used the NIST database<sup>14</sup>  $C_{22}H_{10}N_2O_5$ , density  $1.42 \text{ g/cm}^3$ , mean excitation energy 79.6 eV. Each distribution was approximated by triangles. The slope and constant term energy dependencies for the front and rear side of triangles were approximated with power functions. Finally the triangle equation is:

$$n(r, \varepsilon) = \begin{cases} -0.014476 \cdot \varepsilon^{-1.4962} + 0.0036707 \cdot \varepsilon^{-3.4189} \times r_\beta & \text{front} \\ 0.23928 \cdot \varepsilon^{-1.5272} - 0.0073463 \cdot \varepsilon^{-3.2485} \times r_\beta & \text{back} \end{cases} \quad (6.7)$$

The examples of distribution of penetration depth of electrons by Casino and its triangles approximation are represented in Figure 6.8. The integration dependence  $n(r_\beta, \varepsilon)$  by  $\varepsilon$  taking into account the beta spectrum of tritium,  $w(\varepsilon)$ , will give the distribution of beta particles stopped in polyimide by  $r_\beta$ . This integral multiplied by the elementary charge gives the accumulated charge distribution  $Q(r_\beta)$

$$Q(r_\beta) = q_e \int_0^{\varepsilon_{\max}} n(r_\beta, \varepsilon) \cdot w(\varepsilon) d\varepsilon \quad (6.8)$$

Charge distribution in relative units is represented in Figure 6.9 (curve 1).

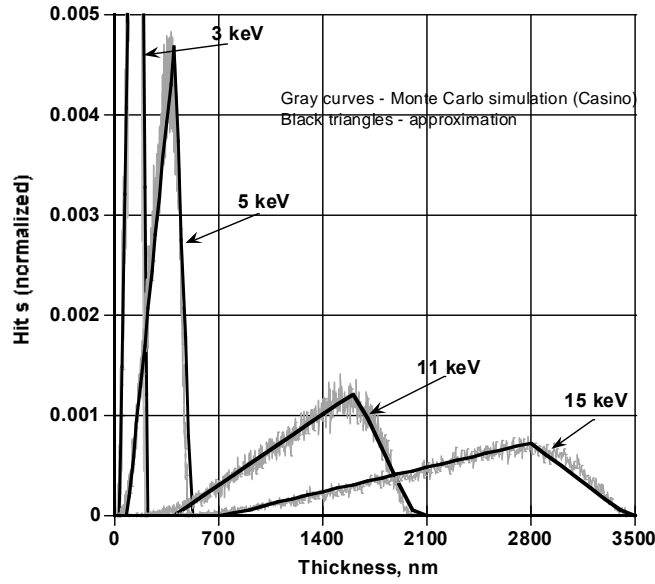


Figure 6.8. Distribution of mono-energetic electrons ranges in polyimide.  
Energy is marked on plots

Another way to calculate the charge distribution involves the use of range-energy relations. The relation given by Glendhill<sup>15</sup> as given in Equation (6.9) is as follows:

$$R(g/cm^2) = 10^{-5.1+1.358 \cdot \lg(\varepsilon)+0.215 \cdot \lg^2(\varepsilon)-0.043 \cdot \lg^3(\varepsilon)}, \varepsilon \text{ in keV} \quad (6.9)$$

This is more suitable for range calculations for tritium betas in light materials<sup>6, 16</sup> like polyimide than the more widely used equation for energy >10 keV relation of Katz and Penfold<sup>17</sup>  $R(mg/cm^2) = 412 \cdot \varepsilon^{1.265-0.0954 \cdot \ln(\varepsilon)}$ ,  $\varepsilon$  in MeV.

The charge distribution in polyimide under tritium beta irradiation can be displayed with a plot dependence of  $\frac{w(\varepsilon)}{d_m \cdot dR(\varepsilon)/d\varepsilon}$  versus  $\frac{R(\varepsilon)}{d_m}$ , where  $d_m$  is the density of polyimide. Distribution of charge in polyimide is represented in Figure 6.9 (curve 2).

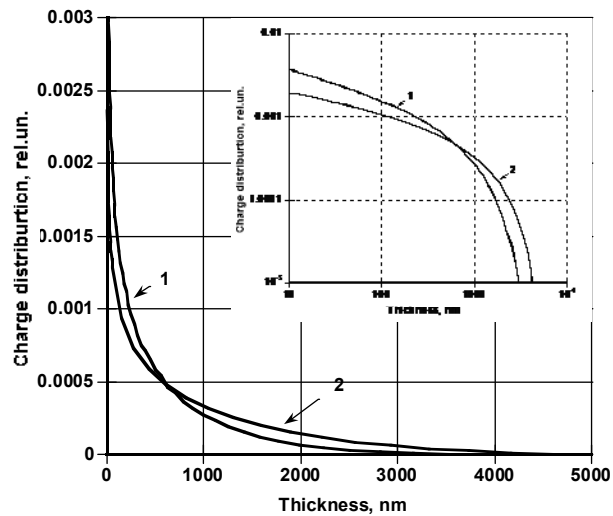


Figure 6.9. Charge distribution accumulated in polyimide from tritium beta particle irradiation. 1 - calculation using Monte Carlo simulation code (Casino v.2.42); 2 - calculation using the Glendhill<sup>15</sup> range-energy relation. Inset shows the same calculations with double logarithmic axes.

The results from both approaches are similar. Under tritium beta irradiation, the charge in polyimide will distribute from the surface to ~3-4 microns by depth.

The distribution of charge accumulated in polyimide under tritium beta irradiation was studied experimentally. A pulsed electro acoustic (PEA) method was used. Charge distribution in polyimide (Kapton), 30  $\mu\text{m}$  thick, irradiated by tritium beta particles for 30 minutes are shown in the Figure 6.10. Because of low resolution from the available mini-PEA system ( $\sim 10 \mu\text{m}$ ), we can only say that the penetration depth for tritium beta particles is not more than  $\sim 7 \mu\text{m}$ . This value is a bit higher than calculated (see Figure 6.9), perhaps due to charge transfer during irradiation or measurement error from poor resolution. For more precise results, resolution  $\sim 1 \mu\text{m}$  with special software from FiveLab can be used.

Both theoretical calculation and experimental determination of charge distribution give similar results. Tritium irradiation of polyimide gives a charged zone where the charge drops from surface to 0.5 micron in 5 times, and then continuously decreases to zero at a depth of several microns ( $\sim 5 \mu\text{m}$ ).

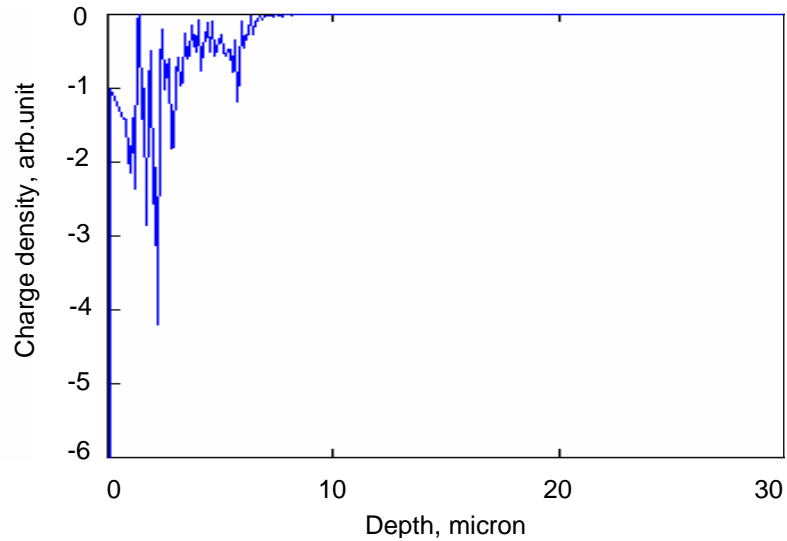


Figure 6.10. Space charge distribution in polyimide sample thickness 30  $\mu\text{m}$  (Kapton) irradiated by tritium beta particles with flux 70  $\text{pA}/\text{cm}^2$  during 30 minutes, arb. unit. Result of measurements using the pulsed electro acoustic method (Details see Appendix 6.1).

### 6.3. DIELECTRICS

The solid dielectric is an important part of the tritium battery with charged dielectric. Dielectrics for testing in the battery model were chosen based on several requirements. The dielectric should have suitable volume resistance, dielectric strength, and high radiation resistance. Some polymers have excellent dielectric strength, but degrade on exposure to radiation. In contrast, ceramic dielectrics generally have low to moderate dielectric strength and are mostly unstable to radiation with some exceptions. A solid state composite of polymer and ceramic oxide has improved dielectric properties. The desirable properties of such composites are high dielectric strength and radiation stability.

Several commercially available dielectric films were tested to determine their ability to accumulate and store energy. It is known that among polymers, polyimide is stable to ionizing radiation and has high dielectric strength (around 300  $\text{kV}/\text{mm}$  or 300  $\text{V}/\text{micron}$ ).<sup>1</sup> Using spin-coating, it is possible to prepare polyimide layers with thicknesses of several to

several dozen microns, as controlled by the speed of rotation and viscosity of polymer precursor. Cure temperatures of the polyimide precursor control the amount of residual solvent and leaving groups, thereby controlling the number of traps and energy levels.

The measurement scheme accordingly the Standard D 257-07, shown in Figure 6.11, was used to measure the volume resistivity,  $\rho$ , Ohm·m, of custom-made (TRACE Photonics, Inc. by Dr. S.M. Yousaf) samples. The volume resistivity was calculated by Equation 6.10.

$$\rho = \frac{R_{meas} \cdot S}{t_s} \quad (6.10)$$

where  $R_{meas}$  is the measured value of the resistance, Ohm,  $S$  is area of the smaller electrode, and  $m^2$ ;  $t_s$  is the dielectric sample thickness, m.

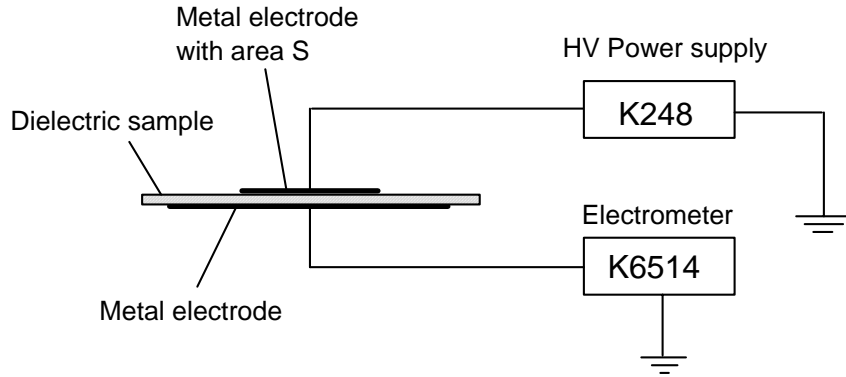


Figure 6.11. Overview of the setup for measurement of the volume resistivity of dielectric samples by standard method D 257-07.

The results of measurements and calculations are represented in Table 6.1. To verify the measurement of the volume resistivity on custom films, a commercial Kapton film was measured under identical conditions.  $2.2 \cdot 10^{14}$  Ohm·m agrees with the reference value of  $2.3 \cdot 10^{14}$  Ohm·m.<sup>1</sup>

**Table 6.1. Results of determination of the volume resistivity of dielectric samples**

Type of dielectric	Thickness, $t_s$ , $\mu\text{m}$	Area, $S$ , $\text{cm}^2$	$R_{meas}$ , Ohm	$\rho t_s = RS$ , $\text{Ohm}\cdot\text{cm}^2$	$\rho$ , $\text{Ohm}\cdot\text{m}$
Polyimide (PI)*	24	1.54	$7.3\cdot 10^{10}$	$1.12\cdot 10^{11}$	$4.7\cdot 10^{11}$
Polyimide*	29	1.54	$1.74\cdot 10^{11}$	$2.68\cdot 10^{11}$	$9.2\cdot 10^{11}$
PI-20%Gd <sub>2</sub> Zr <sub>2</sub> O <sub>7</sub> *	22	1.54	$3.5\cdot 10^{11}$	$5.39\cdot 10^{11}$	$2.5\cdot 10^{12}$
PI-15%Gd <sub>2</sub> O <sub>3</sub> *	27	1.54	$8.3\cdot 10^{11}$	$12.8\cdot 10^{11}$	$4.8\cdot 10^{12}$
		19.6	$5.2\cdot 10^{10}$	$1.01\cdot 10^{12}$	$3.8\cdot 10^{12}$
PI – 140C**	16	1.54	$4.7\cdot 10^{12}$	$7.24\cdot 10^{12}$	$4.5\cdot 10^{13}$
Kapton film	25	1.54	$3.5\cdot 10^{13}$	$5.39\cdot 10^{13}$	$2.2\cdot 10^{14}$

\* Curing of the samples was made at 90°C

\*\* Curing of the samples was made at 140°C

The values of dielectric sample thickness and calculated values of resistance of the samples with area 19.6 cm<sup>2</sup> (equal the tritium source area used for measurements) are shown in Table 6.2.

**Table 6.2. The values of thickness and resistance for different dielectric samples**

Type of dielectric	Thickness, $t_s$ , $\mu\text{m}$	$\rho$ , $\text{Ohm}\cdot\text{m}$	$R$ , Ohm
PI (TRACE)	20	$7.0\cdot 10^{11}$	$7.0\cdot 10^{10}$
PI – 140°C (TRACE)	16	$4.5\cdot 10^{13}$	$3.7\cdot 10^{11}$
Kapton	7.5	$2.3\cdot 10^{14}$	$8.8\cdot 10^{11}$
Kapton	25	$2.3\cdot 10^{14}$	$2.9\cdot 10^{12}$
Polystyrene <sup>18</sup>	25	$>10^{16}$	$>1\cdot 10^{13}$
Mylar <sup>19</sup>	18	$1\cdot 10^{16}$	$9.2\cdot 10^{13}$
20%Gd <sub>2</sub> Zr <sub>2</sub> O <sub>7</sub> -PI	22	$2.5\cdot 10^{12}$	$2.8\cdot 10^{10}$
15%Gd <sub>2</sub> O <sub>3</sub> -PI	27	$4.3\cdot 10^{12}$	$5.9\cdot 10^{10}$

The setup shown in Figure 5.4 was used for measuring the charging process for different dielectrics. The results of measurements are represented in Figure 6.12. As can be observed from Table 6.2 and Figure 6.12 the charging process is stable for the PI (TRACE, heating at 90°C) sample with thickness 20  $\mu\text{m}$  and resistance  $7.0 \cdot 10^{10}$  Ohm. For all other samples, the charging process begins with charging of the inner capacitor, and then decreases with time. Samples with higher resistance did not charge as well.

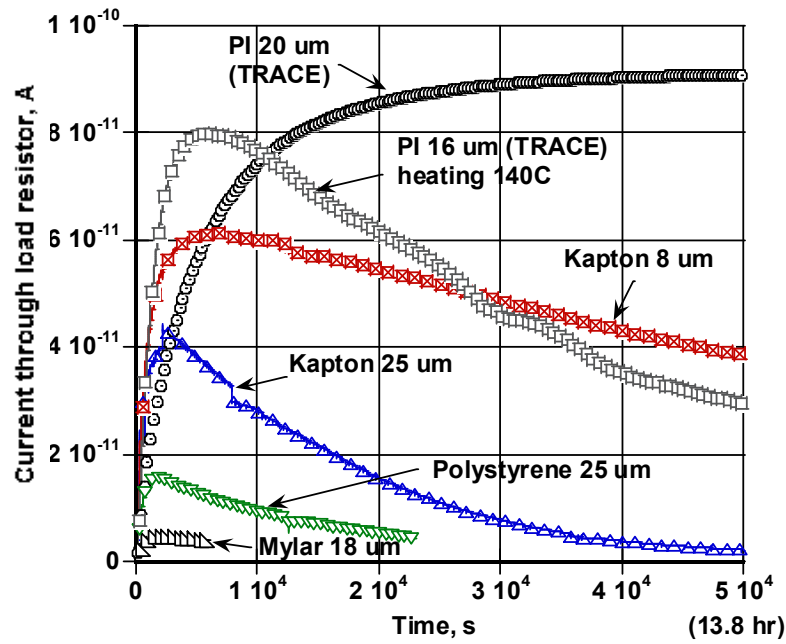


Figure 6.12. Dependencies of current through load resistor ( $R_{load}=1$  TOhm) with time on nuclear batteries with charged dielectric (tritium source with  $A=325$  mCi) for different types of dielectrics

Next, measurements were made of the current through load resistance 3.2 TOhm with time for custom-made PI (TRACE) samples with different thickness. The measured resistances at each thickness are represented in Table 6.3. The results of these measurements are shown in Figure 6.13. For PI  $\sim 1$   $\mu\text{m}$  thick, charging does not occur. Although there is a large absorption of low energy tritium beta particles in the dielectric layer (the range of tritium beta particles in PI  $\sim 5$   $\mu\text{m}$ ), there is no space charge accumulation in such a thin layer.

Increasing the PI layer thickness improves the charging with the highest level of saturation at 20-25  $\mu\text{m}$ , which corresponds to  $7 \cdot 10^{10}$ - $9 \cdot 10^{10}$  Ohm for polyimide.

**Table 6.3. The values of resistance for different thickness of PI samples**

Thickness of PI sample, $\mu\text{m}$	1	5	10	20	25
Resistance, Ohm	$3.5 \cdot 10^9$	$1.8 \cdot 10^{10}$	$3.5 \cdot 10^{10}$	$7.0 \cdot 10^{10}$	$8.8 \cdot 10^{10}$

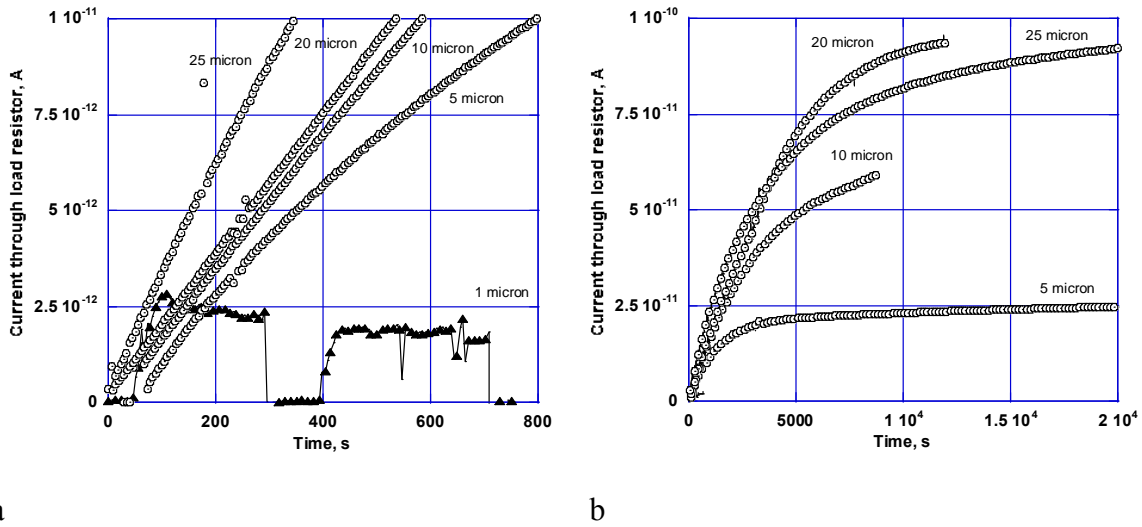


Figure 6.13. Current through load resistor ( $R_{load}=3.2 \text{ TOhm}$ ) with time of nuclear batteries with charged dielectric (tritium source with  $A=325 \text{ mCi}$ ) of different polyimide thicknesses (marked on plot): a) at the beginning of charging; b) over a prolonged time

Increase in charge traps in the dielectric improves the charge density stored. The dielectric constant and dielectric breakdown of a material need to be optimized and this may be achieved through polyimide-ceramic oxide composite formation. To develop suitable dielectric composites for the nuclear battery, metal oxides ( $\text{MgO}$ ,  $\text{Al}_2\text{O}_3$ ,  $\text{ZrO}_2$ ,  $\text{HfO}_2$ ,  $\text{Gd}_2\text{O}_3$ ,  $\text{Gd}_2\text{Hf}_2\text{O}_7$ ,  $\text{Gd}_2\text{Zr}_2\text{O}_7$ ,  $\text{La}_2\text{Zr}_2\text{O}_7$ ,  $\text{Sm}_2\text{Zr}_2\text{O}_7$ ,  $\text{Nd}_2\text{Zr}_2\text{O}_7$ ) were tested as dopants for thermoplastic polyimide.



Some of the tested composites demonstrated increased charge density stability. For instance, adding 20% of the  $\gamma$ -phase  $\text{Al}_2\text{O}_3$  (relative dielectric constant=9.3)<sup>20</sup> with average particle size 20 nm in polyimide increased the charge density stored in the dielectric layer. It increased voltage on a 1 TOhm resistor with 325 mCi tritium sources to 135 V in comparison to 90 V with pure polyimide under the same conditions. The addition of 20% of  $\text{Gd}_2\text{O}_3$  (relative dielectric constant=14)<sup>13</sup> having particle size 20-40 nm to polyimide composite gave 145 V, due to the increased dielectric constant of composite coatings. The resistance of this compound layer is approximately half that of pure polyimide (see Tables 6.2 and 6.3). The results of some measurements are shown in Figure 6.14.

Higher dielectrics in radiation stable composites were also prepared by doping polyimide with ternary oxides of lanthanides and transition metals. In these ternary oxides, radiation damage is minimized because the atoms shift to accommodate defects caused by radiation and regain the initial crystalline state. For example, gadolinium hafnate,  $\text{Gd}_2\text{Hf}_2\text{O}_7$  has been reported to have remarkable radiation resistance when subjected to 1 MeV of  $\text{Kr}^+$  irradiation.<sup>21</sup>

As was shown, the thickness of dielectric layer affects dielectric charging. Experimentally it was determined that the composite dielectrics with thickness 15-25  $\mu\text{m}$ , best accumulate and store electron charge. So this composite dielectric (polyimide with 10-20%  $\text{Gd}_2\text{O}_3$ ,  $\text{Gd}_2\text{Hf}_2\text{O}_7$ ,  $\text{Nd}_2\text{Zr}_2\text{O}_7$ ) is more suitable to use in a tritium battery with charged dielectric, and it was therefore investigated.

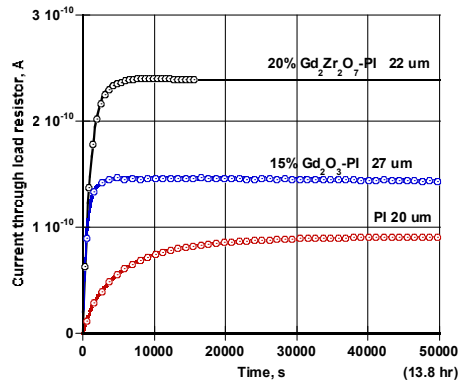


Figure 6.14. Dependencies of current through load resistor ( $R_{load}=1$  TOhm) with time on nuclear batteries with charged dielectric (tritium source with  $A=325$  mCi) for different types of dielectrics

#### 6.4. NUCLEAR BATTERY WITH CHARGED DIELECTRIC MODEL AND EXPERIMENTAL SETUP

To test the workability of the tritium nuclear battery with charged dielectrics, battery models were constructed. The model uses a tritium source, a dielectric layer, and a metal collector. The tritium sources used were PitU-50 type with activity 500 mCi and 1 Ci (see Table 4.1). The composite dielectric on the base of polyimide was chosen because it demonstrates stable charge accumulation and storage (see paragraph 6.2.1). Composite dielectrics consisted of polyimide mixed with neodymium-zirconium ternary oxide (20% by weight) and gadolinium-zirconium ternary oxide (25% by weight). These additives in optimal amounts increase the stable saturation voltage (see Figure 6.14). These dielectric samples were cured at 90°C to improve accumulated voltage stability (see Figure 6.12). The thicknesses of dielectrics were approximately 20  $\mu\text{m}$  as this thickness maximizes accumulated voltage (see Figure 6.13). Dielectrics were spin coated on stainless steel substrates with a diameter equal to the source diameter (50 mm). The battery model was assembled by pressing the source, dielectric, and collector together in a Teflon clamp.

The electrical properties of the above described battery model with charged dielectric were tested with the experimental scheme shown in Figure 6.15. As can be seen from this Figure, the source in the battery was grounded and ground current was measured using a Keithley Electrometer K6514. The collector was grounded using a switch “S”. When the switch was closed, current through the load was absent. When the switch was open, current went through the load resistor, and could be measured using the electrometer. Current from the collector through the load resistor ( $I_{load}$ ) was measured simultaneously with the current from ground to the source ( $I_{grd}$ ). Measurements were done in vacuum to minimize leakage through ionizing air at contacts.

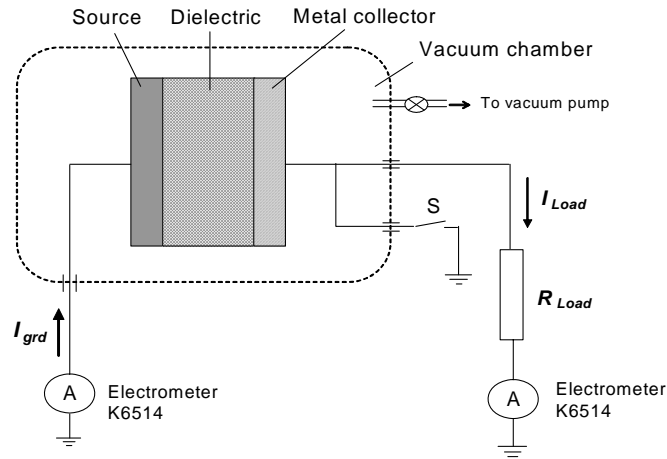


Figure 6.15. Scheme of electrical connections of the testing setup

## 6.5. TESTING THE BATTERY MODEL AND MODELING THE CHARGING PROCESS

With the switch “S” closed, the battery model was connected to measurement electronics, the residual pressure in the vacuum chamber was reduced below  $10^{-2}$  Torr and measurement initiated with the switch being closed. The behaviors of  $I_{grd}$  and  $I_{load}$  with time were the same in general for the various dielectrics used. Experimentally measured dependencies of  $I_{grd}$  and  $I_{load}$  with time for the models using tritium sources ( $A=500$  mCi) and composite dielectric (polyimide with 20%Nd<sub>2</sub>Zr<sub>2</sub>O<sub>7</sub>) are given in Figure 6.16.

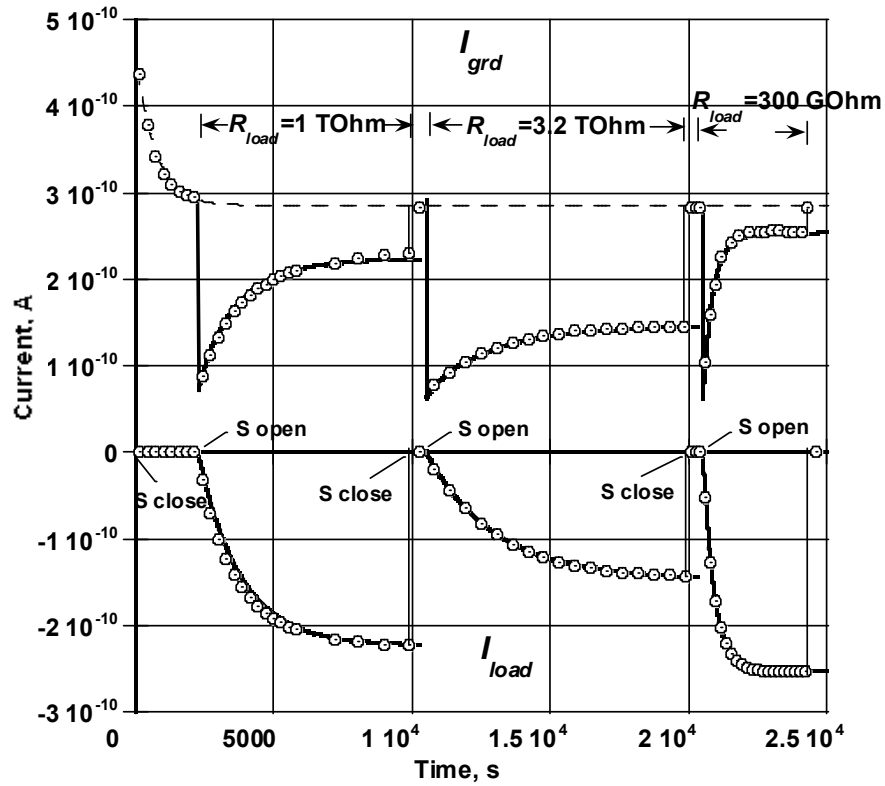


Figure 6.16. The experimentally measured dependencies  $I_{load}$  and  $I_{grd}$  with time (points) and approximation data by calculation (curves, see text for details). The results are for the battery model using tritium sources with  $A=500$  mCi and composite dielectric, polyimide with 20%Nd<sub>2</sub>Zr<sub>2</sub>O<sub>7</sub>

As can be seen in Figure 6.16, initially  $I_{load}$  was zero (collector is grounded), and  $I_{grd}$  decreased with time to a steady state. This steady state can be explained by the equilibrium between the rate of charge accumulation in the dielectric and leakage current caused by electric field of accumulated charge.  $I_{grd}$  usually decreases for 30-40 minutes. After that, a load resistor  $R_{load}$  was connected to the collector and the switch was opened. The  $I_{grd}$  dropped and then increased. Simultaneously  $I_{load}$  increased (in absolute value) until both currents reached steady state levels equal in absolute value but opposite sign. When the collector was grounded again,  $I_{load}$  dropped to zero and  $I_{grd}$  increased rapidly to the previous steady state level. This condition was reproducible with switch closing and opening but the time to reach

the steady state and the value of the steady state saturation voltage level depended critically on  $R_{load}$ .

For analysis of these changes, we will use the model and equivalent scheme shown in Figures 6.2 and 6.3 (see paragraph 6.1).

Consider the changes in  $I_{grd}$  and  $I_{load}$  with time when the switch is closed. In this case observe Figure 6.3,  $I_{load}=0$  and

$$I_{grd}(t) = I_{Ch} \cdot \eta(U_1(t)) - \frac{U_1(t)}{R_1} \quad (6.11)$$

where  $U_1(t)$  is the voltage on the  $C_{int}$ .  $U_1(t)$  can then be expressed as

$$\frac{dU_1(t)}{dt} + \frac{U_1(t) \cdot (R_1 + R_2)}{C_{int} \cdot R_1 \cdot R_2} = \frac{I_{Ch} \cdot \eta(U_1(t))}{C_{int}} \quad (6.12)$$

where  $\eta(U)$  is a function accounting for the electrostatic repulsion of beta particles from the charged region. This function estimates that part of the beta spectrum has energy less than  $q_e \cdot U$  (see paragraph 3.2.3). At low voltages this factor is not significant. For instance, as  $U$  goes from 0 to 1000V,  $\eta(U)$  changes from 1 to 0.91. Ignoring  $\eta(U)$ , the solution of Equation (6.12) for  $U_1$  is

$$U_1(t) = I_{Ch} \cdot y \cdot R_1 \cdot \left[ 1 - \exp\left(-\frac{t}{y \cdot \tau_{int}}\right) \right] \quad (6.13)$$

where  $y = \frac{R_2}{R_1 + R_2}$ , and  $\tau_{int} = C_{int} \cdot R_1$ .

$I_{grd}$  then is

$$I_{grd}(t) = I_{Ch} - \frac{I_{Ch} \cdot y \cdot R_1 \cdot \left[ 1 - \exp\left(-\frac{t}{y \cdot \tau_{int}}\right) \right]}{R_1} = I_{Ch} \cdot \left[ 1 - y \cdot \left( 1 - \exp\left(-\frac{t}{y \cdot \tau_{int}}\right) \right) \right] \quad (6.14)$$

A comparison of experimental data and calculations by this equation (dash curve) is shown in Figure 6.16. The comparison between experimental and calculated data is close. Fitting parameters  $I_{Ch}$ ,  $R_l$  and  $y$  for the battery model using a 500 mCi tritium source and composite dielectric of polyimide-20%Nd<sub>2</sub>Zr<sub>2</sub>O<sub>7</sub> are given in Table 6.4. The value of  $C_{int}$  was 670 pF.

Consider the change in  $I_{grd}$  and  $I_{load}$  with time when the switch is open. In this case

$$\frac{dU_1(t)}{dt} + \frac{U_1(t)}{C_{int} \cdot R_1} + \frac{U_1(t) - U_2(t)}{C_{int} \cdot R_2} = \frac{I_{Ch} \cdot \eta(U_1(t))}{C_{int}} \quad (6.15)$$

$$\frac{dU_2(t)}{dt} + \frac{U_2(t)}{C_{ext} \cdot R_{load}} = \frac{U_1(t) - U_2(t)}{C_{ext} \cdot R_2} \quad (6.16)$$

$$I_{grd}(t) = I_{Ch} \cdot \eta(U_1(t)) - \frac{U_1(t)}{R_1} - C_{ext} \frac{dU_2(t)}{dt} \quad (6.17)$$

$$I_{Load} = \frac{U_2(t)}{R_{Load}} \quad (6.18)$$

where  $U_2(t)$  is the voltage on the external capacitor and on the load.

The solution of this system of differential equation was found numerically using Mathcad software. Dependencies of  $I_{grd}$  and  $I_{load}$  are plotted in Figure 6.16 with time. The comparison between the dependencies and the experimental data was favorable. The value of  $C_{ext}$  = 1.3 nF was measured directly.  $C_{int}$  depends on the different load resistors although this was not expected in the model. For the predicted steady state calculations, these capacitances are irrelevant.

**Table 6.4. Fitting parameters for model equations for 0.5 Ci tritium source and composite dielectric PI-20%Nd<sub>2</sub>Zr<sub>2</sub>O<sub>7</sub>**

Type of dependence	$R_{load}$ , TOhm	$I_{Ch}$ , pA	$R_l$ , TOhm	$y$
$I_{grd}=f(t)$ at the grounded collector	0	487	2.1	0.38
$I_{grd}=f(t)$ and $I_{load}=f(t)$ at different load resistors	1	487	2.1	0.38
	3.2	490	2.1	0.38
	0.3	470	2.1	0.39
	0.1	470	2.1	0.38
	0.015	460	2.1	0.40
$U_{load}=f(R_{load})$ (at saturation)	0.001-10	460	2.3	0.39

Using these equations, it is possible to determine the  $I$ - $V$  and  $P$ - $V$  characteristics of the battery with charged dielectric. We let  $t$  go to infinity at steady state. In this case, the derivative  $dU/dt$  is equal to zero. Then Equations (6.15) and (6.16) can be rewritten as:

$$\frac{U_1}{R_1} + \frac{U_1 - U_2}{R_2} = I_{Ch} \cdot \eta(U_1) \quad (6.19)$$

$$\frac{U_2}{R_{load}} = \frac{U_1 - U_2}{R_2} \quad (6.20)$$

where  $U_1$  and  $U_2$  are voltages at steady state.

From Equation (6.19), (6.20) follow

$$U_1 = U_2 \cdot R_{load} \cdot \left( R_1 \cdot \frac{y}{1-y} + R_{load} \right)^{-1} \quad (6.21)$$

$$U_2 = \frac{I_{ch} \cdot \eta(U_1) \cdot R_1 \cdot R_{load}}{R_1 \cdot (1 - y)^{-1} + R_{load}} \quad (6.22)$$

$$I_{load} = \frac{I_{ch} \cdot \eta(U_1) \cdot R_1}{R_1 \cdot (1 - y)^{-1} + R_{load}} \quad (6.23)$$

The absolute value of the load current and useful electrical power  $P_{load}$  from voltage are:

$$|I_{load}| = \frac{|U_2|}{R_{load}} \quad (6.24)$$

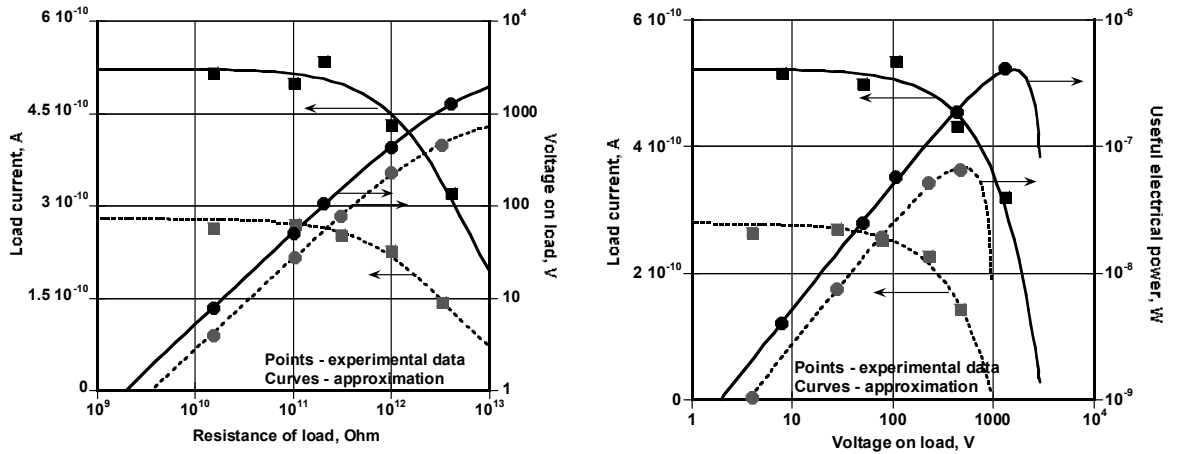
$$P_{load} = \frac{U_2^2}{R_{load}} \quad (6.25)$$

Figure 6.17 shows the  $I$ - $V$  and  $P$ - $V$  characteristics from experimental measurements (points) and approximation by Equations (6.22)-(6.25) (curves) ignoring  $\eta(U)$ . The data represents two tritium battery models with charged dielectric. The first tritium battery model had a tritium source with  $A=1$  Ci and  $A_s=0.06$  Ci/cm<sup>2</sup> and a composite dielectric with polyimide and 25%Gd<sub>2</sub>Zr<sub>2</sub>O<sub>7</sub> (solid curve). The second tritium battery model had a tritium source with  $A=0.5$  Ci and  $A_s=0.03$  Ci/cm<sup>2</sup> and a composite dielectric with polyimide and 20%Nd<sub>2</sub>Zr<sub>2</sub>O<sub>7</sub> (dashed curve). The experimental and calculated results match well. The best fitting parameters for the battery model with  $A=0.5$  Ci and composite dielectric polyimide-20%Nd<sub>2</sub>Zr<sub>2</sub>O<sub>7</sub> are represented in Table 6.4. The best fit for the battery model with 1 Ci tritium and composite dielectric polyimide-25%Gd<sub>2</sub>Zr<sub>2</sub>O<sub>7</sub> was  $I_{ch}=670$  pA,  $R_I=6.5$  TOhm, and  $y=0.22$ .

As can be seen in Table 6.4 from the approximation of the  $I$ - $V$  characteristic, the values  $I_{ch}$ ,  $R_I$ , and  $y$  are very close to those received from the approximation of dependencies of  $I_{grd}$  with time when the switch was closed. In addition, the same was observed with the battery model, with  $A=0.5$  Ci and composite dielectric polyimide-20%Nd<sub>2</sub>Zr<sub>2</sub>O<sub>7</sub>, from the approximation of dependencies of  $I_{grd}$  and  $I_{load}$  with time when the switch was open (Figure 6.3). The same agreement was noted in other battery models and was taken as evidence that the above model was suitable for describing the tritium nuclear battery with charged dielectric.



As can be seen from represented values  $R_l$  and  $y$ ,  $R_2$  is less than  $R_l$ . It was expected that  $R_2$  would be greater than  $R_l$  because the distance from the charged domain to the rear electrode was farther than from the charged domain to the source (front electrode). It was observed that the charge density in charged domain decreased from the surface toward the inner volume direction (see Figures 6.9 and 6.10). Beta particles penetrated through the charged surface to the dielectric volume, and thermolized in it. Due to an intensely charged domain, the thermolized electrons move to the rear electrode and cannot move back through the charged domain due to its much larger negative charge. As a result  $R_2$  is less than  $R_l$  and  $y < 0.5$ .



a) Voltage (square) and load current (circles) versus resistance of load.

Approximation by Eq. (6.22) and (6.23)

b) Current-voltage (square) and power-voltage (circles) characteristics.

Approximation by Eq. (6.24) and (6.25)

Figure 6.17. Electrical load characteristics of tritium batteries with charged dielectric with 1 Ci ( $A_s = 0.06 \text{ Ci/cm}^2$ ) and polyimide-25%Gd<sub>2</sub>Zr<sub>2</sub>O<sub>7</sub> (solid) and 0.5 Ci ( $A_s = 0.03 \text{ Ci/cm}^2$ ) and polyimide-20%Nd<sub>2</sub>Zr<sub>2</sub>O<sub>7</sub> (dash)

The measured data of useful electrical power permits calculation of the efficiency of this battery model. In the best case, useful electrical power was  $4 \cdot 10^{-7} \text{ W}$  with efficiency of 1.2% as calculated from Equation (6.26).

$$\xi = \frac{P_{el,max}}{A \cdot \varepsilon_{avg}} \cdot 100\% \quad (6.26)$$

## 6.6. PREDICTED CALCULATIONS

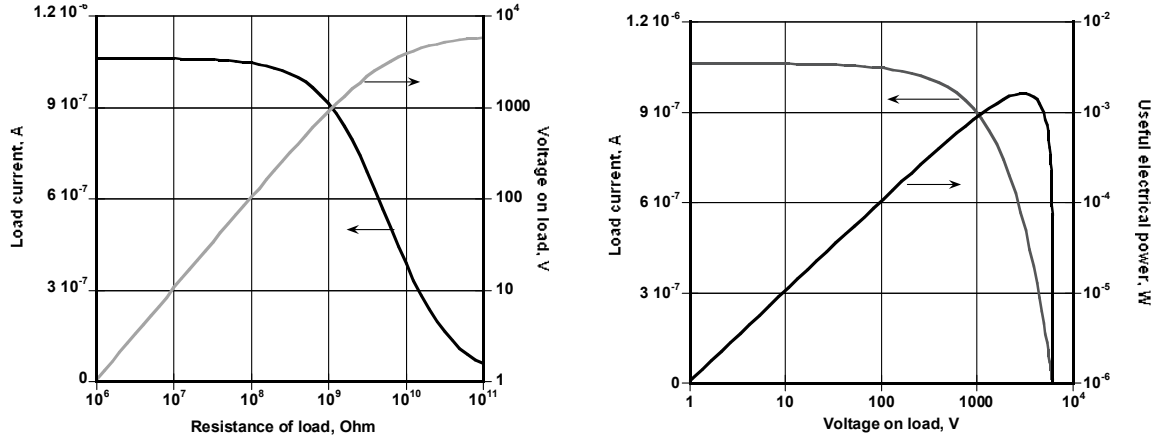
The experimental battery with charged dielectric using 1 Ci tritium delivers several hundred nanowatts of useful power. To increase the electrical power of this battery, One can increase the surface activity and total activity of radioactive source as well as design a  $4\pi$  source. One is able to predict the electrical load characteristics of a tritium battery with charged dielectric with total activity of 1000 Ci and surface activity of  $100 \text{ mCi/cm}^2$ . Fabrication of scandium tritide sources using 300 nm Sc will produce this surface activity. In this case, the beta particle current density will be approximately  $140 \text{ pA/cm}^2$  (Equation (4.6)). The total area of the sources with 1000 Ci tritium and surface activity  $100 \text{ mCi/cm}^2$  is one  $\text{m}^2$ . The 130 10 cm diameter substrates provides a total active area of one  $\text{m}^2$ .

Suppose that the resistance  $R_l$  is inversely proportional to area  $R_l = r_l / S$ , where  $r_l$  is coefficient. Therefore, using Equation (4.4) and (6.22), the following is assumed:

$$U_2 = q_e \cdot \eta_s \cdot A_s \cdot S \cdot \frac{r_l \cdot R_{load}}{r_l \cdot (1 - y)^{-1} + R_{load}} \cdot \eta(U_1) \quad (6.27)$$

$r_l$  is possible to estimate from the value of  $R_l$  determined experimentally. In the best case  $R_l = 6.5 \text{ TOhm}$  for the outer diameter of battery model  $5 \text{ cm}^2$  (see paragraph 6.5). Given the area of this dielectric,  $r_l = R_l \cdot S = 1.2 \cdot 10^{10} \text{ Ohm} \cdot \text{m}^2$ , and this value is used for predicted calculations.

Results of electrical load characteristics calculations using Equations (6.27), (6.21), (6.22) for a 1000 Ci tritium battery with charged dielectric are given in Figure 6.18. As can be seen from these plots, open circuit voltage is more than 6 kV, and short circuit current is more than  $1 \text{ } \mu\text{A}$ . This battery would produce  $> 1$  milliwatt of electric power on an optimal load. The efficiency of this battery calculated by Equation (6.26) is approximately 4.7%. For example, a  $4\pi$  source produced by sandwiching the conductive tritide between dielectrics increases efficiency to 9.4%.



a) Dependencies voltage and load current versus resistance of load

b) current-voltage and power-voltage characteristics

Figure 6.18. Calculated load electrical characteristics of tritium battery with charged dielectric with tritium sources total activity 1000 Ci and polyimide-25%Gd<sub>2</sub>Zr<sub>2</sub>O<sub>7</sub> composite.

The gravimetric energy density,  $E_G$  (Wh/kg) of the 1 kCi battery with 15 micron composite dielectric polyimide-25%Gd<sub>2</sub>Zr<sub>2</sub>O<sub>7</sub> can be estimated:

$$E_G = \frac{P_{el}}{m} \cdot \int_0^{T_{1/2}} e^{-\frac{\ln 2 \cdot t}{T_{1/2}}} dt = \frac{A \cdot \epsilon_{av} \cdot \xi}{m} \cdot \int_0^{T_{1/2}} e^{-\frac{\ln 2 \cdot t}{T_{1/2}}} dt \quad (6.28)$$

where the  $m$  is mass of tritide (1 g) plus the mass of dielectric (29 g),  $T_{1/2}$  is half-life of the isotope (hours).

Assuming a power supply life equal to the half-life of the radioisotope gives  $E_G=3700$  Wh/kg. A conservative calculation might include the metal collectors, contacts, and package to increase total device mass four-fold, reducing  $E_G$  to 900 Wh/kg. State-of-the-art lithium ion batteries reach 300 Wh/kg although commercial batteries are substantially less.<sup>22</sup>

## 6.7. CONCLUSION

This experimental work has shown that tritium nuclear batteries with solid dielectric function well even when the dielectric is much thicker than the penetration depth of the ejected beta particles. The electronic charge accumulated in the thick dielectric is efficiently transferred to the metal collector with adequate volume resistivity of dielectric. The load electrical characteristics of tritium nuclear battery with charged dielectric using 0.5-1 Ci tritium sources and different dielectric layers have been built and some of them have been described above. To date it was determined that composite dielectric polyimide loaded with 25%Gd<sub>2</sub>Zr<sub>2</sub>O<sub>7</sub> with thickness 15-20 micron is more suitable for use in this battery. Equations were derived to describe the electrical load characteristics of the tritium nuclear battery with charged dielectric and these equations compare favorably with the experimental data. Predicted electrical properties using 1000 Ci tritium sources were provided. The device should be able to produce 1  $\mu$ A of short circuit current, approximately 6 kV of open circuit voltage, and up to 1 mW of electrical power with an overall efficiency approaching 4%. The gravimetric energy density of this battery would be several times higher than for the best chemical batteries. The fabrication and testing of tritium nuclear batteries with charged dielectric has a direct practical application for high-voltage, long-life, and extreme environment conditions such as space and deep sea sensor/transmitters.

## REFERENCES

- <sup>1</sup> [http://www2.dupont.com/Kapton/en\\_US/assets/downloads/pdf/summaryofprop.pdf](http://www2.dupont.com/Kapton/en_US/assets/downloads/pdf/summaryofprop.pdf)
- <sup>2</sup> L. N. de Oliveira, and B. Gross, "Space-charge-limited currents in electron-irradiated dielectrics," *Journal of Applied Physics* **46** (7), 3132 (1975).
- <sup>3</sup> F. C. Aris, P. M. Davies, and T. J. Lewis, "Electron-beam-induced conduction in dielectrics," *Journal Physics C: Solid State Physics* **9**, 797 (1976).
- <sup>4</sup> D. M. Taylor, "Electron-beam charging of polyethylene terephthalate films," *Journal Physics D: Applied Physics* **9**, 2269 (1976).
- <sup>5</sup> L. M. Beckley, T. J. Lewis, and D. M. Taylor, "Electron-beam-induced conduction in polyethylene terephthalate films," *Journal Physics D: Applied Physics* **9**, 1355 (1976).
- <sup>6</sup> B. Gross, J. Dow, and S. V. Nablo, "Charge buildup in electron-irradiated dielectrics," *Journal Applied Physics* **44**, 2459 (1973).
- <sup>7</sup> A. Rose, "Space-Charge-Limited Current in Solids," *Physical Review* **97** (6), 1538 (1957).
- <sup>8</sup> C. Perrin, V. Griseri, C. Inguibert, and C. Laurent, "Analysis of internal charge distribution in electron irradiated polyethylene and polyimide films using a new experimental method," *Journal of Physics D: Applied Physics* **41**, 205417 (2008).
- <sup>9</sup> C. Perrin, V. Griseri, and C. Laurent, "Measurement of Internal Charge Distribution in Dielectrics using the Pulsed Electro-acoustic Method in non Contact Mode," *IEEE Transactions on Dielectrics Electrical Insulation* **15** (4), 958 (2008).
- <sup>10</sup> V. Griseri, C. Perrin, K. Fukunaga et al., "Space-Charge Detection and Behavior Analysis in Electron Irradiated Polymers," *IEEE Transactions on Plasma Science* **34** (5), 2185 (2006).
- <sup>11</sup> G. M. Sessler, "Charge Dynamics in Irradiated Polymers," *IEEE Transactions on Electrical Insulation* **27** (5), 961 (1992).
- <sup>12</sup> B. Gross, "Radiation-Induced Charge Storage and Polarization Effects," *Topics in Applied Physics* **33**, 217 (1979).
- <sup>13</sup> D. Drouin, A.R.Couture, D.Joly et al., "CASINO v.2.42 – a fast and easy-to-use modeling tool for scanning electron microscopy and microanalysis users," *Scanning* **29**, 92 (2007).
- <sup>14</sup> A. Morozov, T. Heindl, C. Skrobol, J. Wieser, R. Krucken, and A. Ulrich, "Transmission of ~10 keV electron beams through thin ceramic foils: Measurements and Monte Carlo simulations of electron energy distribution functions," *The European Physical Journal D*, **48**, 383 (2008).
- <sup>15</sup> <http://www.nist.gov/physlab/data/star/index.cfm>
- <sup>16</sup> J.A. Glendhill, "The range–energy relation for 0.1-600 keV electrons," *Journal of physics A: Math., Nucl. Gen.* **6**, 1420 (1973).
- <sup>17</sup> L. Katz, A.S. Penfold, "Range-Energy Relations for Electrons and the Determination of Beta-Ray End-Point Energies by Absorption," *Reviews of Modern Physics* **24**, 28 (1952).
- <sup>18</sup> [http://www.boedeker.com/polyst\\_p.htm](http://www.boedeker.com/polyst_p.htm)
- <sup>19</sup> A. R. Frederickson, and S. Woolf, "Electric Field in keV Electron Irradiated Polymers," *IEEE Transactions on Nuclear Science* **NS-29** (6), 2004 (1982).
- <sup>20</sup> D. Linder, and T. B. Reddy, "Handbook of Batteries," 3<sup>rd</sup> ed., McGraw-Hill (2002).
- <sup>21</sup> *Journal Material Research* **19**, 1575 (2004).
- <sup>22</sup> <http://www.batteryuniversity.com/partone-3.htm>

- <sup>23</sup> N. H.Ahmed, and N. N.Srinivas, "Review of Space Charge Measurements in Dielectric," *IEEE Transactions on Dielectric and Electrical Insulation* **4** (5), 644 (1997).
- <sup>24</sup> M. A. Noras, "Charge Detection Methods for Dielectrics – Overview," *Trek Application Note* **1** (Nov 2005).
- <sup>25</sup> K. Fukunaga, "Progress and Prospects in PEA Space Charge Measurement Techniques," *IEEE Electrical Insulation Magazine* **26** (2008).
- <sup>26</sup> Y.Li, M.Aihara, et al., "Space charge measurement in thick dielectric materials by pulsed electroacoustic method," *Review Scientific Instruments* **66**, 3909 (1995).
- <sup>27</sup> Li Y., Yasuda M., and Takada T., "Pulsed Electroacoustic Method Measurement of Charge for Accumulation in Solid Dielectrics," *IEEE Transactions on Dielectric and Electrical Insulation* **1**, 2, 188 (1994).
- <sup>28</sup> Maeno T., Futami T., Kushibe H., Takada T. , et al., "Measurement of Spatial Charge Distribution in Thick Dielectrics Using the Pulsed Electroacoustic Method," *IEEE transactions on Electrical Insulation* **23**, 443 (1988).
- <sup>29</sup> Kushibe H., Maeno T., and Takada T., "Measurement of Accumulated Charge Inside Dielectric by Pulsed Electric Forced Techniques," *Trans. IEE Japan*, **A-106**, 118 (1986).

## CHAPTER 7

### APPLICATIONS OF DIRECT CHARGE NUCLEAR BATTERIES

#### 7.1 LOAD CHARACTERISTICS AND POSSIBLE DIRECT CHARGE NUCLEAR BATTERY APPLICATIONS

The present dissertation research describes progress in optimizing direct charge nuclear batteries using tritium and Pm-147. Load characteristics are summarized in Table 7.1.

**Table 7.1. Activity and load characteristics for different direct charge nuclear batteries**

Isotope and dielectric type	Activity	Optimal load resistor	Voltage on optimal load	Power on optimal load	Efficiency, %
Tritium, vacuum, experimental	108 Ci	35 GOhm	2.6 kV	200 $\mu$ W	5.5
Pm-147, vacuum, experimental	2.6 Ci	8300 GOhm	35 kV	140 $\mu$ W	14
Tritium, solid, experimental	1 Ci	4000 GOhm	1.3 kV	0.4 $\mu$ W	1.2
Tritium, solid, predicted	1000 Ci	5.5 GOhm	2.8 kV	1600 $\mu$ W	4.7

The nuclear battery can produce working voltage up to several dozen kilovolts on an active load of gigohm to several terohm, as summarized in the Table 7.1. More importantly, the operating voltage can be engineered over a wide range for any given load. Given the advantages of the nuclear battery and its high efficiency and energy density, a number of advantages in remote and hostile environments are suggested:

- Use of the battery on lower resistance loads (kilohm-gigohm) at lower operating voltages (10-100V) is certainly possible although this does sacrifice power and efficiency.

However, their application in hostile environments (space and deep sea) does not affect the stability of the power supply or fuel burn rate;

- Use of the battery as a high-impedance voltage down-converter for continuous secondary battery recharge and leakage inhibition (for example a reversible Marx-generator<sup>1</sup>);
- Use of the battery to accumulate energy on an external capacitor over long periods (seconds to minutes) for fast (millisecond) discharge of the accumulated energy such as a spark or even a fielded sensor transmission pulse;
- Use of the direct charge nuclear battery to produce useful electrostatic fields.

## 7.2 AUTONOMOUS ALPHA DIRECT CHARGE NUCLEAR BATTERY (ALPHA-BETA CELL)

In the Anno work<sup>2</sup> as well as in previous experiments with an alpha isotope powered direct charge battery it was shown that the successful operation of the alpha direct charge nuclear battery required an external source of negative voltage. This negative voltage is needed to suppress low-energy secondary electron current from the alpha source. Copious secondary electrons come from alpha particles emitted in the alpha source. Therefore such a cell is not really autonomous. It was shown that a beta direct charge battery can provide the needed voltage to effectively up-convert electrical potential. It was suggested that the same battery be utilized as a source of grid voltage for the alpha direct charge nuclear battery. The same principle can be applied to the myriad of devices requiring high voltage, low current bias, such as sensitive nuclear detectors (including Geiger-Muller tubes), PMTs, and electroluminescent display backlights.

A schematic of the experiment demonstrating the operation of the alpha direct charge nuclear battery with a secondary electron suppression mesh powered by a beta direct charge nuclear battery (alpha-beta battery) is presented in Figure 7.1.



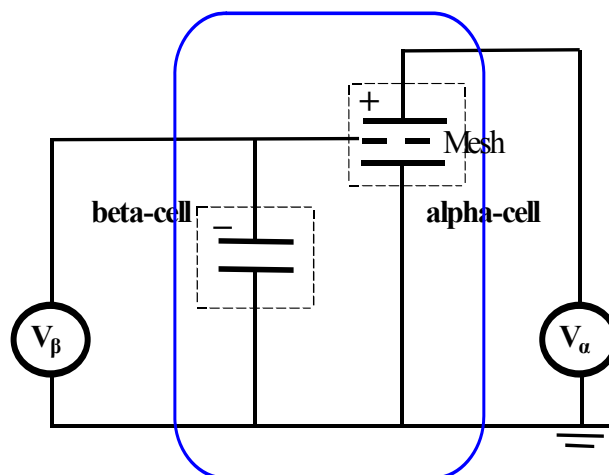


Figure 7.1. Schematic of successful connection of a beta direct charge nuclear battery to the secondary electron suppression mesh of an alpha direct charge nuclear battery

Two series of experiments with the alpha-beta battery were done. In the first series, an alpha direct charge nuclear battery was built using a Pu-238 source (see Figure 7.2) with an activity of 300 mCi. The picture of this battery is shown in Figure 7.3, and the scheme is shown in Figure 7.4.



Figure 7.2. Picture of Pu-238 alpha-source



Figure 7.3. Picture of Pu-238 direct charge battery

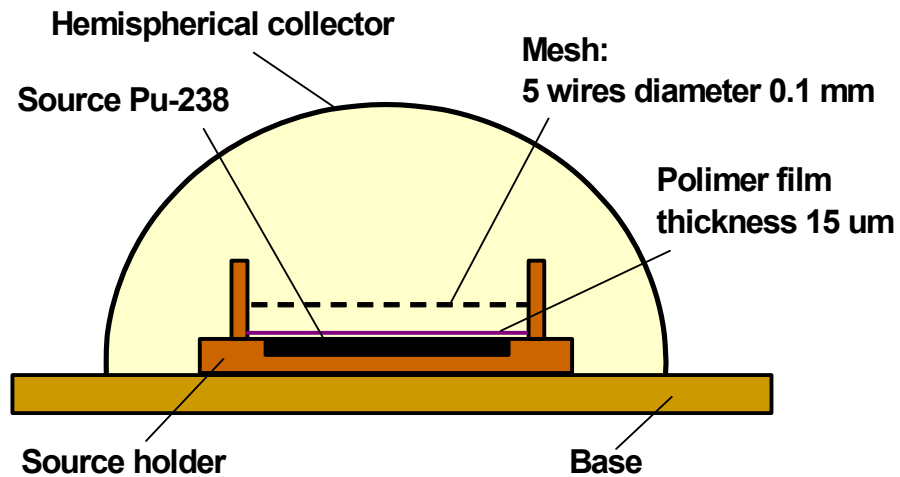


Figure 7.4. Scheme of Pu-238 direct charge nuclear battery

The negative voltage on the mesh was applied from the tritium direct charge nuclear battery described in Chapter 4. The behaviors of the voltage on the tritium battery collector, (connected to the mesh of the alpha battery) and on the collector of alpha battery are shown in Figure 7.5.

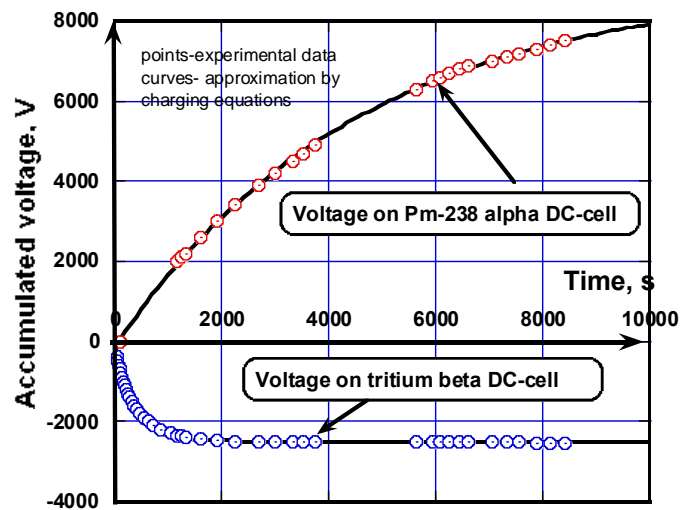


Figure 7.5. Charging of plutonium-238 DCNB operated by tritium DCNB

As can be seen in Figure 7.5, the voltage produced by the tritium battery increases until it reaches the saturation coincident of the alpha charging cell.

In the second series of experiments, the alpha-beta battery was fabricated on the base of one Po-210 source with activity 5 mCi (alpha battery) and four Pm-147 sources with total activity 110 mCi (beta battery). The overview of the alpha-beta battery is shown in Figure 7.6, and the experimental schematic is presented in Figure 7.7.

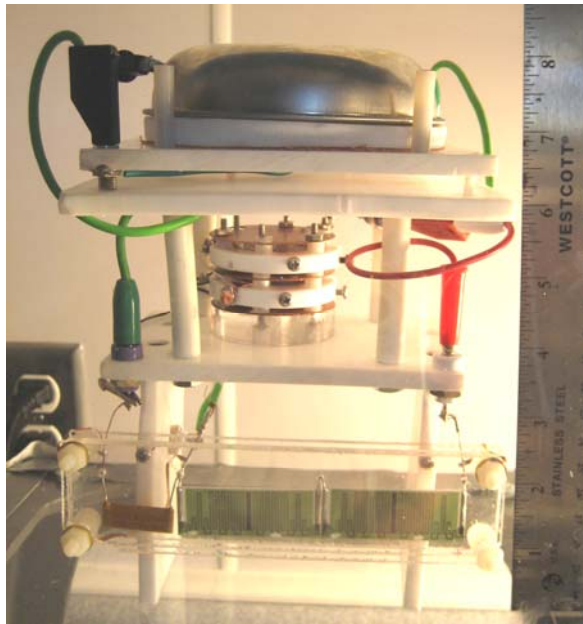


Figure 7.6. Picture of Po-Pm alpha-beta cell with voltage divider (Po-210 source with activity 5 mCi, and four Pm-147 sources with total activity 110 mCi)

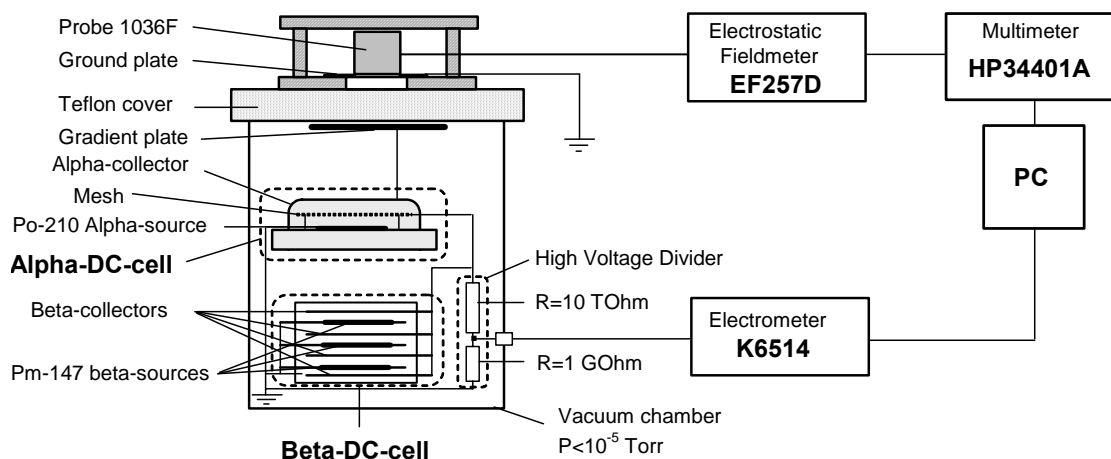
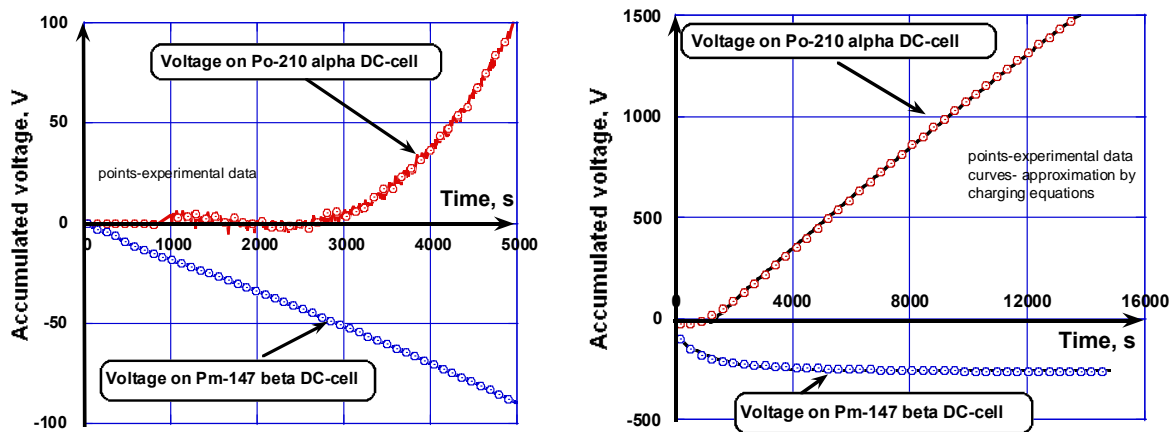


Figure 7.7. The schematic of alpha – beta direct charge experiment for voltage measurements of the beta cell with a high voltage divider

The collector of the promethium beta battery was connected to the mesh of the polonium alpha battery for supplying the mesh bias, and voltage on the collectors of the beta and alpha battery were measured. These are presented in Figure 7.8.



a) At the beginning of charging

b) Prolonged time

Figure 7.8. Dependencies accumulated voltage in Po-Pm alpha-beta battery with time (Po-210 source with 5mCi activity, and four Pm-147 sources with total activity 110 mCi, bias on mesh of alpha battery is provided by the beta battery)

These two series of experiments with tritium-Pu-238 and Pm-147–Po-210 alpha-beta batteries demonstrate how direct charge beta batteries are used as a voltage source on the mesh of direct charge alpha batteries, and indirectly as an electrostatic bias for any low current purpose.

### 7.3. EXPERIMENTS WITH FLASH LAMP

As was suggested, another way of constructively using the direct charge nuclear battery is through the accumulation of energy on an external capacitor during a relatively long time and using this energy in short pulses. As a demonstration of this application experiments with neon lamps were carried out. A neon lamp was connected in parallel to a capacitor on which the electrical energy accumulated from tritium direct charge battery. The capacitor was chosen to accommodate at least 80 V, which is the voltage at which the neon lamp flashed. Every 10 seconds, at the charging current which was expected to accumulate on the capacitor, energy flashed the lamp. Approximately 0.1 mJ at 80 V was deemed adequate to flash the neon lamp. 0.1 mJ on the capacitor at 80 V is around 30 nF. The charging time of a 24-source tritium direct charge nuclear battery described in Chapter 4 (148 nA) should be around 16 second. Based on these considerations, capacitors with 10-30 nF were chosen for this experiment.

The scheme of connecting the neon lamp to the capacitor charged by the tritium direct charge nuclear battery is shown in Figure 7.9.

The experiments were conducted with tritium direct charge nuclear battery as described in Chapter 4 with a current of 90 and 148 nA. When the voltage on the capacitor reached the discharge voltage of the neon lamp (approximately 80 Volts), the neon lamp flashed and voltage dropped down. The process repeated indefinitely. The capacitance of the capacitor, frequency of the flash, and the brightness of the flash are shown in Table 7.2.

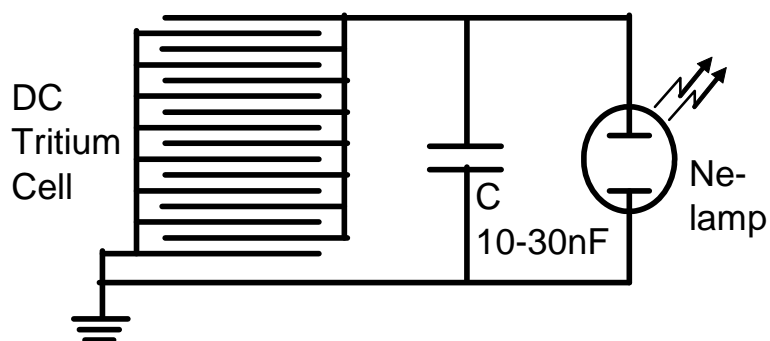


Figure 7.9. The scheme of connecting the neon lamp to tritium direct charge nuclear battery

**Table 7.2. The capacitance of capacitor, frequency of flash and characteristic of brightness of flash in experiments with neon lamp**

Type of tritium battery	Charging current	Capacitance of capacitor	Frequency of flash	Characteristic of flash brightness
16 PitU-100 sources; vacuum; PI covered SS collector; $A=72$ Ci	90 nA	10 nF	Each 5 second	Seen in twilight from several meters
24 PitU-100 sources; vacuum; PI covered SS collector; $A=108$ Ci	148 nA	20 nF	Each 6 second	Brighter than previous case

The dependence of voltage on the capacitor with time is shown in Figure 7.10. As can be seen from this Figure, the voltage increased to 80 V and then dropped back to 65 V. With each light flash the process repeated. The first experiment continued all night and the flashes were observed in the morning with the same frequency as in evening.

This experiment demonstrated the possibility of using the direct charge nuclear battery as a power supply for pulsed applications.

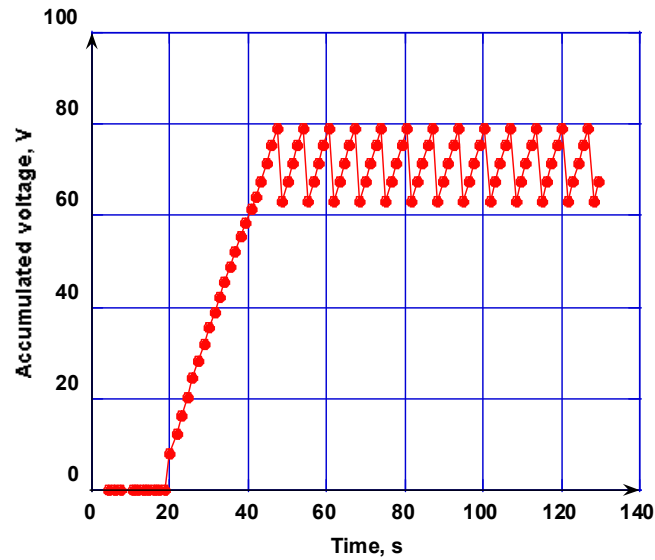


Figure 7.10. Voltage on capacitor charged by a tritium direct charge nuclear battery and connected to a neon lamp

#### 7.4 DIRECT CHARGE NUCLEAR BATTERY AS A POWER SUPPLIER FOR ELECTROSTATIC MOTOR AND PHOTOMULTIPLIER

Two promising applications of the direct charge nuclear battery include powering electrostatic motors and self-bias of photomultiplier tubes.

In an electrostatic motor, the motion is created as a result of electrostatic forces acting between electric charges. According to O.D. Jefimenko,<sup>3</sup> this type of motor requires a high voltage ( $> \text{kV}$ ) power supply at a low current (nanoampere range). As can be seen from Table 7.1, the nuclear battery with either Pm-147 or tritium with activity  $> 100$  curies can serve as such a power supply.

A power supply which produces 1-2 kilovolts is needed for the photomultiplier tube. This negative voltage is connected to the photocathode and eventually distributed on the dynode system using a high voltage divider to distribute the voltage on dynode system. The

current through the voltage divider should be at least ten times more than anode current for stable photomultiplier performance. For low light flux, anode current is in the nanoampere range. As seen in Figure 6.19, stable voltage at around 1 kV and at a current of approximately 1  $\mu$ A was produced by the tritium battery with charged solid dielectric. The application of the same power supply for PMT makes sense in autonomous light sensitive gauges.

## REFERENCES

- <sup>1</sup> N. Luo, and G. H. Miley, "Power conversion circuitry," *US Patent 7417356* (2008).
- <sup>2</sup> J. N. Anno, "A Direct-Energy Conversion Device Using Alpha Particles," *Nucl. News*, **6**, 3 (1962).
- <sup>3</sup> O. D. Jefimenko, "Electrostatic Motors," *Electret Scientific Company* (1973).



## CONCLUSIONS

This research examined experimental and theoretical developments of direct charge nuclear batteries based on radioactive decay of tritium and promethium-147. The work involved the construction, testing and analysis of several direct charge nuclear battery systems. In addition, the theoretical basis for assessing the performance and efficiencies of these systems was developed and compared with the experimental results. Along with direct charge nuclear batteries using a vacuum dielectric, a tritium battery incorporating a solid dielectric with thickness greater than the range of tritium beta particles was designed and investigated. A phenomenological model describing this new type of nuclear battery was presented. Through experimentation, models were created to show the possible applications for nuclear batteries.

Based on research and experimentation, the following conclusions can be drawn.

1. On the basis of both literature review and theoretical considerations it was shown that the direct charge nuclear battery has the highest overall conversion efficiency in comparison with other types of nuclear batteries (direct and indirect conversion, contact potential, secondary electron emission nuclear batteries). Based both on a comparative risk analysis of properties of alpha and beta isotopes, including calculations of beta particle flux densities from available beta sources, tritium and promethium-147 were chosen as the most suitable for a direct charge nuclear battery.

2. This work theoretically predicted and experimentally confirmed the possible fabrication of direct charge nuclear batteries with a vacuum dielectric having electrical power close to the milliwatt range, and efficiency of approximately 12% using tritium and 21% using promethium-147.

Based on theoretical analysis of factors including backscattering and secondary electron emission, configuration geometry, working voltage, efficiency of sources, and interelectrode distance (which affect charge accumulation in tritium and promethium-147 direct charge batteries with vacuum dielectric) it was determined that high efficiency can be

reached taking in to consideration high efficiency ( $4\pi$ ) sources and specialized collector coatings.

A tritium direct charge battery with a vacuum dielectric, one-sided tritium sources with total activity of 108 curies, and collectors with secondary electron and backscattering suppression coatings was built and tested. It was demonstrated that while bare stainless steel collectors did not function, the model using secondary electron and backscattered electron suppression coatings had an open circuit voltage of 5300 volts, a short circuit current 148 nanoamperes, and an efficiency of 5.5%. The efficiency can be doubled for double-sided ( $4\pi$ ) sources. The experimental results agree with the theoretical estimation.

The best promethium-147 model had a cylindrical design and used a double-sided ( $4\pi$ ) source with flux efficiency over 50% and an activity of 2.6 curies. Its collector had a polyimide coating to reduce backscattering. This prototype had an open circuit voltage around 60 kilovolts, a short circuit current 6 nanoamperes, and an overall efficiency of 15%. The experimental value of efficiency also closely matched the theoretical calculations.

The theoretically predicted and experimentally confirmed efficiency of these batteries is much more than previously demonstrated in historical models of direct charge nuclear batteries (less than 3%).

3. This work suggested a new type of nuclear battery based on the effect of charge accumulation in a dielectric under beta irradiation. All beta particles are stopped in a thick solid dielectric and charge accumulates (the thickness of the dielectric is more than beta particle range). The electric field due to this space charge will create an electrical current toward the collector. If the thickness and conductivity of the dielectric are chosen properly, useful current on the collector can be developed.

A functional battery of this type was built. The battery used a tritium source (300 nanometers scandium tritide on stainless steel substrate, activity of 1 curie), dielectric (20 micron polyimide) layer and metal collector without vacuum space between layers was built and tested. This model with an activity of 1 curie produced 0.4 microwatts of electrical power on a 1 tera-ohm load with efficiency of approximately 1%.

This research provides a phenomenological model describing the interactive dependencies of sources and collector currents with time, collector current and voltage at saturation with dielectric, and load resistors. The model is consistent with experimental data. Based on this model, the scaled-up battery properties were calculated. This battery design has a tritium activity of 1000 curies and will produce over one milliwatt power with efficiency approximating 4%. The efficiency of the nuclear battery with charged dielectrics is less than that with vacuum dielectric. However, the solid-state power supply is significantly smaller and more rugged.

While studying the mechanism of charge accumulation and transfer in dielectric under tritium irradiation, calculations using Monte Carlo simulation code and experimental measurements by the pulse electro acoustic method were performed. It was determined that charge accumulated under tritium irradiation in polyimide. Because of this charge accumulation, there was a charged zone where the charge dropped from surface to 0.5 micron in 5 time and then continuously decreased to zero at depth of several microns (~5 micron). This fact was used for initial theoretical considerations of the mechanism of charge transfer under these conditions. The mechanism of current transfer through dielectric material under ionizing radiation conditions is worth additional investigation for optimization of this battery type.

4. This work experimentally demonstrated suitable applications of direct charge nuclear batteries and nuclear battery with charged dielectric. Possible applications include the production of bias voltage on electrostatic shields and high-voltage pulsed power for flash lamps or lasers. In addition, this research suggested the general direction that commercially important market development might take.

## **FUTURE WORK**

The most productive direction for future work in this field is the investigation of a nuclear battery with charged solid dielectric, and includes:

- the theoretical and experimental investigation of the charge accumulation, space charge distribution, and charge transfer in dielectric under electron beam and tritium beta irradiation;
- optimizing the chemical composition of dielectrics, including graded dielectric structures, for their ability to charge, store, and transfer charge to a collector;
- the investigation of dielectric processing;
- the investigation of radiation damage of dielectric under tritium beta irradiation;
- optimizing the thickness of dielectric for this device for maximum efficiency or engineered voltage at a given long-term load;
- the fabrication and testing of this type of battery with an activity above 1000 curies;
- demonstrating that the battery is a suitable power supply for diverse deep space or deep sea applications, including the harvesting of ionizing radiation in deep space for propulsion and communications.

## Appendix A

### MEASUREMENT OF THE ACTIVITY PM-147 SOURCE (BPm7-MU08-6 Rectangular) BY GAMMA-SPECTROMETRIC METHOD

Date of measurement: May 06, 2008.

Measurements were carried out using a gamma-spectrometer Canberra with 4" HPGe detector and a standard reference source using a comparison method. The photon energy of Pm-147 is 121.22 keV<sup>1</sup> so source Co-57 #75645-156 with photon energy 122.06 keV<sup>2</sup> was chosen as the reference line. The measurements were made by comparison of peak area counting from reference source and Pm-147 source BPm7-MU08-6 Rectangular.

At first, the measurement of the background,  $N_b$ , in the region of Pm-147 photon energy 121.22 keV was done. For reducing the statistical error, three measurements for 1800 seconds each were collected. The average value,  $N_{bavg}$ , was taken, and the number of counts per second was calculated. The error of results was taken as two standard deviations by Equation (A1).<sup>3</sup> The results of these measurements and calculations are represented in Table A. 1.

$$\Delta N_b = 2 \cdot \sqrt{\frac{\sum_{i=1}^3 (N_{bi} - N_{bavg})^2}{2}} \cdot \frac{1}{T_c} \quad (A1)$$

**Table A. 1. Results of the background measurement**

# meas., $i$	Counting time, $T_c$ , s	$N_{bi}$ , counts	$N_{bavg}$ , counts	$N_b \pm \Delta N_b$ , cps
1	1800	11600	11070	6.2±0.6
2		11100		
3		10500		

Next, counting over the full-energy peak around 121.22 keV of the Pm-147 source was done. Because of the high activity of the Pm-147, the distance between source and detector was chosen such that the dead time was less than 1%. This distance was  $226 \pm 1$  cm. The procedure of the measurements and calculation of average value  $N_s$  and error  $\Delta N_s$  were the same as for the background measurement. The pure counting rate for Pm-147 source,  $N_{Pm}$ , was calculated as the difference between the source rate,  $N_s$ , and background rate,  $N_b$ . The error of the pure counting rate  $\Delta N_{Pm}$  was calculated by Equation (A2).<sup>3</sup> The results of measurements and calculations are presented in Table A. 2.

$$\Delta N_{Pm} = \sqrt{\Delta(N_s)^2 + \Delta(N_b)^2} \quad (A2)$$

**Table A. 2. Results of the Pm-147 source measurement**

# meas., $i$	Counting time, $T_c$ , s	$N_{si}$ , counts	$N_{savg}$ , counts	$N_s \pm \Delta N_s$ , cps	$N_{Pm} \pm \Delta N_{Pm}$ , cps
1	1800	123000	122650	68.1 $\pm$ 0.6	61.9 $\pm$ 0.8
2		123000			
3		122000			

The counting of the reference source,  $N_{ref}$ , was measured at a distance of  $30.5 \pm 0.5$  cm between source and detector. This is a standard geometry for a reference source. In this case, one measurement for 54000 seconds was done, and the rate for reference source  $N_{rs}$  was calculated. The error was calculated by Equation (A3).<sup>3</sup>

$$\Delta N_r = 2 \cdot \frac{\sqrt{N_r}}{T_c} \quad (A3)$$

The pure counting rate  $N_{ref}$  was calculated as difference between reference source rate  $N_{rs}$  and background rate  $N_b$ . The error of the pure counting rate  $\Delta N_{ref}$  was calculated using Equation (A2). The results of measurement and calculations are presented in Table A. 3.

**Table A. 3. Results of the reference source measurement**

# meas.	Counting time, $T_c$ , s	$N_r$ , counts	$N_{rs} \pm \Delta N_{rs}$ , cps	$N_{ref} \pm \Delta N_{ref}$ , cps
1	54000	523000	$9.69 \pm 0.02$	$3.5 \pm 0.6$

Gamma flux,  $F_0$ , of the standard reference source at 122.06 keV (Co-57) according to the manufacturer certificate was equal  $6013 \text{ s}^{-1}$  on the 07/01/07. Taking into account the decay of Co-57 from the certificate date to our measurement date (05/06/2008)  $\Delta t$ , the present expected flux,  $F$ , was calculated by Equation (A4).

$$F = F_0 \cdot e^{-\frac{\ln(2) \cdot \Delta t}{T_{1/2}}} \quad (\text{A4})$$

where  $\Delta t = 308$  days and  $T_{1/2} = 271.74$  days.<sup>2</sup>

Gamma flux on 05/06/08 was  $F = 2743 \text{ s}^{-1}$ .

Because the reference source and Pm-147 source were measured at different distances from the detector, we needed to recalculate the Pm-147 source at 30.5 cm by Equation (A5).

$$N_{30.5} = N_{Pm} \cdot \left( \frac{226}{30.5} \right)^2 \cdot \exp(\mu \cdot \rho \cdot (226 - 30.5)) = 3520 \text{ s}^{-1} \quad (\text{A5})$$

where  $\mu = 0.1425 \text{ cm}^2/\text{g}$  is the mass attenuation coefficient of air for photons of 121 keV,<sup>4</sup> and  $\rho = 0.00121 \text{ g/cm}^3$  is the air density.<sup>5</sup>

The activity of Pm-147 source BPm7-MU08-6 Rectangular on the 05/06/08 can be calculated by Equation (A6).

$$A = \frac{N_{Pm30.5}}{N_{ref}} \cdot F \cdot \frac{1}{\gamma \cdot 3.7 \cdot 10^{10}} = 2.6 \text{ Ci} \quad (\text{A6})$$

where  $\gamma = 0.0000285$  is the yield of 121.22 keV gamma rays for Pm-147.<sup>2</sup>

The error of activity value was calculated by Equation (A7).

$$\Delta A = A \cdot \sqrt{\left(\frac{\Delta N_{Pm}}{N_{Pm}}\right)^2 + \left(\frac{\Delta N_{ref}}{N_{ref}}\right)^2 + \delta F^2} = A \cdot \sqrt{\left(\frac{0.8}{61.9}\right)^2 + \left(\frac{0.6}{3.5}\right)^2 + 0.03^2} = 0.4 \text{ Ci} \quad (\text{A7})$$

where  $\delta F = 3\%$  is the error in flux of the reference source given in its manufacturer certificate.

Finally, the activity of Pm-147 source BPm7-MU08-6 Rectangular on 05/06/08 is equal to  $2.6 \pm 0.4 \text{ Ci}$ .

## REFERENCES

<sup>1</sup> <http://www.nndc.bnl.gov/chart/chartNuc.jsp>

<sup>2</sup> <http://www.nndc.bnl.gov/nudat2/>

<sup>3</sup> G. F. Knoll, “Radiation Detection and Measurement,” 3<sup>th</sup> ed., John Wiley&Sons (2000).

<sup>4</sup> <http://physics.nist.gov/PhysRefData/XrayMassCoef/tab4.html>

<sup>5</sup> <http://physics.nist.gov/PhysRefData/XrayMassCoef/tab2.html>



## Appendix B

### MEASUREMENTS OF SPACE CHARGE DISTRIBUTION IN DIELECTRICS

#### B1. Description of the methods for the measurement of the space charge distribution in dielectric

To understand the different processes in dielectric under beta irradiation, and optimizing the dielectrics to accumulate, store, and transfer charge, while minimizing the risks from breakdown, it is important to know the charge distribution in the dielectric with time. In the last three decades, a significant effort has been made to understand the internal charge distributions in dielectrics. This has resulted in the development of a number of nondestructive methods which give detailed information about space charge distributions. Such methods can be divided into several groups.<sup>1, 2</sup>

- The thermal pulse method applies a thermal pulse to one surface of the dielectric by means of a light flash and measures the electrical response generated by the sample as a function of time while the thermal transient diffuses across the sample. The form of the time dependence of the electrical response carries the information about the charge or polarization distribution. Such distribution only can be obtained by a deconvolution process. The resolution of this method is around 2  $\mu\text{m}$  in a sample  $\sim 200 \mu\text{m}$  thick.

- The laser intensity modulation method (LIMM) utilizes sinusoidally-modulated surface heating of dielectric samples to produce spatially nonuniform temperature distributions through the material. In the LIMM technique, each surface of the sample is exposed to a laser beam which is intensity modulated in a sinusoidal fashion by an acousto-optic modulator or light chopper. The laser beam is absorbed by the front of the electrode of the sample. The sinusoidal modulation of the laser beam causes a sinusoidal fluctuation in temperature of the front electrode, resulting in propagation of temperature waves into the sample. The temperature waves are attenuated as they progress through the sample and they also are retarded in phase. The interaction of the fluctuating temperature and the spatially distributed polarization and space charge produces a sinusoidal pyroelectric current. This

current is a unique function of the modulation frequency and the polarization and charge distributions. Like the thermal pulse methods, a mathematical deconvolution technique is required to compute the polarization and space-charge distributions from the current-frequency data. The resolution of this method is around  $2\text{ }\mu\text{m}$  in a sample  $\sim 25\text{ }\mu\text{m}$  thick.

- In the laser induced pressure pulse method, one side of a sample containing space charges is irradiated with a short laser-light pulse and a pressure is generated by laser ablation. As the very narrow compressed region travels through the sample, a current is induced in the external circuit due to non uniform changes in dimension and permittivity reflecting the space charge distribution. When the thickness of the compressed region is small, the profile of the current response is directly proportional to the charge distribution, including the charges on the electrodes. The resolution of this method is around  $1\text{ }\mu\text{m}$  in a sample  $\sim 100\text{-}1000\text{ }\mu\text{m}$  thick.

- In the pressure wave propagation (PWP) method, a pressure wave is generated by absorbing a short laser light pulse in a metal target bonded to the dielectric plate under investigation. For a short duration pulse, the electrical response gives directly the spatial distributions of the electric field and charge density. A short duration (typically  $1\text{ ns}$ ) pressure wave can be generated by the impact of a  $35\text{ ps}$  Nd-YAG laser pulse on a  $500\text{ }\mu\text{m}$  thick aluminum target covering one of the electrodes. The resolution of this method is around  $10\text{ }\mu\text{m}$ , thickness of the sample  $\sim 5\text{-}200\text{ }\mu\text{m}$ .

- The acoustic probe method is based on the effect of generation of an electric signal by mechanical excitation of the charged specimen. The mechanically generated longitudinal wave forms a narrow, deformed, layer in the sample, which moves through the specimen. The electrical signal as a function of time is proportional to the charge density and field intensity of the deformed area. The resolution of this method is around  $200\text{ }\mu\text{m}$ , thickness of the sample  $\sim 2\text{-}6\text{ mm}$ .

- The principle of the pulsed electro-acoustic (PEA) methods is based on the Lorentz force law, where an externally applied pulse field induces a perturbing force density on the material in the presence of resident charges. The perturbation launches an acoustic wave which originates from the charged bulk. The acoustic signal then is detected by a piezoelectric transducer mounted on one of the electrodes. The space-charge profile

information contained in the exiting acoustic signal is extracted and calibrated through the use of a digital signal processing. It should be noted here that the acoustic wave is internally generated by the space charge in contrast to the pressure wave propagation methods where the pressure wave is generated externally. The resolution of this method is around 10  $\mu\text{m}$  for samples  $<10000 \mu\text{m}$ , but new PEA systems with resolution  $\sim 2 \mu\text{m}^3$  use deconvolution techniques to obtain the space charge profile.

PEA method is now widely accepted as one of the most simple and effective techniques for the measurement of the space charge distribution in solid dielectrics. The core of the PEA method is to position a charged sample between two electrodes, give an electric pulse to the sample, and measure the acoustic wave form caused by the charge distribution. The great advantage this method is that measurements of the space charge distribution can be carried out “in-situ”, during irradiation.

## B2. Principle of the pulsed electro acoustic method

The principle of PEA method is shown in Figure B1.<sup>4,5</sup> The principle is based on the Lorentz force law.<sup>3,6</sup> The following assumptions are made:

- The space charge accumulations, electric field distributions, and acoustic wave propagation are constant in the x-y plane, and vary only in the z dimension (see Figure B1). It is based on the condition that the wavelength of the acoustic wave is much smaller than the diameter of the detecting electrodes.
- The generated acoustic wave shape in each charge layer inside dielectric is the same as that of the applied pulsed electric field.
- Every frequency component of the acoustic wave propagates through the dielectric with the same velocity  $v_{sa}$  and without decrease in amplitude during the propagation. Thus attenuation and dispersion can be neglected.
- The linear superposition principle is applicable for interaction of the two or more acoustic waves.

The configuration of the PEA method is that a sheet sample with thickness  $d$ , with a space charge,  $\rho(z)$ , placed between two electrodes. An external electric field pulse,  $e_p(t)$ , of duration  $dT$  and amplitude  $V_p/d$  is applied. This electric pulse creates an electric force,  $df(z,t)$ , causing a charge,  $\rho(z)$ , to move. This movement launches an acoustic pressure wave,  $dp(z,t)$ , that propagates through the sample which is transformed into an electric signal,  $v_s(t)$ , by the piezoelectric transducer.

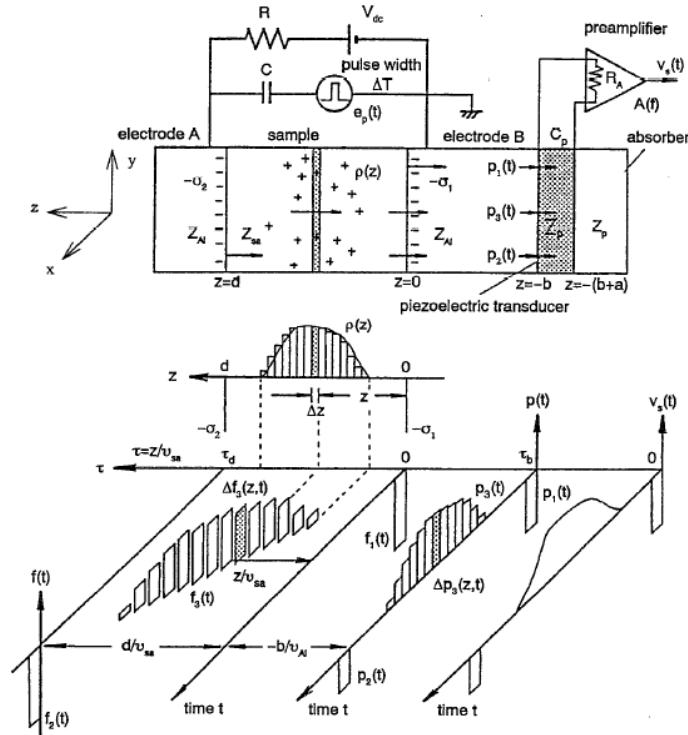


Figure B1. Schematic diagram of pulsed electro acoustic method<sup>5</sup>

An electric force  $df(z,t)$  acting on a charge layer  $\rho(z) \cdot \Delta z$  under electric field pulse can be written as

$$df(z,t) = \rho(z) \cdot dz \cdot e_p(t) \quad (B1)$$

An acoustic pressure wave arrive on the transducer with delay  $\tau_s$

$$\tau_s = \frac{b}{v_{al}} + \frac{z}{v_d}, \quad (B2)$$

where  $b$  is thickness of the electrode,  $v_{al}$  is the velocity of sound in aluminum,  $v_d$  is the velocity of sound in the sample.

The acoustic pressure wave on the transducer is

$$dp(z, t - \tau_s) = \rho(z) \cdot dz \cdot e_p(t - \tau_s) \quad (B3)$$

The total acoustic wave detected by transducer is

$$p(t) = \int_0^z \rho(z) \cdot e_p(t - \tau_s) \cdot dz = \int_0^z \rho(z) \cdot e_p\left(t - \frac{b}{v_{al}} - \frac{z}{v_d}\right) \cdot dz \quad (B4)$$

In this Equation,  $b/v_{al}$  is constant,  $\tau = z/v_d$  depends on the position of the charge layer, so Equation (B4) can be expressed as

$$p(t) = v_d \cdot \int_0^t r(\tau) \cdot e_p\left(t - \frac{b}{v_{al}} - \tau\right) \cdot d\tau, \quad (B5)$$

where  $r(\tau)$  is transformed from  $\rho(z)$  as function of position  $z$ .

So  $p(t)$  in Equation (A5) is convolution of functions  $r(\tau)$  and  $e_p(t)$ . The Fourier transform of  $p(t)$  can be taken:

$$P(f) = v_d \cdot R(f) \cdot E(f) \cdot \exp(-j \cdot 2\pi \cdot f \cdot \frac{b}{v_{al}}) \quad (B6)$$

where  $R(f)$  and  $E(f)$  are the Fourier transform of  $r(t)$  and  $e(t)$ , respectively.

The relationship between the output electric signal  $v_s(t)$  and transmitted acoustic wave  $p(t)$  are related in convolution form by

$$V_s(f) = H(f) \cdot P(f), \quad (B7)$$

where  $V_s(f)$  and  $P(f)$  are the Fourier transforms of  $v_s(t)$  and  $p(t)$ , respectively, and  $H(f)$  is the transfer characteristics of the transducer.

To obtain  $H(f)$  the sheet charge can be induced on the electrode surface, and pulse electric field is applied. Because the thickness of the induced charge is negligible, Equation (B6) became:

$$P_1(f) = A \cdot E(f) \cdot \exp(-j \cdot 2\pi \cdot f \cdot \frac{b}{v_{al}}), \quad \text{and} \quad (\text{B8})$$

$$V_{s1}(f) = H(f) \cdot P_1(f) \quad (\text{B9})$$

where  $A$  is constant,  $V_{s1}(f)$  and  $P_1(f)$  are the Fourier transforms of  $v_{s1}(t)$  and  $p_1(t)$ , respectively.

From Equations (B5), (B6), (B8) and (B9) follow

$$R(f) = A \cdot \frac{V_s(f)}{v_d \cdot V_{s1}(f)} \quad (\text{B10})$$

The inverse Fourier transform of  $R(f)$  gives the function  $r(t)$ , and using  $z = v_d \cdot (t - b/v_{al})$  the function  $\rho(z)$  can be obtained. The value  $A$  can be determined according the condition that integration of  $\rho(z)$  over the volume of the sample equal the total charge.<sup>7</sup>

### B3. Experimental setup

Defining the space charge distribution in dielectric samples under the tritium beta particles irradiation was carried using the Mini-PEA System (FiveLab (Japan)) with resolution  $<10 \mu\text{m}$ . The PEA-system was mounted on a special holder and connected to electronics in situ (see Figure B2). Checking the workability of the Mini-PEA system was done using PVC and PMMA reference samples and comparing the results with given in reference documents (see Figure B3). The view of the output signal from PVC reference sample is shown in Figure B3. The shape and value of the signal from PVC and PMMA reference samples correspond the given from FiveLab.

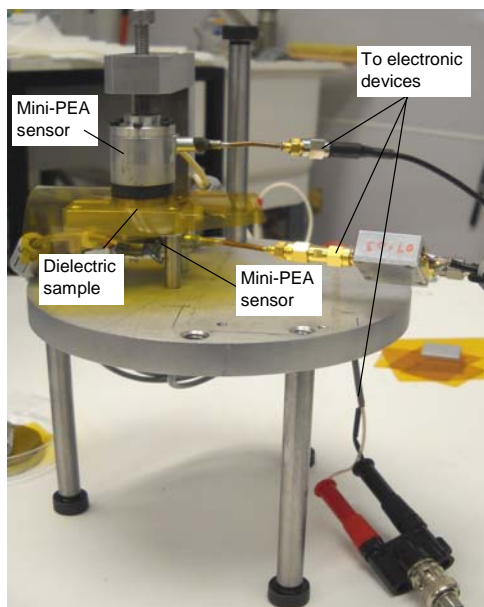


Figure B2. Overview of the Mini-PEA system

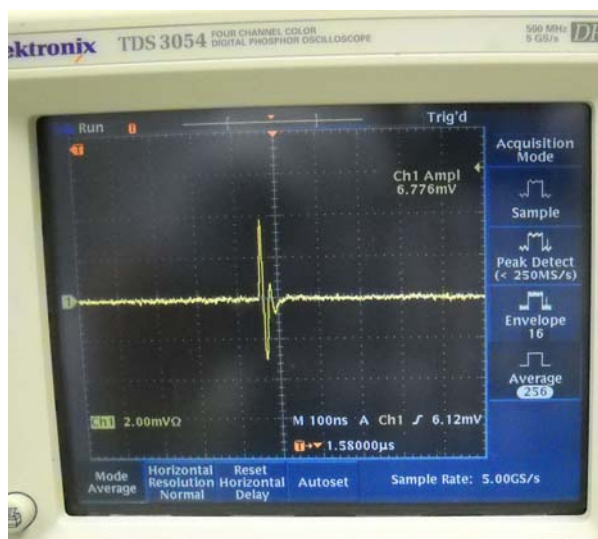


Figure B3. Output signal of the PVC reference sample

The Mini-PEA system was mounted in the vacuum chamber for experiments (see Figure B4). All charge accumulation were made under vacuum condition  $<10^{-3}$  Torr to prevent leakage through the surrounding air.



Figure B4. The Mini-PEA system in the vacuum chamber

Measure of the output signal from the bias voltage was made for comparison to the sheet charge on the sample (bias voltage) and distribution due to irradiation by tritium beta particles. One of the comparisons of the output signal from a reference sample with applied bias voltage (sheet charge) and tritium irradiated sample (volume charge) are shown in Figure B5.

The calculation of the space charge distribution was made using MatLab code following the procedure described earlier. The result of calculation is shown in Figure B6. Because of the low resolution of the mini-PEA system ( $\sim 10 \mu\text{m}$ ) we can only say that penetration depth for tritium beta particles is not more than  $\sim 7 \mu\text{m}$ . This value is a bit higher than calculated (see Figure 6.10), perhaps due to charge transfer during irradiation or measurement error because of poor resolution and software.

PEA resolution  $\sim 1 \mu\text{m}$  can be achieved with FiveLab software.

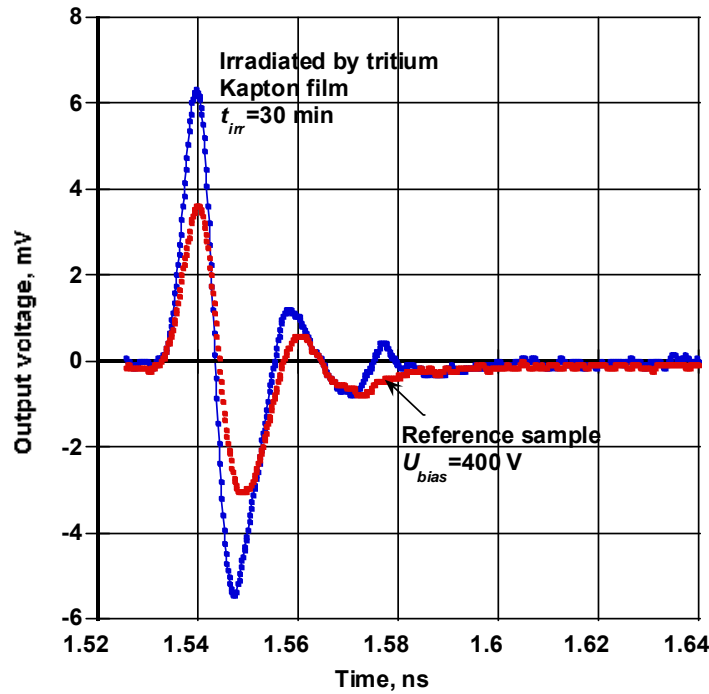


Figure B5. Output signal from irradiated by tritium beta particles during 30 min. Polyimide (Kapton) thickness is  $30 \mu\text{m}$  and the reference sample was biased with 400 V.



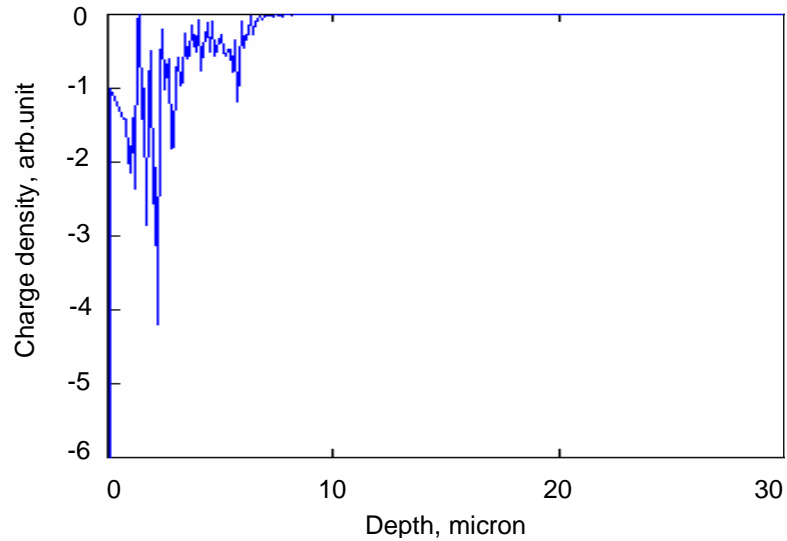


Figure B6. Space charge distribution in polyimide irradiated by tritium beta particles during 30 minutes, arb. units, measured by the pulsed electro acoustic method

## REFERENCES

- <sup>1</sup> N. H.Ahmed, and N. N.Srinivas, "Review of Space Charge Measurements in Dielectric," *IEEE Transactions on Dielectric and Electrical Insulation* **4** (5), 644 (1997).
- <sup>2</sup> M. A. Noras, "Charge Detection Methods for Dielectrics – Overview," *Trek Application Note* **1** (Nov 2005).
- <sup>3</sup> K. Fukunaga, "Progress and Prospects in PEA Space Charge Measurement Techniques," *IEEE Electrical Insulation Magazine* **26** (2008).
- <sup>4</sup> Y.Li, M.Aihara, et al., "Space charge measurement in thick dielectric materials by pulsed electroacoustic method," *Review Scientific Instruments* **66**, 3909 (1995).
- <sup>5</sup> Li Y., Yasuda M., and Takada T., "Pulsed Electroacoustic Method Measurement of Charge for Accumulation in Solid Dielectrics," *IEEE Transactions on Dielectric and Electrical Insulation* **1**, 2, 188 (1994).
- <sup>6</sup> Maeno T., Futami T., Kushibe H., Takada T. , et al., "Measurement of Spatial Charge Distribution in Thick Dielectrics Using the Pulsed Electroacoustic Method," *IEEE transactions on Electrical Insulation* **23**, 443 (1988).
- <sup>7</sup> Kushibe H., Maeno T., and Takada T., "Measurement of Accumulated Charge Inside Dielectric by Pulsed Electric Forced Techniques," *Trans. IEE Japan*, **A-106**, 118 (1986).

## LIST OF PUBLICATIONS

### Publications:

- Kavetsky A., **Yakubova G.**, Yousaf S.M., Bower K., *Tritium battery with solid dielectric*, Nuclear Science and Engineering (submitted, 2010).
- *Promethium-147 Capacitor*, Applied radiation and isotopes, **67**, 1057, 2009.
- Kavetsky A., **Yakubova G.**, Sychov M., et al. *Tritium-charged capacitor*, Nuclear Science and Engineering, **158**, 321, 2008.
- Sychov M., Kavetsky A., **Yakubova G.**, et al. *Alpha indirect conversion radioisotope power source*. Applied radiation and isotopes, **66**, 173, 2008.
- Kavetsky A., **Yakubova G.**, Sychov M., et al. *Tritium “atomic battery”*. Investigation by chemistry, technology and application of radioactivity. Proceedings of Technological institute, Sankt-Petersburg, 2008, 46 (in Russian).

### Representative Presentations:

- Sychov M., Kavetsky A., **Yakubova G.**, et al. *Alpha indirect conversion radioisotope power source*, The 232<sup>nd</sup> Meeting of the American Chemical Society, San Francisco, 10-14 Sept., 2006.
- Kavetsky A., **Yakubova G.**, Sychov M., et al. *Autonomous direct charge alpha cell using tritium-charged capacitor to bias the secondary electron mesh*. The 232<sup>nd</sup> Meeting of the American Chemical Society, San Francisco, 10-14 Sept., 2006.

## CURRICULUM VITAE

**Galina N. Yakubova**

**TRACE Photonics, Inc.,  
Charleston, Illinois, 61920  
USA**

**Phone: (217) 348-6703 (office)  
(217) 549-4075 (cell)  
E-mail: [gyakubo2@illinois.edu](mailto:gyakubo2@illinois.edu)**

---

### **Career Summary**

Design of the nuclear batteries with vacuum and solid dielectric and study its electrical characteristics. Investigation of the space-charge behavior in beta irradiated dielectrics.

Research in the field of development of the radiation instrumentation.

Research in the field of metrology of ionizing radiation.

Research in the field of radiological environmental monitoring, health physics.

### **Professional Experience:**

***TRACE Photonics, Inc., Charleston, Illinois, 61920***

**Research Scientist**

**2006 to present**

- Basic research in the field of direct charge nuclear batteries. Development of alpha and beta direct charge nuclear batteries with vacuum and solid dielectric. Investigation of the internal space charge distribution in the dielectric under beta irradiation.
- Data analysis of the charging process in nuclear batteries, and electrical characteristics of the devices.

***Khlopin Radium Institute, St. Petersburg, Russia (05/92-05/06)***

**Chief of Metrology Service Bureau**

**1992-2006**

- Managing the team of fifteen staff members in all aspects of metrological documentation: R&D reports, technical reports, specifications; device certification programs and techniques, with emphasis on the measurement of radiation-physical parameters of ionizing radiation sources;
- Development of the radiation instrumentation for the detection and characterization of radioactive sources, environmental samples, and nuclear materials;
- Responsibility for dosimetric, radiometric and spectrometric measurements of the radioactive isotopes in the environmental samples; mathematical modeling and mapping of the environmental monitoring results.

**Senior Engineer**

**1985-1992**

- Development of the metrological certifications for ionizing radiation instruments;

- Development of the measuring technique for determination of the radioactive isotope activity in the ionizing radiations sources, tritium in air, and other environmental samples;
- Development of the technique in the field of health physics.

## **Engineer**

**1979-1985**

- Certification and calibration of ionizing radiation instruments.

## **Teaching Experience:**

### ***High school #9, St. Petersburg, Russia***

**1995-2005**

- Teacher of mathematics, physics, and basics of computer programming.

## **Computer skills:**

- Working knowledge of software: MatLab, MathCad, KaleidaGraph, Origin, Excel, Geant4.

## **Education:**

*University of Illinois at Urbana-Champaign (2010)*

**PhD.** Major: Nuclear Engineering.

Dissertation: Nuclear batteries with tritium and promethium-147 radioactive sources

*The Polytechnic Institute, St. Petersburg, Russia (1988)*

**MS.** Major: Automation of experimental researches.

Thesis: Mathematical modeling and mapping of large area gamma emissions.

*The Institute of aviation appliance-construction, St. Petersburg, Russia (1977)*

**MS.** Major: Electronic Computing Machine.

Thesis: Electronic circuit design and fabrication for logic operations.

*The St. Petersburg Pedagogical Mastery University, St. Petersburg, Russia (2001)*

**MS.** Major: Pedagogue-psychologist. Practical psychology.

## **License/Certification**

*ORTEC, USA (2006)*

The Fundamentals of Gamma Spectrometry, Course #2005-00-043.

*ORTEC, USA (2006)*

The Fundamentals of Alpha Spectrometry, Course #2005-00-044.

*The Academy of Standardization, Metrology and Certification, St. Petersburg, Russia (2004)*

Verification and Calibration of measurement instrumentation for ionizing radiation; state verification officer.

*The Polytechnic Institute, St. Petersburg, Russia (1984)*

Metrological providing of research & development issues; expert-metrologist.

#### **Publications:**

- Kavetsky A., **Yakubova G.**, Yousaf S.M., Bower K. *Tritium battery with solid dielectric*, *Nuclear Science and Engineering* (submitted, 2010)
- Kavetsky A., **Yakubova G.**, Lin Q., et al. *Prometium-147 Capacitor*, *Applied radiation and isotopes*, **67**, 1057, 2009.
- Kavetsky A., **Yakubova G.**, Sychov M., et al. *Tritium-charged capacitor*, *Nuclear Science and Engineering*, **158**, 321, 2008.
- Sychov M., Kavetsky A., **Yakubova G.**, et al. *Alpha indirect conversion radioisotope power source*. *Applied radiation and isotopes*, **66**, 173, 2008.
- Kavetsky A., **Yakubova G.**, Sychov M., et al. *Tritium “atomic battery”*. Investigation by chemistry, technology and application of radioactivity. Proceedings of Technological institute, Sankt-Petersburg, 2008, 46 (in Russian).

#### **Representative Presentations:**

- Sychov M., Kavetsky A., **Yakubova G.**, et al. *Alpha indirect conversion radioisotope power source*, The 232<sup>nd</sup> Meeting of the American Chemical Society, San Francisco, 10-14 Sept., 2006.
- Kavetsky A., **Yakubova G.**, Sychov M., et al. *Autonomous direct charge alpha cell using tritium-charged capacitor to bias the secondary electron mesh*. The 232<sup>nd</sup> Meeting of the American Chemical Society, San Francisco, 10-14 Sept., 2006.

#### **Professional Activities:**

- Member, The American Nuclear Society.
- Member, The American Chemical Society.